Forschungszentrum Jülich

IBG-2: Institute for Bio- and Geosciences — Plant Sciences

Understanding Stress-induced Dynamics of Solar-induced Chlorophyll Fluorescence with Leaf-level Hyperspectral Imaging

Dissertation

zur Erlangung des Grades

Doktorin der Agrarwissenschaften (Dr. agr.)

der Agrar-, Ernährungs- und Ingenieurwissenschaftlichen Fakultät

der Rheinischen Friedrich-Wilhelms-Universität Bonn

von

Huaiyue Peng

aus

Henan, China

Bonn 2026

Referent: Prof. Dr. Uwe Rascher

Koreferentin: Prof. Dr. Ribana Roscher

Tag der mündlichen Prüfung: 21.04.2026

Angefertigt mit Genehmigung der Agrar-, Ernährungs- und Ingenieurwissenschaftlichen Fakultät der Universität Bonn

Abstract

Proximal sensing of solar-induced chlorophyll fluorescence (SIF) is widely used as a non-invasive indicator of photosynthetic activity. Together with photochemical quenching (PQ) and non-photochemical quenching (NPQ), SIF represents a third pathway of energy dissipation in excited chlorophyll molecules and provides direct insight into the redox state of the photosystem, particularly under stress conditions, often with shorter response times than vegetation indices (VIs). Because SIF does not require artificial illumination, it can be applied across spatial scales from leaf to global satellite observations. However, two major challenges limit the direct interpretation of SIF in terms of photosynthetic efficiency: (1) accurate estimation of SIF yield due to confounding effects of absorbed PAR (APAR) and fluorescence escape probability, both influenced by illumination geometry, plant structural, and physiological properties; and (2) incomplete understanding of the relationships among SIF yield, NPQ, and PQ under stress. To address part of these challenges, this thesis first introduced a ground-based hyperspectral imaging system (HyScreen) for high-resolution retrieval of red and far-red SIF. The proposed measurement protocol and processing chain achieved high accuracy, with relative errors of 0.4–1.0% for red SIF and 0.2–0.5% for far-red SIF due to noise. Second, a controlled cold-stress experiment was conducted to evaluate the combined use of SIF and VIs as indicators of cold stress tolerance in *Arabidopsis thaliana*. Specifically, the study examined whether SIF and VIs can (1) detect cold stress duration, (2) distinguish genotypes with contrasting NPQ capacity, and (3) resolve differences in photoinhibition between young and mature leaves. The results show that (1) acute cold stress initially induced high SIF yield with high near-infrared (NIR) reflectance, followed by decreasing SIF, reduced NIR reflectance, and reduced red-edge normalized difference vegetation index (NDVIre) under photoinhibition. Low values of the effective quantum yield of PSII together with high NPQ indicated that NPQ dominated SIF quenching during cold stress, while changes in NIR reflectance and NDVIre indicated cold-induced alterations in leaf structure and reduced chlorophyll content, respectively. (2) Four genotypes differing in NPQ capacity were distinguishable by combining SIF yield, photochemical reflectance index (PRI), and NDVIre. Early SIF responses reflected the fast NPQ component qE, whereas the change and temporal profile of PRI captured both qZ and overall NPQ during prolonged stress. Importantly, higher qE or qZ capacity did not necessarily correspond to reduced photodamage, as chlorophyll degradation (indicated by reduced NDVIre) contributed strongly to photoinhibition. (3) Young leaves exhibited greater cold tolerance than mature leaves, as evidenced by higher Fv/Fm after cold exposure, characterized by higher qE capacity, retention of qZ activity, and better chlorophyll maintenance, as indicated by lower initial SIF yield, higher PRI, and higher NDVIre. In summary, HyScreen enables leaf-level SIF imaging while minimizing background effects and provides new opportunities to investigate spatial heterogeneity in photoprotective responses from leaf to plant scales. This study suggests that the combined use of SIF and VIs can capture NPQ dynamics, chlorophyll degradation, and leaf structural responses linked to cold stress tolerance across genotypes and leaf ages. This work also provides insights relevant to future validation activities for the ESA FLEX mission and to high-throughput screening of stress-tolerant plants in breeding programs.

Zusammenfassung

Die bodennahe Fernerkundung der sonneninduzierten Chlorophyllfluoreszenz (SIF) wird in der Forschung häufig als nicht-invasiver Indikator für photosynthetische Aktivität eingesetzt. Zusammen mit dem photochemischen Quenching (PQ) und dem nicht-photochemischen Quenching (NPQ) stellt SIF einen dritten Weg der Energiedissipation angeregter Chlorophyllmoleküle dar und ermöglicht direkte Einblicke in die Physiologie der Photosysteme, insbesondere unter Stressbedingungen. Im Vergleich zu Vegetationsindizes (VIs) zeigt sich, dass SIF häufig eine schnellere Reaktion auf physiologische Veränderungen aufweist. Für SIF-Messungen ist keine künstliche Beleuchtung erforderlich, sodass sie über verschiedene Skalen hinweg angewendet werden können – vom Blatt bis zur globalen Satellitenbeobachtung. Die unmittelbare Interpretation der SIF in Bezug auf die photosynthetische Effizienz wird jedoch durch zwei zentrale Herausforderungen limitiert: Einerseits erschwert der Einfluss der absorbierten photosynthetisch aktiven Strahlung (APAR) sowie der Fluoreszenz-Austrittswahrscheinlichkeit die exakte Bestimmung der SIF-Ausbeute. Dabei sind die Beleuchtungsgeometrie sowie die strukturellen und physiologischen Eigenschaften der Pflanze zu berücksichtigen. Zweitens sind die Zusammenhänge zwischen SIF-Ausbeute, NPQ und PQ unter abiotischem Stress bislang unzureichend verstanden. Zur Bearbeitung dieser Fragestellungen wurde in dieser Arbeit zunächst ein bodengestütztes hyperspektrales Bildgebungssystem (HyScreen) zur hochauflösenden Erfassung von roter und fernroter SIF eingeführt. Das Messprotokoll und die Datenverarbeitung wiesen eine hohe Genauigkeit mit relativen Fehlern von 0,4–1,0 % für rote SIF und 0,2–0,5 % für fernrote SIF aufgrund von Rauschen auf. Im Anschluss wurde ein kontrolliertes Kältestressexperiment durchgeführt, um die kombinierte Verwendung von SIF und Vegetationsindizes als Indikatoren für die Kältestresstoleranz bei *Arabidopsis thaliana* zu bewerten. Im Rahmen der Untersuchung wurde analysiert, ob diese Parameter (1) die Dauer von Kältestress erfassen, (2) Genotypen mit divergierender NPQ-Kapazität differenzieren und (3) Diskrepanzen in der Photoinhibition zwischen jungen und alten Blättern auflösen können. Die Ergebnisse zeigen, dass (1) akuter Kältestress zunächst zu erhöhter SIF-Ausbeute und hoher Nahinfrarot-Reflexion (NIR) führte, gefolgt von abnehmender SIF, reduzierter NIR-Reflexion und vermindertem Red-Edge Normalized Difference Vegetation Index (NDVIre) unter Photoinhibition. Niedrige Werte der effektiven Quantenausbeute von PSII in Kombination mit hoher NPQ deuten darauf hin, dass NPQ die Abschwächung der SIF während des Kältestresses dominierte, während Änderungen der NIR-Reflexion und des NDVIre auf kälteinduzierte Veränderungen der Blattstruktur bzw. eine Abnahme des Chlorophyllgehalts hinwiesen. (2) Vier Genotypen mit unterschiedlicher NPQ-Kapazität konnten durch die kombinierte Analyse von SIF-Ausbeute, Photochemical Reflectance Index (PRI) und NDVIre unterschieden werden. Frühe SIF-Reaktionen spiegelten die schnelle NPQ-Komponente qE wider, während zeitliche Änderungen des PRI sowohl qZ als auch die gesamte NPQ-Dynamik während längerem Stress erfassten. Eine höhere qE- oder qZ-Kapazität ging dabei nicht zwingend mit geringerer Photodamage einher, da Chlorophyllabbau – angezeigt durch reduziertes NDVIre – wesentlich zur Photoinhibition beitrug. (3) Junge Blätter zeigten eine höhere Kältetoleranz als ältere Blätter, belegt durch höhere Fv/Fm-Werte nach Kälteeinwirkung und charakterisiert durch höhere qE-Kapazität, anhaltende qZ-Aktivität und bessere Erhaltung des Chlorophyllgehalts, angezeigt durch geringere anfängliche SIF-Ausbeute, höheren PRI und höheres NDVIre. Zusammenfassend ermöglicht HyScreen eine blattweise SIF-Bildgebung mit reduzierten Hintergrundeinflüssen und eröffnet neue Möglichkeiten zur Analyse räumlicher Heterogenität photoprotektiver Reaktionen vom Blatt- bis zum Pflanzenmaßstab. Die Ergebnisse legen nahe, dass die kombinierte Nutzung von SIF und Vegetationsindizes NPQ-Dynamiken, Chlorophyllabbau und strukturelle Blattveränderungen im Zusammenhang mit Kältetoleranz über verschiedene Genotypen und Blattalter hinweg erfassen kann und liefern zugleich wichtige Beiträge für zukünftige Validierungsaktivitäten der ESA-Mission FLEX sowie für die hochdurchsatzbasierte Selektion stresstoleranter Pflanzen in der Züchtung.

Contents

List of Abbreviations

3FLD	three-band Fraunhofer line depth method
APAR	absorbed photosynthetically active radiation
ATP	adenosine triphosphate
CCI	chlorophyll/carotenoid index
Chl a	chlorophyll a
Chl b	chlorophyll b
ChlaF	chlorophyll fluorescence
CIre	chlorophyll index red-edge
CMOS	complementary metal-oxide semiconductor
Col	*Arabidopsis thaliana* Columbia
DAC	data acquisition computer
DC	dark current
DCMU	(3,4-dichlorophenyl)-1,1-dimethylurea (herbicide)
DN	dark current
DPPN	German Plant Phenotyping Network
ELM	empirical line method
FCVI	fluorescence correction vegetation index
FLD	Fraunhofer line depth method
FLUO	fluorescence sensor module
FOV	field of view
fps	frames per second
FRET	Förster resonance energy transfer
FRRF	fast repetition rate fluorescence
FWHM	full width at half maximum
iFLD	improved Fraunhofer line depth method
ISSF	spectral instrument spectral spread function
IT	integration time

LCNP	plastid lipocalin
LHC	light-harvesting complexes
LHCI	light-harvesting complexes associated primarily with PSI
LHCII	light-harvesting complexes associated primarily with PSII
LIFT	light-induced fluorescence transient
mARI	modified anthocyanin reflectance index
mCRIgreen	modified carotenoid reflectance index
NADPH	nicotinamide adenine dinucleotide phosphate (reduced form)
NDVI	normalized difference vegetation index
NDVIre	red-edge normalized difference vegetation index
NER	noise equivalent radiance
NIR	near-infrared
NIRv	near-infrared radiance of vegetation
NIRvR	near-infrared radiance of vegetation
NPQ	non-photochemical quenching energy dissipation
NPQ	parameter of non-photochemical quenching energy dissipation
O_2A	Earth's atmosphere telluric oxygen absorption A bands (759–770 nm)
O_2B	Earth's atmosphere telluric oxygen absorption B bands (687–692 nm)
PAM	pulse-amplitude modulated fluorometry
PAR	photosynthetically active radiation
PCU	power and control unit
ROI	regions of interest
ROS	reactive oxygen species
PQ	photochemical quenching
PRI	photochemical reflectance index
PsbS	a photoprotective protein in LHCII
PSF	point spread function
PS I	Photosystem I
PS II	photosystem II
qE	energy-dependent quenching

qI	photoinhibitory quenching
qT	state transition
qZ	zeaxanthin-dependent quenching
S0	ground singlet state
S1	first excited singlet state
Sn	higher excited singlet state
sFLD	simple Fraunhofer line depth method
SFM	spectral fitting method
SIF	solar-induced chlorophyll fluorescence
SNR	signal-to-noise ratio
SR	simple ratio
TOC	top-of-canopy
UAVs	unmanned aerial vehicles
VDE	violaxanthin de-epoxidase
VIs	vegetation indices
VIS	visible
VNIR	visible and near-infrared sensor module
Vx	violaxanthin
WBI	water band index
WI	wavelength intervals
ZEP	zeaxanthin epoxidas
Zx	zeaxanthin
$Coeff_{rad}$	radiometric calibration coefficients
$E^{\downarrow}$	irradiance
F_0	minimum fluorescence flux emitted under the measuring light in the dark-adapted state
F_0'	minimum fluorescence flux emitted under the measuring light in the light-adapted state
F_m	maximal fluorescence when a saturation pulse is applied in the dark-adapted state

F_m'	maximal fluorescence in the light-adapted state
F_{red}	red chlorophyll fluorescence
F_{farred}	far-red chlorophyll fluorescence
F_s	steady-state fluorescence flux
F_v	variable fluorescence flux
F_q'	variable fluorescence flux in the light-adapted state
F_v/F_m	maximum quantum yield of photochemistry from PSII
$F687$	solar-induced chlorophyll fluorescence at 687 nm
$F687y$	solar-induced chlorophyll fluorescence yield at 687 nm
$F760$	solar-induced chlorophyll fluorescence at 760 nm
$F760y$	solar-induced chlorophyll fluorescence yield at 760 nm
k_D	rate constant of basal thermal dissipation
k_{IC}	rate constant of internal conversion
k_{ISC}	rate constant intersystem crossing
k_f	rate constant of chlorophyll fluorescence
k_{NPQ}	rate constant of non-photochemical quenching
k_P	rate constant of effective photochemistry, $k_P = qk_{PSII}$
k_{PSII}	rate constant of photochemical quenching
ΦF_{II}	quantum yield of fluorescence emission from PSII
ΦF_{IImax}	maximum quantum yield of fluorescence emission from PSII
ΦP_{II}	effective quantum yield of photochemistry in PSII
ΦP_{max}	maximum quantum yield of photochemistry from PSII

$L^{\uparrow}_{at-sensor}$	at-sensor upwelling radiance
$L^{\uparrow}_{TOC}$	top-of-canopy upwelling radiance
$L^{\uparrow}_{offset}$	offset in at-sensor upwelling radiance
$L^{\downarrow}_{TOC}$	top-of-canopy downwelling radiance
$L^{\downarrow}$	downwelling radiance
L_R	reflected radiance
Q_A	plastoquinone A
q	fraction of the open and functional reaction centres of PS II
qk_{PSII}	rate constant of effective photochemistry
qL	fraction of the open and functional reaction centres of PS II, lake model
qP	fraction of the open and functional reaction centres of PS II, puddle model
R	reflectance
R_{app}	apparent reflectance
Raw_{DC}	dark current of the raw data cube
Raw_{DN}	digital numbers of the raw data cube

1. Introduction*

Parts of this chapter have been published in peer-reviewed journals:

Huaiyue Peng, Maria Pilar Cendrero-Mateo, Juliane Bendig, Bastian Siegmann, Kelvin Acebron, Caspar Kneer, Kari Kataja, Onno Muller, and Uwe Rascher. 2022. "HyScreen: A Ground-Based Imaging System for High-Resolution Red and Far-Red Solar-Induced Chlorophyll Fluorescence" Sensors 22, no. 23: 9443. https://doi.org/10.3390/s22239443

The table below indicates the origin of different sections within this chapter:

Newly added	Adapted *	Original
Figure 1.1 Figure 1.2 Figure 1.9	Section 1 Section 1.3 Section 1.3.1	Everything else

In times of global climate change, efficiently and non-invasively quantifying photosynthetic traits is essential for better understanding the spatiotemporal adaptation of plants' primary metabolism and improving the early detection of stress, thereby enabling plant production management sustainably (Murchie et al., 2018; Schurr et al., 2006). To estimate photosynthesis in plants, chlorophyll a (Chl a) fluorescence (ChlaF) has been widely used due to its direct connection to the dynamic regulation of photosynthesis at the photosystem level. When chlorophyll molecules are excited by absorbed radiant fluxes, re-emitted fluorescence photons, namely ChlaF, compete with photochemical quenching (PQ) and non-photochemical quenching (NPQ) energy dissipation by heat (Figure 1.1). These three de-excitation processes are tightly interrelated and are also constantly adjusted in response to changing environmental conditions and stress levels (Maxwell and Johnson, 2000).

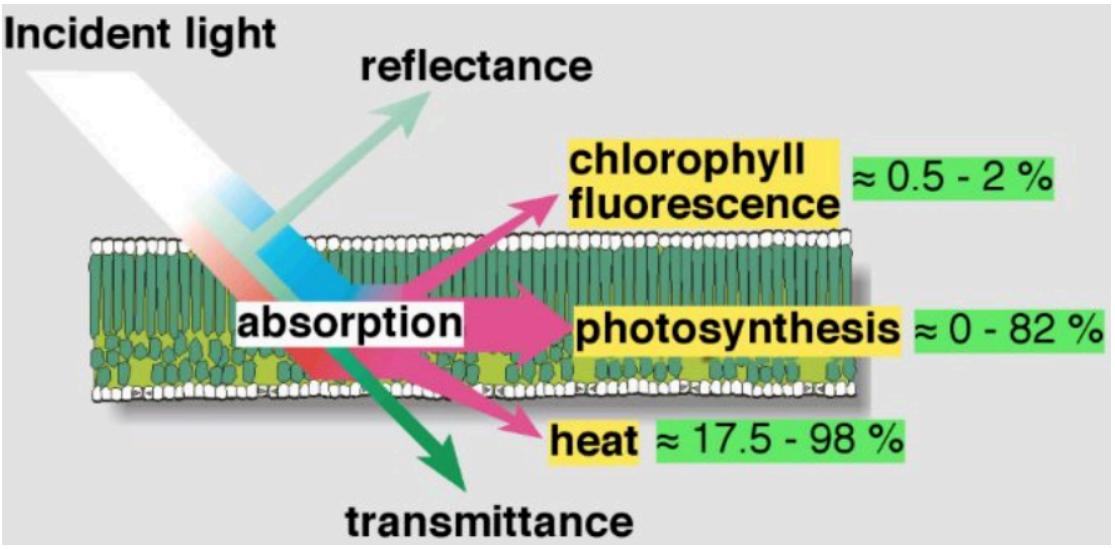

Figure 1.1 Three pathways of energy dissipation of absorbed energy in chlorophyll a molecules (Taccola et al., 2017).

The ChlaF emission of plants spans the spectral range of 650-800 nm, characterized by two peaks: one in the red region (around 685 nm) and the other in the far-red spectral region (around 740 nm) (Figure 1.2). Photosystem I (PS I) mainly emits ChlaF in the far-red range, and photosystem II (PS II) emits ChlaF both in the red and far-red ranges (Porcar-Castell et al., 2021). Depending on the excitation light source, ChlaF can be categorized as either active/artificial light induced ChlaF or solar-induced ChlaF (SIF). In contrast to active ChlaF measured under artificial activation light, SIF is considered passive ChlaF. It can serve as a real-time proxy for photosynthesis under natural illumination and can be measured on a larger scale in contrast to active ChlaF (Kolber et al., 2005; Maxwell and Johnson, 2000).

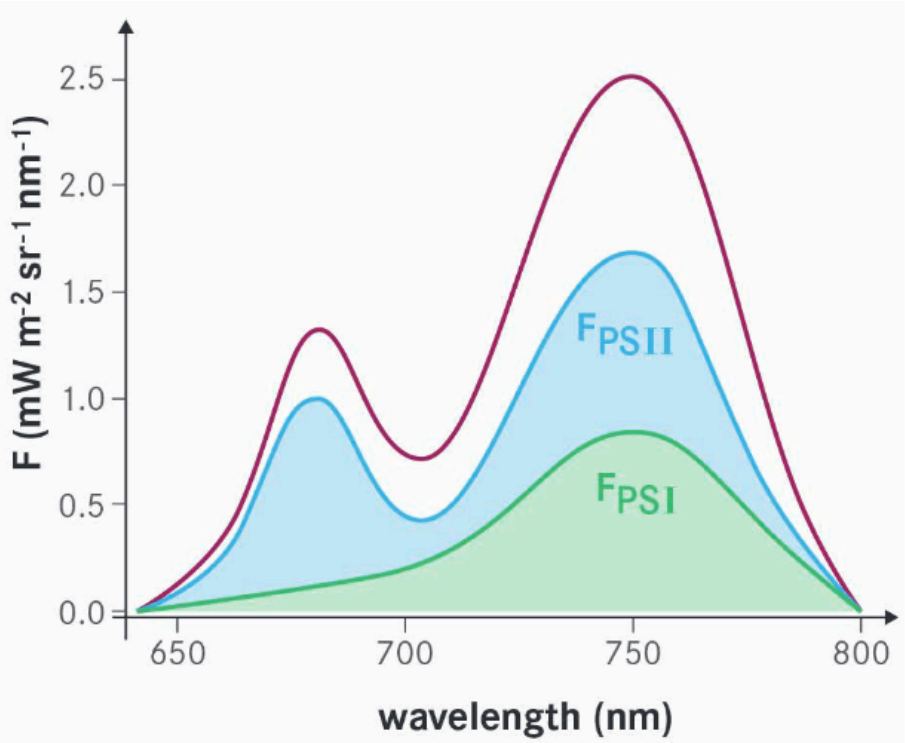

Figure 1.2 Emission spectrum of chlorophyll a fluorescence from both PSI and PSII photosystems. The two peaks occur at 685 nm and 740 nm (Fletcher, 2015).

1.1. Photosynthetic energy partitioning

Considering the propagation of light transfer from canopy to photosystem level and the reverse emission path of ChlaF, several factors play a crucial role in quantifying ChlaF and photosynthesis dynamics. These include the absorption of photosynthetically active radiation (PAR), energy distribution within PSI and PSII, the openness and connectivity of reaction centers, energy partitioning among ChlaF, NPQ, photochemistry, and energy decay, reabsorption, and the escape factor of ChlaF (Porcar-Castell et al., 2014). Given this complexity, it is worth introducing the structure of the photosystem and the energy distribution from the molecular level to photosystem level.

1.1.1. The structure of the photosynthetic apparatus

The light-dependent reactions of photosynthesis in higher plants occur on thylakoids, which are internal membranes within chloroplast. Photosystem I PSI and PSII are pigment-protein supercomplexes embedded in the thylakoid membranes, functioning as units for light harvesting and photochemistry (Figure 1.3). The antenna complexes and antenna proteins in PSII reaction center harvest light and deliver the captured energy to the associated core reaction center chlorophylls efficiently, facilitating electron transport to produce NADPH for dark reaction. However, PSII and PSI are spatially separated, and the distribution of

supercomplexes is uneven, indicating that a one-to-one stoichiometry between PSII and PSI is not required. The ratio of PSII to PSI in quantity is about 1.5:1, but this ratio increases when plants grow in shaded conditions (Taiz et al., 2015, p. 181).

The antenna system in higher plants typically comprises 200 to 300 chlorophyll molecules per reaction center. Light-harvesting complexes (LHCs) are the most abundant antenna proteins. Those associated primarily with PSII are called LHCII, while those associated with PSI are called LHCI. However, LHCII can also associate with PSI to modulate the distribution of excitation energy between PSII and PSI, a process known as state transition (Puggioni, 2020). LHCs contain Chls a, chlorophylls b (Chl b), and carotenoids including various carotenes such as β -carotene and xanthophylls (oxygenated carotenoids) such as lutein, neoxanthin, and violaxanthin. PSII and PSI core reaction centers are named P680 and P700, respectively, based on their maximum absorption wavelengths.

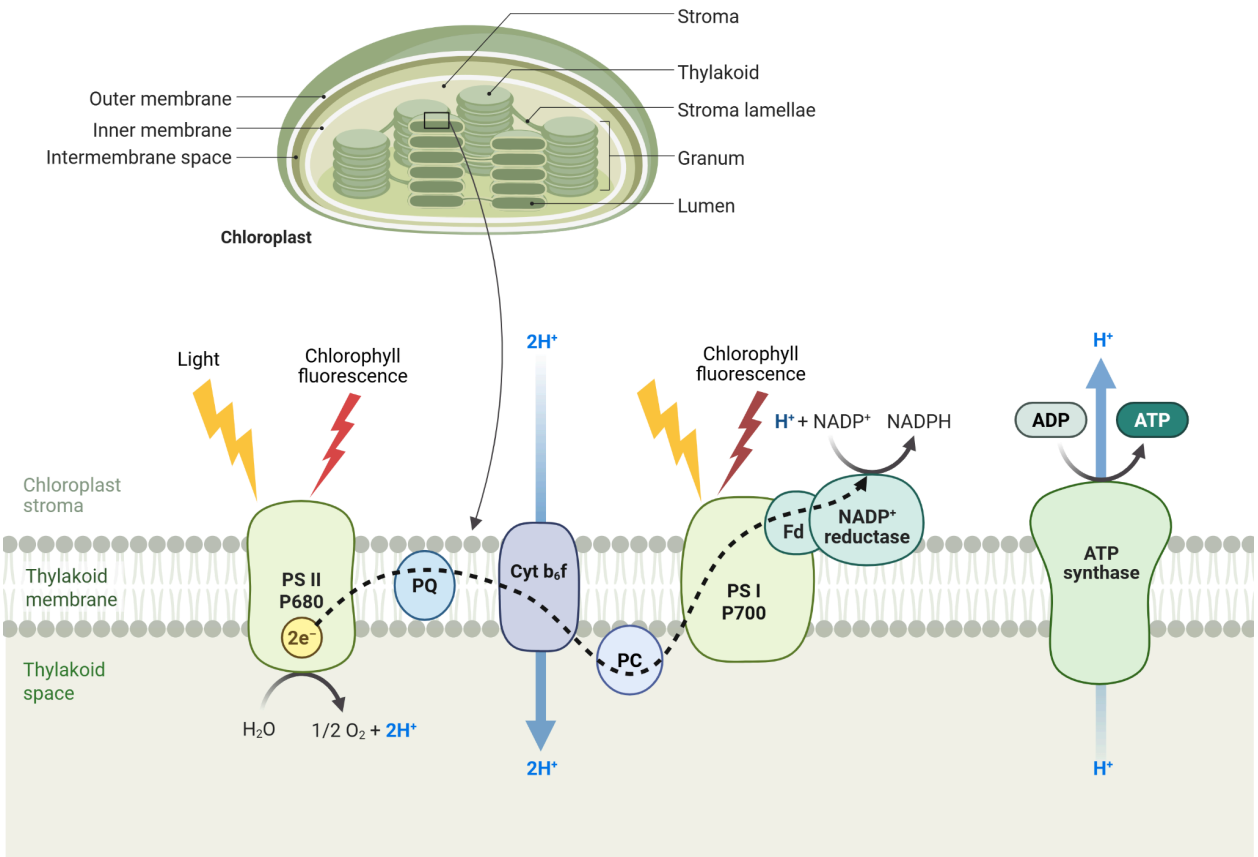

Figure 1.3 Light reaction of photosynthesis in higher plants. Photosystem II (PSII) and photosystem I (PSI) pigment-protein supercomplexes are embedded in the membrane of thylakoid, where they harvest light and facilitate electron transfer, emit chlorophyll fluorescence, producing oxygen, ATP, and NADPH. Created in https://BioRender.com

1.1.2. Light absorption and energy transfer

Photosynthetic pigments (Chl a, Chl b, and carotenoid) absorb the energy of light, and their typical spectra of absorption of light are shown in Figure 1.4. The (protein) environment of the pigments can shift and broaden the absorption spectrum of individual pigments due to changes of their vibrational energy states (Porcar-Castell et al., 2014). LHCs transfer energy efficiently to their associated reaction centers achieving about 95 to 99% by a non-radiative but distance dependent process from one molecule to another called Förster resonance energy transfer (FRET). This process funnels energy to the reaction center Chl a pigments with energy loss under the sequence of carotenoid, Chl b, and Chl a. Thus, the reaction centers can trap energy they got from antenna pigments and use less energy to achieve the excited state. The variety of LHCs reflects the need of balancing energy into the two photosystems and the adaptation to diverse environments (Taiz et al., 2015, p. 183).

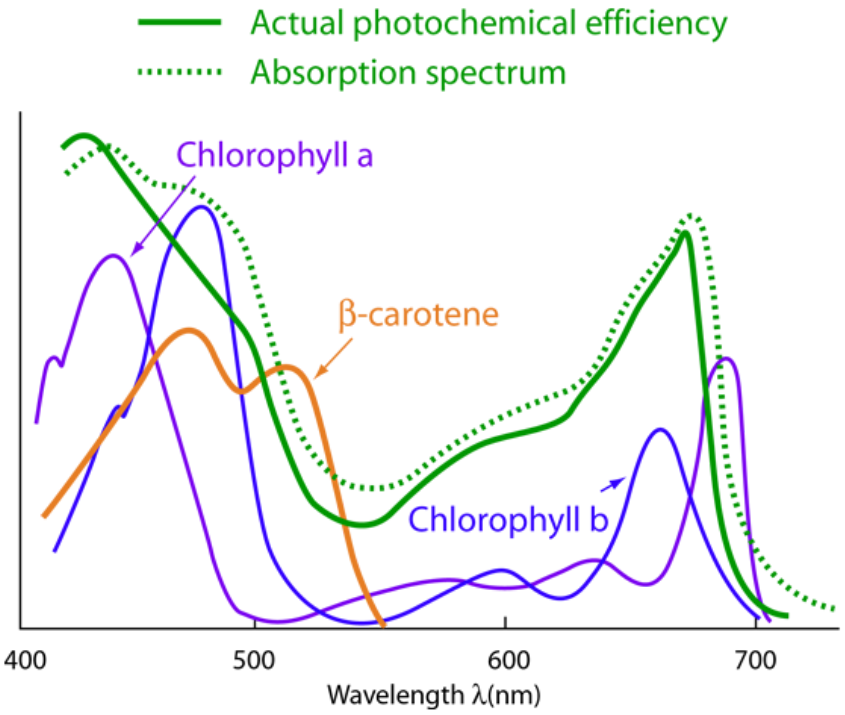

Figure 1.4 Absorption spectra of photosynthetic pigments. The photochemical efficiency is measured by measuring the amount of oxygen produced by leaves following exposure to various wavelengths (Moore, 1998, p. 138).

1.1.3. Chlorophyll a excitation and energy dissipation

Molecule excitation

Molecules have multiple electronic states corresponding to energy levels decided by quantized molecular orbitals and interactions of electrons. Within each electronic level there are vibrational energy states and each of these states can be

divided into rotational energy levels. A photon can be absorbed only if its frequency equals the difference of two energy levels, and this transition usually occurs from the ground electronic state with the lowest energy level to excited electronic state as well as vibrational state (Porcar-Castell et al., 2014). Chl a and Chl b transit from ground singlet state (S0) to the first excited singlet state (S1) by absorbing red light, and to the second or higher excited singlet state (Sn) by absorbing blue light. For carotenoids, only transition from S1 to Sn state is allowed (Ruban et al., 2022, p. 10). Due to the very efficient energy transfer from carotenoids and Chls b to Chls a, here the de-excitation of a Chl a is introduced by using a Jablonski diagram in Figure 1.5.

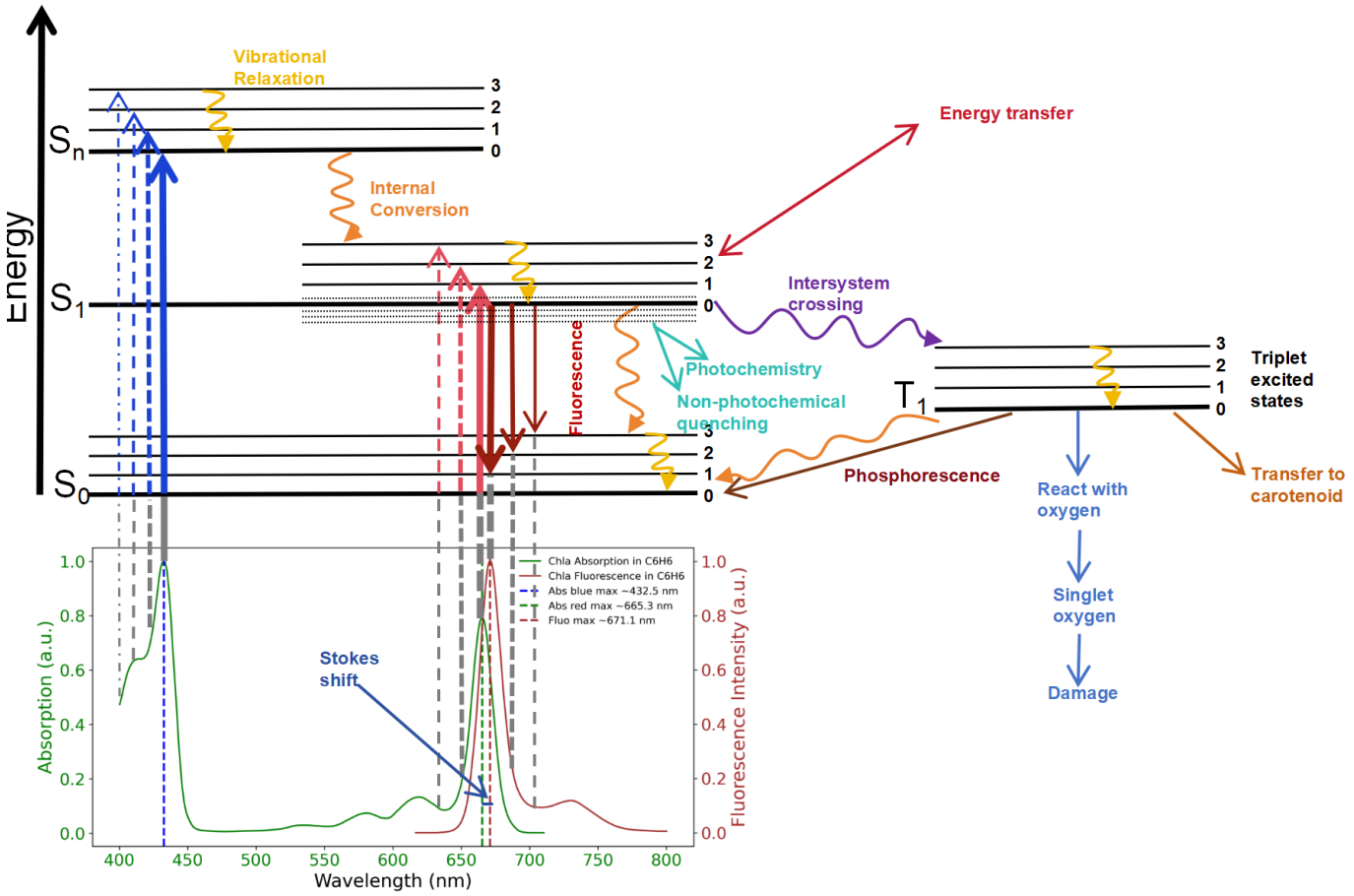

Figure 1.5 Idealized Jablonski diagram depicting the energy dissipation and energy partitioning of absorbed photons in a chlorophyll a molecule in the solvent of C6H6. The spectra of chlorophyll absorption and fluorescence emission were extracted from the database (Taniguchi and Lindsey, 2021) and origin from studies (Kobayashi et al., 2013).

Energy dissipation from second or higher states to first excited state

At molecule level, energy dissipation involves several stages and competing ways on different time scales (Croce and van Amerongen, 2020). Within one electronic state, vibrational relaxation dissipates energy between vibrational energy states

as kinetic energy. If vibrational energy levels strongly overlap electronic energy levels, which are usually greater than the S1, internal conversion happens from one electronic state to another lower electronic state. These two processes are mechanistically identical occurring just after absorbance. Excited Chls and carotenoids fall back to the lowest vibrational level of S1 within several hundreds of femtoseconds via vibrational relaxation and internal conversion. The lifetime of S1 for a carotenoid is around 10 picoseconds and for a Chl is around several nanoseconds (Ruban et al., 2022, p. 12).

Energy partitioning from first excited state to ground state of Chl a

In the absence of excitation energy transfer or electron transfer, isolated Chls a in solvent fall back from S1 to S0 via three pathways: (1) emitting a photon, a process called ChlaF with a typical rate constant of $k_f = 0.05\, ns^{-1}$, (2) internal conversion with a typical rate constant of of $k_{IC} = 0.02\, ns^{-1}$, or most likely (3) relaxing to a triplet state called intersystem crossing with a typical rate constant of of $k_{ISC} = 0.13\, ns^{-1}$. Chl a triplets are potentially dangerous to organisms because they can react with oxygen producing singlet oxygen which can damage cells. Thus, in photosystems normally every Chl a in the antenna is in contact with a carotenoid for transferring the energy efficiently preventing singlet oxygen (Ruban et al., 2022, pp. 12–13).

At the thylakoid and photosystem level, energy partitioning of Chls a in PSII has three main pathways: (1) PQ with rate constant k_{PSII} by transferring an electron to an acceptor for photosynthesis in reaction centers, (2) NPQ with rate constant k_{NPQ} which is any increase of thermal dissipation beyond basal thermal dissipation (minimal thermal dissipation in absence of stress and down regulation), (3) emission of ChlaF, and the basal thermal dissipation $k_D = k_{IC} + k_{ISC}$.

Photochemistry

Photosynthesis dynamics link with the fraction of the open and functional reaction centres of PS II (q), as well as depend on the connectivity of PS II centres that enable energy to move from closed to open ones. Two approaches can be used to estimate q based on two extreme models: (1) qP parameter based on fully separated PSII units, a puddle model, or (2) qL parameter based on fully connected PSII units, a lake model. The effective rate constant of photochemistry (k_P) can be expressed as qk_{PSII} where q can be either qP or qL depending on the connectivity model used and the maximum intrinsic rate constant of photochemistry k_{PSII}. Subsequently, the quantum yield of fluorescence emission

from PSII can be expressed in Equation (1.1) and the effective quantum yield of photochemistry in PSII (ΦP_{II}) can be expressed in the Equation (1.2) where $\Phi F_{II\_max} = \frac{k_F}{k_D+k_F+k_{NPQII}}$ is measured when q=0 without photochemistry by using herbicides, liquid nitrogen temperature or saturating light pulses (Porcar-Castell et al., 2021; Ruban et al., 2022, pp. 12–13).

$$\Phi F_{II} = \frac{k_F}{k_D+k_F+k_{NPQII}+qk_{PSII}} \quad (1.1)$$

$$\Phi P_{II} = \frac{qk_{PSII}}{k_D+k_F+k_{NPQII}+qk_{PSII}} = 1 - \frac{\Phi F_{II}}{\Phi F_{II\_max}} \quad (1.2)$$

Chlorophyll a fluorescence

At the molecular level, the emission spectrum of ChlaF is typically a mirror image of the absorption spectrum of the S0 to S1 transition shown in Figure 1.5, because the similar vibrational energy spacing in both S0 and S1 states as well as the Franck-Condon principle, the unchanged transition probability between two vibrational levels from the two electronic states. Thus, from the lowest vibrational level of S1 to S0 is an independent process of excitation wavelength. (Lakowicz and Masters, 2008, p. 8). The overlap of absorption and emission is due to the sub-levels of each vibrational level resulting in longer wavelength absorption. At the photosystem level, both PSI and PSII have capacity to fluorescence, but ChlaF from PSII typically exhibits more dynamics in quantum yield to photochemical and non-photochemical processes and dominates in the red region. At the leaf level and beyond, the light condition of the growing environment alters the photosystems composition, PSII and PSI stoichiometry, and physiological state. The reabsorption of emitted red SIF by Chls also alters the final captured leaf or higher level SIF entangled spectral properties of light-harvesting (Porcar-Castell et al., 2014).

1.1.4. Non-photochemical quenching

Plants adapt to light by minimizing the absorption and the excited state lifetime of chlorophyll through adjustments in chloroplast movement and light-harvesting mechanisms involving PQ, NPQ, and fluorescence. In this context, NPQ refers to the thermal quenching of the excited state of chlorophyll by quenchers without engaging in photochemistry. It reduces the excited state lifetime of chlorophyll, thereby preventing the formation of reactive oxygen species. Reduced absorption of light in PSII via chloroplast movement or/and LHCII movement from PSII to PSI (state transition) are not considered as NPQ due to no reduction of lifetime of excited Chls a. Classified by relaxation kinetics, NPQ has four pathways (Figure 1.6): energy-dependent quenching (qE),

zeaxanthin-dependent quenching (qZ), sustained antenna quenching (qH), and photoinhibitory quenching (qI). NPQ is primarily regulated by the protein environment and the xanthophyll cycle (Figure 1.6), which produces zeaxanthin across various time scales , depending on the location of violaxanthin (Puggioni, 2020).

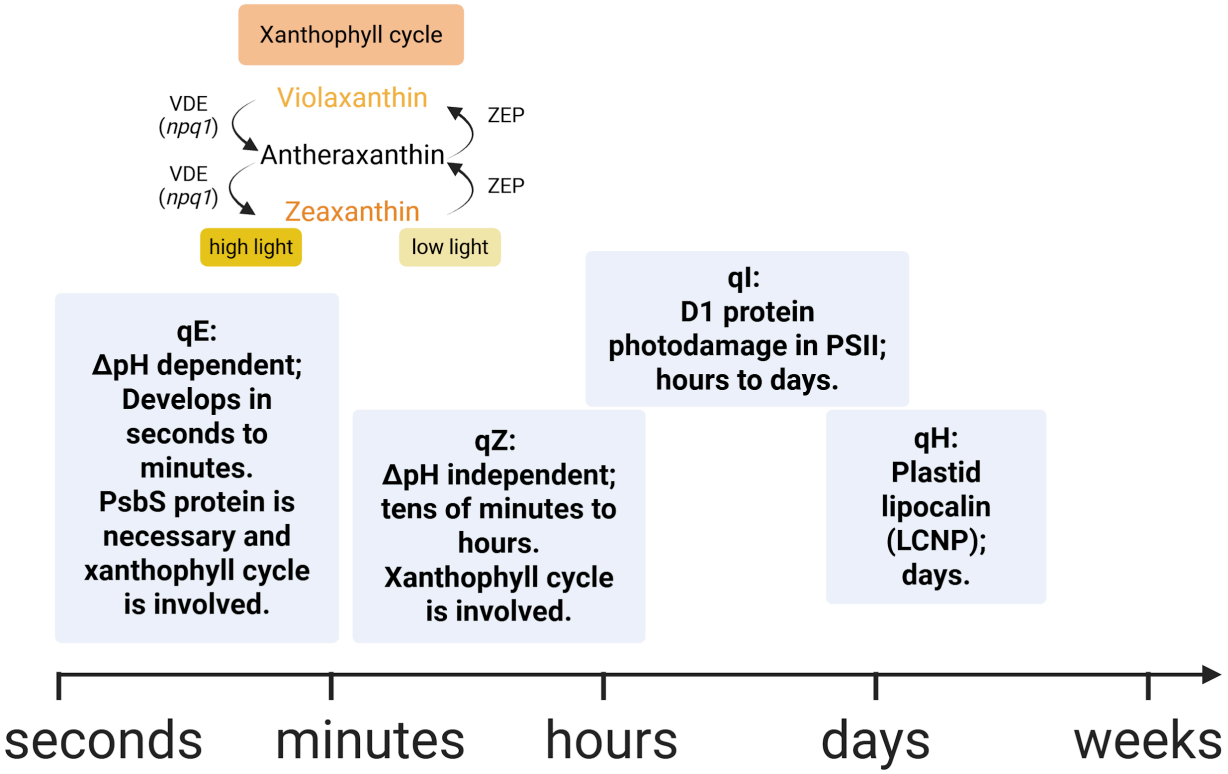

Figure 1.6 Five types of non-photochemical quenching pathways with differing response time. qE is energy-dependent quenching, qZ is zeaxanthin-dependent quenching, qT is state transition, qH is sustained antenna quenching, and qI is photoinhibitory quenching. PsbS refer to photoprotective proteins and LCNP refer to plastid lipocalin. Xanthophyll cycle involved in energy-dependent quenching (qE) and zeaxanthin-dependent quenching (qZ) in non-photochemical quenching processes. VDE is violaxanthin de-epoxidase, and *Arabidopsis thaliana npq1* mutant lacks the enzyme for this process. ZEP is zeaxanthin epoxidase and it is the reverse process of VDE. Created in https://BioRender.com

NPQ

In the short term (seconds to hours), NPQ is highly dynamic, regulated by several processes operating on different time scales. The qE is pH-dependent and involves two mechanisms: photoprotective proteins (PsbS) and the rapidly activated xanthophyll cycle. At the time scale of seconds, the PsbS protein functions as a pH sensor and is not stably associated with the PSII-LHCII supercomplex, which likely results in the dissociation of LHCII proteins from PSII. The LHC proteins subsequently aggregate, inducing conformational changes that

result in reduced energy transfer to reaction centers (Ruban and Saccon, 2022). On a time scale of 1-3 minutes, the pH of lumen also regulates the activity of the enzyme violaxanthin (Vx) de-epoxidase (VDE) (Figure 1.6), where a decrease in pH triggers the de-epoxidation of a specific pool of Vx, increasing zeaxanthin (Zx) content. Zx is associated with the quenching center of NPQ and promotes LHCII aggregation, facilitating excitation energy transfer from chlorophyll to nearby carotenoids. Additionally, a form of pH-independent NPQ called qZ is activated by accumulated Zx and prolonged excess light, developing within 10-20 minutes and relaxing within 10-60 minutes (Puggioni, 2020).

In the long term (hours to days), qI occurs when plants face sustained stress and do not recover overnight. qI is associated with PSII photoinhibition caused by apparent damage to the D1 protein in the PSII core reaction center considered as a safety valve for saving the downstream components from dangerous ROS. qI also promotes NPQ by involving the retention of Zx, PsbS, and aggregation of LHCs. The recovery rate is even lower with low temperatures (Porcar-Castell et al., 2014). Photoinhibition shows as a decrease in the the maximum quantum yield of photochemistry from PSII (ΦP_{max}), which can be estimated by fluorescence measurement. In contrast to PSII, the excited state lifetime of chlorophyll in PSI does not change significantly, and its reaction center is not easily damaged due to the high efficiency of photochemistry and protective mechanisms. However, PSI shows less efficient repair of the reaction center compared to PSII when damaged. Meanwhile, qH occurs with lower ΦP_{max} but without PSII photoinactivation due to the damage of D1 protein. The increased expression of plastid lipocalin (LCNP) protein is required for qH to occur during abiotic stress, which is differing from the known factors for other types of NPQ pathways (Malnoë, 2018).

Reduction of light absorption

Except for NPQ quenchers, chloroplast movement and state transition (qT) also reduce fluorescence via reduction of light absorption, which can be distinguished from true NPQ by decreased amplitudes of fluorescence other than shortened lift-time of fluorescence (van Amerongen and Croce, 2025).

After 10 minutes, chloroplast movement can be observed and may take from half-hour to a few hours (Kagawa et al., 2001). On the time scale of minutes, qT regulates the partitioning of energy between PSII and PSI by moving LHCII, resulting in changes in the light-harvesting capacities of photosystems (Wientjes et al., 2013). qT can balance the energy distribution between the two photosystems in natural environments to achieve optimal efficiency in electron transfer. In State 2, PSII is excited more, leading to the downregulation of the light-harvesting capacity of PSII and the upregulation of PSI. State 1 is the reverse.

1.2. Active measurements of chlorophyll fluorescence

ChlaF measurements using artificial light are considered active methods. A controlled light source with shorter wavelengths enables the measurement of the small amount of ChlaF emitted at longer wavelengths. To exclude the impact of ambient light, traditional pulse-amplitude modulated (PAM) fluorimetry (Schreiber et al., 1986) for leaf level and the light-induced fluorescence transient (LIFT) method (Kolber et al., 2005) for canopy level are the two main active techniques. These techniques were used in Chapter 3.

1.2.1. Traditional pulse-amplitude modulated fluorometry

The theoretical principle of PAM is based on the weak and pulsed constant amplitude of modulated measuring light, which can just excite chlorophyll molecules but cannot induce photosynthesis. The lock-in amplifier allows the PAM detector to receive only the effective quantum yield of fluorescence induced by measuring light (Figure 1.7(a)), without interfering from fluorescence induced by ambient light or actinic light which can induce photochemistry. Assuming fluorescence from PS I is constant or negligible, PAM fluorometers are typically used to estimate the quantum yield of photochemistry and the NPQ status from PS II (Porcar-Castell et al., 2014). The most commonly used parameter is the maximum quantum yield of photochemistry from PSII (Fv/Fm), which is calculated by Equation (1.3) after dark-adaption which relaxes all reversible NPQ. The principle is demonstrated in Figure 1.7(b).

$$\Phi P_{max} = \frac{F_m - F_o}{F_m} = \frac{F_v}{F_m} \quad (1.3)$$

F_o is the minimum modulated fluorescence emitted under the measuring light only, assuming NPQ is zero and the PSII is with full capacity for photochemistry after dark adaption. F_m is the maximum modulated fluorescence when a saturation pulse is applied, where NPQ is still zero, but the PS II reaction center is fully closed. For the light adapted plants, where NPQ plays a role in energy quenching, the steady-state fluorescence (F_s) can be measured under actinic light, and the maximal fluorescence in the light-adapted state (F_m') is measured by applying a saturating pulse, which transiently closes all the reaction centres. The quantum efficiency of PSII in light, namely PSII operating efficiency (ΦP), can be expressed in Equation (1.4).

$$\Phi P = \frac{F_m' - F_s}{F_m'} = \frac{F_q'}{F_m'} \quad (1.4)$$

Combining time series measurements, PAM fluorometry provides parameters with the capabilities to track the changing of status of PSII and NPQ under

varying physiological status and environmental conditions (Maxwell and Johnson, 2000; Murchie and Lawson, 2013). Nowadays, PAM is not limited to point measurements or greenhouses. Imaging PAM fluorometers (Figure 1.7(c)) are available for detecting spatial features from leaves or small plants, and long-term PAM fluorometers can stay in the field to monitor the status of leaves across seasons. However, the requirement to deliver saturating flashes from PAM to the canopy level limits its application at larger scales.

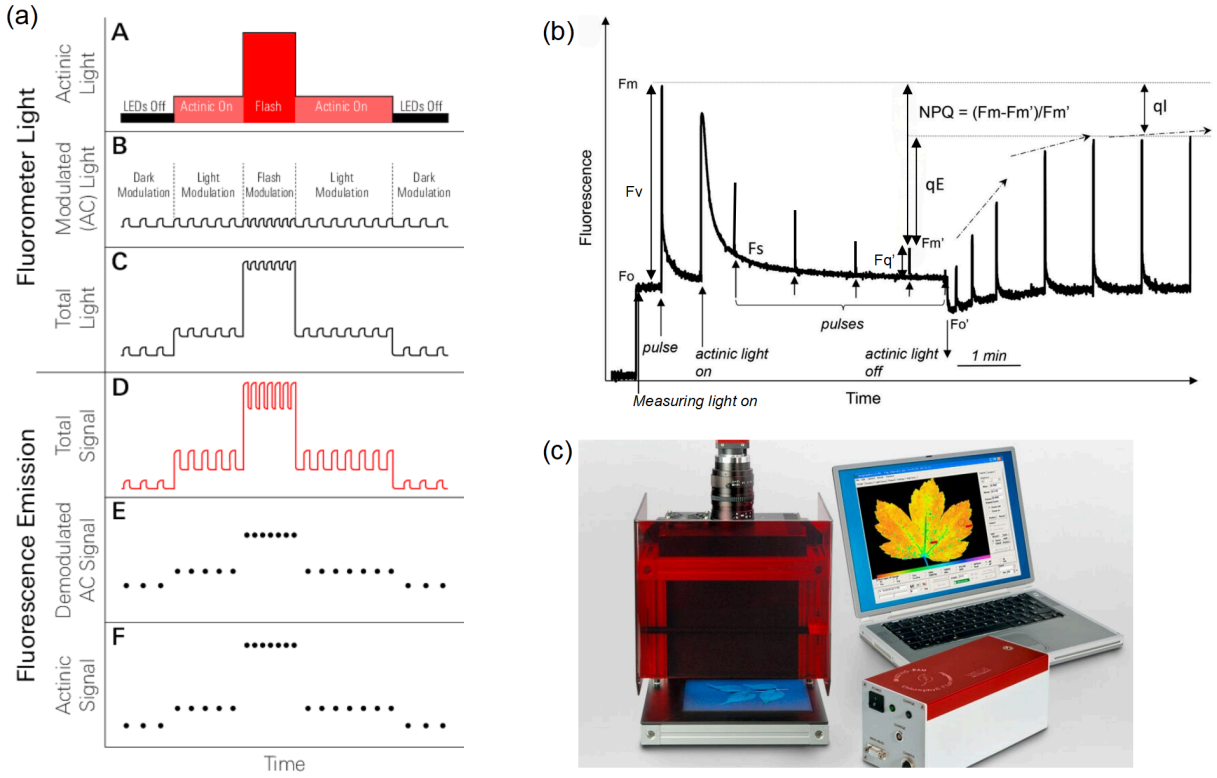

Figure 1.7 Pulse-amplitude modulated fluorometry (PAM) technique. (a) The principle of retrieve fluorescence from modulated measuring light by subtracting the fluorescence signal shortly before or after a measuring pulse from the fluorescence signal during this measuring pulse(figure is borrowed from Li-Cor Biosciences, https://www.licor.com/support/LI-6800/topics/theory-fluorescence.html). (b) Typical fluorescence showing induction and relaxation of NPQ. Fm and Fo are the maximum and minimum fluorescence levels in the dark before actinic light illumination, respectively. Fs and Fm' are the steady-state fluorescence, maximum fluorescence during actinic light illumination, respectively. Fv = Fm-Fo and Fq' = Fm'-Fs. qE and qI are quickly and slowly reversible components of NPQ, respectively (figure was taken and modified from (Ruban, 2016)). (c) The MAXI version of IMAGING-PAM for imaging maximum photosynthetic efficiency. (credit: Walz, Effeltrich, Germany)

1.2.2. Light-induced fluorescence transient

To overcome the impractical high intensity of saturation pulse applied on canopy by traditional PAM, LIFT was developed for canopy-scale remote measurements

in open fields. It can measure the efficiency of photosynthetic light utilization, the quantum efficiency of PS II, and the kinetics of photosynthetic electron transport based on the principles of fast repetition rate fluorescence (FRRF) (Kolber et al., 1998). Without additional saturating light pulse, sub-saturating (actinic) measuring flashlets induces fluorescence transient to estimate the reduction status of the primary quinone electron acceptor plastoquinone A (Q_A) in PS II, allowing for the extraction of photosynthetic parameters such as F_s and F_m' under background irradiance from fully reduced Q_A by curve fitting. When measuring under dark condition for dark adapted plants, F_0 and F_m can also be measured respectively. LIFT observations showed good consistency with PAM measurements, except under high ambient illumination conditions (Acebron et al., 2021; Kolber et al., 2005). The LIFT (Version LIFT-REM, Soliense Inc., New York, USA) used in Section 3.3.2 also has a STS-VIS spectrometer (Ocean Optics, Florida, USA) and two RGB cameras (FLIR Solutions Inc., British Colombia, Canada) which can also provide vegetation indices simultaneously to fluorescence measurements. Figure 1.8 shows the LIFT in the laboratory and outdoors. However, LIFT measurements are still limited to canopy scales, not regional or global scales.

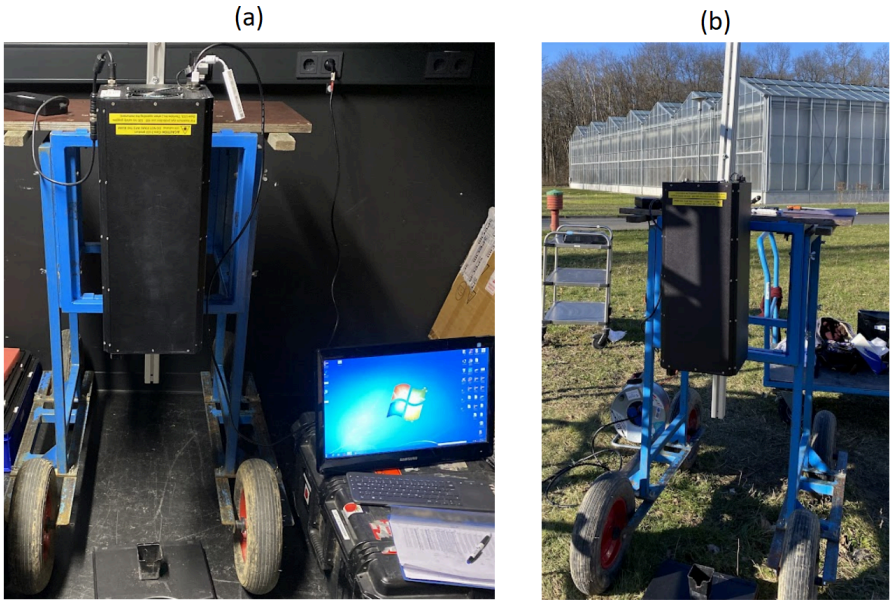

Figure 1.8 The LIFT instrument in the laboratory and outdoors. (a) LIFT in the dark laboratory for measuring maximum photosynthetic efficiency from dark-adapted plants. (b) LIFT outdoors for measuring PSII operating efficiency from plants under ambient illumination.

1.3. Solar-induced chlorophyll fluorescence measurement*

SIF is a relatively small signal superimposed on the reflected radiance of plants (Mohammed et al., 2019), so measuring SIF is challenging from the perspective of optics. Therefore, SIF is commonly retrieved by taking advantage of solar or the Earth's atmospheric absorption bands where irradiance transmission through the atmosphere is low (Cendrero-Mateo et al., 2019; Meroni et al., 2009). For proximal sensing, the typically used spectral bands for SIF retrieval are Earth's atmosphere telluric oxygen absorption bands (O_2B (687–692 nm) and O_2A (759–770 nm)) because their strongest absorption features around 687 nm and 760 nm are close to the SIF emission peaks Figure 1.9 (a). Therefore, red (F687) and far-red (F760) SIF can be retrieved at these two oxygen absorption bands due to their relatively higher contribution to the apparent reflectance (Figure 1.9 (b)) at these two bands than other bands (Cendrero-Mateo et al., 2019).

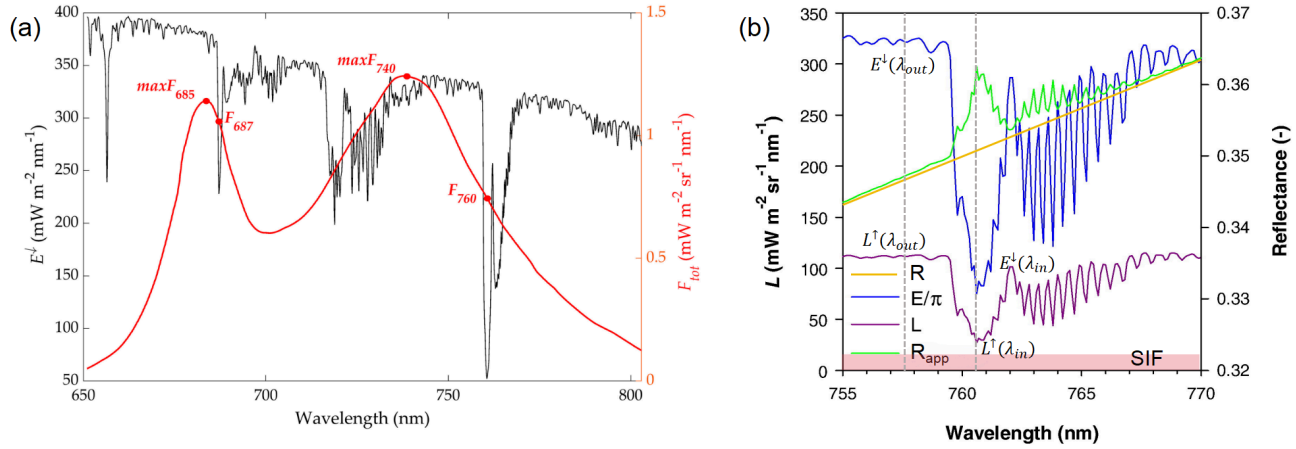

Figure 1.9 Principle of using oxygen absorption bands for SIF retrieval. (a) The two SIF emission peaks are near the O_2B and O_2A absorption bands (borrowed from (Cendrero-Mateo et al., 2019)). (b) Contribution of SIF to apparent reflectance (R_a□□) through in-filling of the O_2A band (adapted from (Meroni et al., 2010).

1.3.1. SIF measurements systems*

Since SIF only represents a fraction of the radiance measured by a sensor, high spectral resolution, high signal-to-noise ratio (SNR) (Damm et al., 2011), high instrument dynamic range as well as adequate measurement protocols and sensor calibration are required for reliable SIF retrieval (Cendrero-Mateo et al., 2019; Medina et al., 2019; Pacheco-Labrador et al., 2019).

At the leaf level, the FluoWat system uses a short-pass filter that cuts off irradiance above 650 nm and measures SIF with a hyperspectral spectroradiometer. In this way, the full SIF spectrum can be captured (Van Wittenberghe et al., 2015). At the landscape level, airborne push-broom imaging spectrometers (e.g., HyPlant) (Rascher et al., 2015; Siegmann et al., 2019) and

unmanned aerial vehicles (UAVs) equipped with imaging (Kneer et al., 2023) and point spectrometers (Bendig et al., 2020; Chang et al., 2020; Wang et al., 2021) are essential for bridging the SIF measurement from regional to the satellite. For the scaling gap between leaf and regional, existing proximal point spectroradiometer systems such as PICCOLO DOPPIO (Arthur et al., 2014), FloX (Julitta et al., 2016), PhotoSpec (Grossmann et al., 2018), FluoSpec(Yang et al., 2018), FluoCat (Moncholi-Estornell et al., 2023) were developed. However, these point spectroradiometers have limited suitability when investigating spatial dynamics of SIF among leaves and within a plant canopy, as the signal is always an integration of the field of view of the sensor. Hyperspectral imaging systems are needed to quantify spatial dynamics of SIF with additional information, such as fractional vegetation cover, leaf angles and orientations, sunlit and shaded parts of the canopy, and leaves with differing ages.

Some studies have successfully retrieved F760 from imaging systems (Fu et al., 2021; Jiang et al., 2020; Kneer et al., 2023; Pinto et al., 2017, 2016), and there are recent developments both from academia (Wang et al., 2024) and companies (Ruehr et al., 2024). Their measurements showed spatial and temporal variation of far-red SIF responding to herbicide stress, canopy structure and absorbed photosynthetically active radiation (APAR), corroborating the need of SIF high-spatial-resolution imagery to overcome the challenge of linking top-of-canopy (TOC) fluorescence with leaf-level photosynthetic efficiency, as listed in Porcar-Castell (2021). However, ground measurements of red SIF have been challenging due to limited spectral resolutions and signal-to-noise ratios of previous imaging spectrometers which also limit the precision of far-red SIF. Nevertheless, to characterize the contributions of PSII and PSI to the total ChlaF emission and, consequently, to understand the dynamics of ChlaF and photosynthesis, the measurement of both F687 and F760 is mandatory (Ač et al., 2015; Rossini et al., 2016; Zeng et al., 2022a). The new-generation HyScreen system with two sensors was developed following its earlier version (Pinto et al., 2016)to meet the demand for retrieving both red and far-red SIF as well as vegetation indicies. Detailed specifications of the sensors, measurement protocol, and data processing chain are presented in Chapter 2.

As SIF is interrelated to photochemistry and NPQ, it is highly dynamic to the status of the photosystem, which is controlled by the plant's physiological status and the biotic and abiotic factors, especially the light condition. To understand the connection of SIF to photosystem activities, high spatiotemporal resolution of SIF is necessary. Meanwhile, even SIF can be sensed from ground-based instruments up to satellites, but there is still a gap in understanding the downscaling of TOC SIF to leaf-level SIF (Mohammed et al., 2019; Siegmann et al., 2021). Canopy architecture influences how absorbed photosynthetically active radiation (APAR) changes within the canopy (Pinto et al., 2016; Yang and van der Tol, 2018) and

how leaf-emitted SIF is scattered and re-absorbed in the canopy. Leaves located at different vertical locations within the canopy decide their physiological status as a response to the environment (Yang et al., 2021). Furthermore, viewing geometry influences measured SIF (Damm et al., 2015). Physically based radiative transfer models can help with understanding these processes, but measured data are mandatory to validate modelled results or as input data to parameterize models (Kallel, 2020). Thus, hyperspectral imaging techniques are needed to quantify the dynamics of SIF as well as capturing the structure of plants.

1.3.2. SIF retrieval methods

SIF retrieval methods are rooted in the Fraunhofer line in-filling principle, which describes the additive contribution of SIF to the at-sensor radiance (Guanter et al., 2021). For satellite-based remote sensing of SIF, where atmospheric effects are substantial, two main approaches are commonly applied: (1) physically based methods that use explicit radiative transfer modeling (Köhler et al., 2015), and (2) data-driven methods that empirically quantify atmospheric effects using SIF-free reference data (Guanter et al., 2012).

For proximal sensing of SIF, where atmospheric effects on upwelling radiance ($L\uparrow$) are limited, the most widely used methods are the Fraunhofer line depth (FLD) principle and the spectral fitting method (SFM), both of which exploit the oxygen absorption features near 760 nm and 687 nm (Cendrero-Mateo et al., 2019).

The irradiance ($E\downarrow$, in units of radiant flux per unit projected area per wavelength e.g., $mWm^{-2}\ nm^{-1}$) arriving at the TOC represents solar radiation after passing through the atmosphere, including Fraunhofer and other absorption features. Equation (1.5) shows that upwelling radiance ($L\uparrow$, in units of radiant flux per unit projected area per unit solid angle per wavelength e.g., $mWm^{-2}\ sr^{-1}nm^{-1}$) consists of both reflected radiance (L_R) and SIF (F), where L_R can be represented as the product of reflectance (R) and $E\downarrow$. Consequently, the apparent reflectance R_{app} (Equation (1.6)) contains both the true canopy reflectance and an additional fluorescence term $F/E\downarrow$, which increases $E\downarrow$ decreases while R and F remain relatively constant within a narrow spectral window.

$$L\uparrow(\lambda) = L_R(\lambda) + F(\lambda) = \frac{R(\lambda)\cdot E\downarrow(\lambda)}{\pi} + F(\lambda) \quad (1.5)$$

$$R_{app}(\lambda) = \frac{\pi\cdot L\uparrow(\lambda)}{E\downarrow(\lambda)} = R(\lambda) + \frac{\pi\cdot F(\lambda)}{E\downarrow(\lambda)} \quad (1.6)$$

FLD methods exploit the differential contribution of F to the $L\uparrow$ inside and outside of an absorption band Figure 1.9 (b). With known $E\downarrow$, assuming constant R and F, the simple FLD (sFLD) method uses one spectral band inside and one outside the oxygen absorption feature to retrieve F. The three-band FLD (3FLD) overcomes

these assumptions by using one inside and two outside bands to linearly interpolate R and F. The improved FLD (iFLD) method applies correction factors to account for the non-linear behavior of R and F. To retrieve the full SIF spectrum, SFM can be applied, which separates SIF and reflectance from high-resolution radiance and irradiance spectra by fitting mathematical functions representing the shape of R and F (Cendrero-Mateo et al., 2019). In this study, the iFLD method(Section 2.3.6) was used for SIF retrieval due to its reasonable assumptions and faster computational performance compared with SFM.

1.3.3. SIF yield

SIF can be approximated by the following Equation (1.7) where $fPAR$ is the fraction of absorbed PAR , ΦF is the quantum yield of chlorophyll a fluorescence, and f_{esc} is the escape probability caused by pigments reabsorption (Zeng et al., 2019).

$$SIF(\lambda) = PAR * fPAR * \Phi F(\lambda) * f_{esc}(\lambda) \quad (1.7)$$

1.4. SIF as an indicator of stress in the photosystem II

Plants can regulate the energy absorbed and transferred to PSII responding to light conditions according to their status, thus PQ and NPQ are highly dynamic and can be reflected by ChlaF. As the SIF signal is an optical signal reflecting the status of photosystems in real time under natural illumination, tracing the dynamics of SIF over time can help us to understand the plasticity of plants under stress, particularly over short periods that cannot be captured by changes in structure or pigment-based vegetation indices. However, interpreting dynamic SIF with respect to stress across space and time is not intuitive, which hinders the application of SIF for stress monitoring and stress-tolerant variety selection.

Many stresses trigger the need for photoprotection in plants, activating multiple mechanisms over short time spans. These include increased leaf inclination angles, chloroplast movement to enhance light transmission, and other physiological changes such as NPQ and the movement of LHCII from PSII to PSI. Previous studies demonstrated that environmental conditions and physiological status of plants can result in a positive or negative relationship between ΦF and ΦP depending on NPQ status (Porcar-Castell et al., 2021).

A classical experimental approach for monitoring the PSII via SIF involves the use of the herbicide (3,4-dichlorophenyl)-1,1-dimethylurea (DCMU) to inhibit the PSII electron transport chain. In an experiment on grass, treatment with DCMU for 40 minutes resulted in significantly higher red and far-red SIF compared to untreated plants, while the NDVI for both untreated and DCMU-treated plants remained similar (Rossini et al., 2015). Similarly, Pinto et al. (2016) conducted a

DCMU experiment in a cornfield and demonstrated that DCMU-treated maize exhibited higher far-red SIF than untreated maize after 1 hour. The findings of the two studies indicated an inverse relationship between SIF and ΦP. Conversely, under conditions of combined excessive light and low temperature, a positive correlation between ΦF and ΦP was observed with sustained NPQ (Ensminger et al., 2004). It is evident that NPQ must be considered simultaneously to better understand energy partitioning in PSII.

1.4.1. Cold stress

Maximum photosynthesis occurs within a narrow temperature range, known as the photosynthetic thermal optimum. Species evolved in, or the same species grown under different temperature conditions normally show varying optimal temperature ranges. Plants growing over a wider range of temperature demonstrate higher thermal plasticity. Low temperature is a major stress factor affecting crop production. At low temperatures, the demand for triose phosphates for starch and sucrose synthesis decreases, resulting in limited inorganic phosphate uptake into the chloroplasts for photosynthesis (Taiz et al., 2015). In the context of climate change, breeders must select cultivars with high thermal plasticity and high tolerance of low temperature to optimize crop production.

Plants can be affected by cold stress in different ways. These include the consideration of temperature range, duration, and the interaction of cold stress with other stresses. The temperature range separates chilling, which slows down metabolism, from freezing (temperature below 0°C), which induces ice formation and slows down metabolism severely (Baker and Rosenqvist, 2004). By duration and dynamics, acute cold events happen suddenly with rapid temperature drops, while long-term low temperatures prolong days to weeks, which produce cumulative damage if acclimation is incomplete or growth is strongly limited (cold-shifted), or allow cold acclimation with new developed leaves. The cold acclimation process exposes plants to non-freezing low temperatures to increase subsequent freezing tolerance (Gray et al., 2003). When cold stress coincides with high light, it causes strong pressure on PSII and rapid induction of NPQ and photoinhibition if repair is limited (Velitchkova et al., 2020).

1.4.2. SIF to study the response of plants to cold stress

Plants respond to cold stress differently via either partitioning excess excitation more to photochemistry or more to protective processes due to their different natural habitat and growth regimes (Khanal et al., 2017). Adjustments in PQ and NPQ result from reversible PQ and NPQ as well as sustained NPQ depending on the extent and timing of cold stress (Porcar-Castell, 2011). However, previous studies usually use active ChlaF to monitor the energy partitioning, which lacks the ability of scaling up for larger scale application. To bridge the gap, Acebron et

al. (2021) investigated energy partitioning especially photoinhibition of Arabidopsis with different capacity of reversible NPQ under cold stress by combining SIF and reflectance with active measurements. However, the point spectrometer prevented resolving the leaf level spatial SIF and reflectance and measuring simultaneously of all the genotypes, which limited the comparison of leaves with different physiological status and excluded the effects of PAR completely when comparing genotypes.

1.4.3. Leaf age-dependent cold stress responses

Young leaves are different from mature leaves in morphology, physiology, and biochemistry. They are more susceptible to photoinhibition due to their developing photosystems. However, to cope with the excess of energy, their NPQ is highly active to protect them from photodamage caused by reactive oxygen species (ROS). In *Arabidopsis*, young leaves maintain their Fv/Fm and prevent photo-oxidative stress via alternative strategies, such as light shielding by anthocyanins. Young leaves and young plants can activate NPQ much faster than older leaves to prevent leaf bleaching, and have higher ROS scavenging capacity (Rankenberg et al., 2021).

1.5. Objectives of this thesis

The objectives of this study are: (1) to develop measuring protocols and data processing chains of a hyperspectral imaging system for SIF and vegetation indices retrieval; (2) to investigate how the extent and timing of cold stress affects energy partitioning in PSII across *Arabidopsis* genotypes with differing NPQ capacities and between mature and young leaves by combining SIF, VIs, and active ChlaF.

2. Novel ground-based hyperspectral system measuring solar-induced chlorophyll fluorescence*

Parts of this chapter have been published in peer-reviewed journals:

Huaiyue Peng, Maria Pilar Cendrero-Mateo, Juliane Bendig, Bastian Siegmann, Kelvin Acebron, Caspar Kneer, Kari Kataja, Onno Muller, and Uwe Rascher. 2022. "HyScreen: A Ground-Based Imaging System for High-Resolution Red and Far-Red Solar-Induced Chlorophyll Fluorescence" Sensors 22, no. 23: 9443. https://doi.org/10.3390/s22239443

The table below indicates the origin of different sections within this chapter:

Newly added	Adapted *	Original
Figure 2.2 Figure 2.4 Figure 2.8 - 2.17 Table 2.3 - 2.5	Section 2 Section 2.1 Section 2.3 Section 2.3.2 Section 2.3.4 - 2.3.7 Section 2.4 Section 2.4.1 Section 2.4.2	Everything else

In this chapter, the HyScreen imaging spectrometer system will be introduced. The system allows the retrieval of red and far-red fluorescence close to the canopy, where single leaves can be spatially resolved. HyScreen consists of two high-spatial- and high-spectral-resolution imaging spectrometers. One allows the retrieval of red chlorophyll fluorescence (F_{red}) of far-red chlorophyll fluorescence (F_{farred}), and the other is used for calculating vegetation indices and characterising PAR. This chapter presents a detailed technical description of HyScreen, introduces the data acquisition protocol and gives insights into the developed processing chain. A case study with structurally simple *Arabidopsis* is presented to illustrate the performance of HyScreen. Finally, measurement uncertainties are discussed. The initial system description was in (Peng et al., 2022), but the protocol and processing chain were updated when processing the data in this thesis.

2.1. Hyperspectral sensors*

The HyScreen system consists of two push-broom imaging spectrometers: the fluorescence sensor (FLUO) and the visible and near-infrared (NIR) sensor (VNIR). This system was built and developed by Forschungszentrum Jülich in cooperation with SPECIM (Spectral Imaging Ltd., Oulu, Finland) as part of the German Plant Phenotyping Network (DPPN). Figure 2.1.(a) shows the detailed components of the system. Both cameras are mounted side-by-side on a scanning bar to create an overlapping field of view (FOV) and synchronous movement. The system has a main, compact power and control unit (PCU), which is connected to both the VNIR and FLUO sensors. In addition, each sensor has its own PCU and corresponding data acquisition computer (DAC), which includes data acquisition software. With this setup, the HyScreen system can be mounted on a scaffolding (Figure 2.1(a)) or a mobile platform in the field (Figure 2.1(b)).

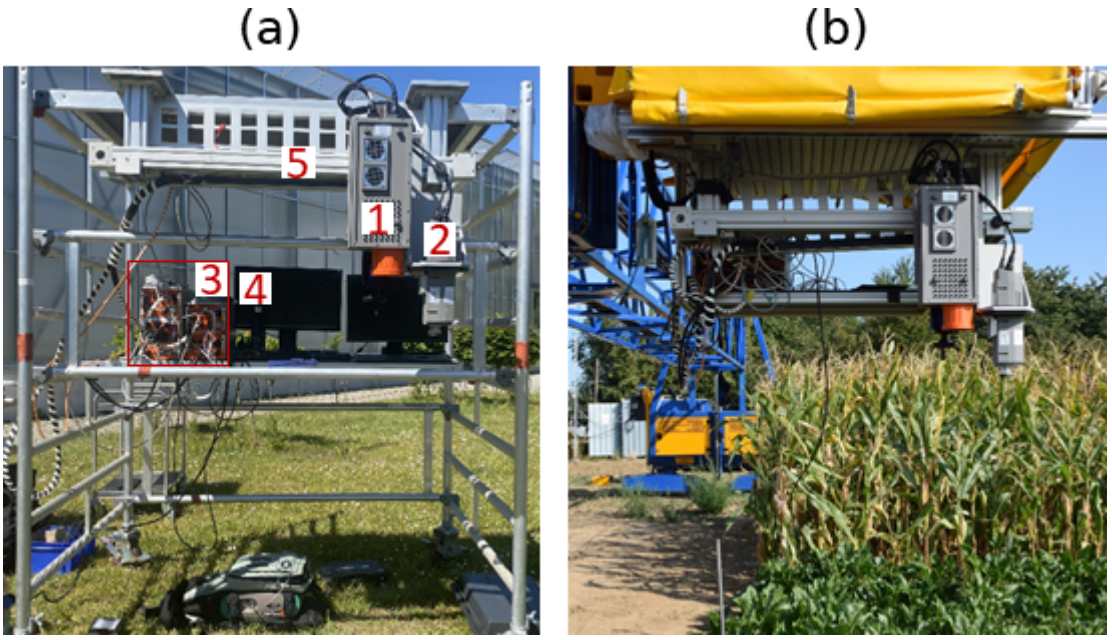

Figure 2.1 Overview of the HyScreen system: (a) HyScreen mounted on a movable scaffolding with components noted in numbers. Legend: 1. fluorescence sensor (FLUO), 2. visible and NIR sensor (VNIR), 3. power and control units (PCUs) and data acquisition computers (DACs) of the two sensors, 4. displays, and 5. linear axis. (b) HyScreen mounted on the mobile field phenotyping platform.

The main components of HyScreen are the imaging spectrometers. The VNIR module has a high-speed complementary metal-oxide semiconductor (CMOS) sensor. It covers the spectral range from 400 nm to 1000 nm with a mean spectral sampling interval of 0.78 nm and a mean full width at half maximum (FWHM) of 3.21 nm. The FLUO module has a scientific CMOS (sCMOS) detector. It covers the spectral range from 670 nm to 780 nm with a mean spectral sampling interval of 0.055 nm and a mean FWHM of 0.31 nm. The detailed characteristics of the two spectrometers are shown in Table 2.1.

Table 2.1 Characteristics of the fluorescence sensor (FLUO) and the visible and near-infrared sensor (VNIR) imaging spectrometers of HyScreen. The VNIR module measures in the visible and NIR spectral range, while the FLUO module, with its very fine spectral resolution, only covers the visible red and NIR spectral range and was specifically designed to retrieve SIF. FWHM stands for full width at half maximum.

Sensor	**VNIR**	**FLUO**
Sensor type	CMOS	sCMOS1
Dynamic range (bit)	12	14
Spectral range (nm)	400-1000	670-780
Mean spectral	0.79	0.06

sampling interval (nm)		
Mean spectral resolution (FWHM) (nm)	3.21	0.31
Field of view (FOV) (°)	32.71	32.24
Spatial pixels	1312	1512
Standard measurement setup[2]		
Spectral binning	2	2
Spectral sampling interval (nm)	1.46-1.61	0.1-0.12
Spectral resolution (FWHM) (nm)	2.42-4.35	0.36 at O_2B/0.40 at O_2A
Number of bands	384	1004
Spatial binning	2	4
Spatial pixels	656	378
Swath width of the sensor mounted 1 m above canopy (mm)	587	578
Frame rate (fps)	20	10
Exposure time range (ms)	0.1-50	0.1-100
Power consumption (W)	80	115
Input voltage (V)	12	12

[1]sCMOS: scientific CMOS chip—chip technology that combines high signal-to-noise ratio, wide dynamic range and fast frame rates with linear sensitivity. [2] To improve the SNR, the spatial and spectral binning of the VNIR module are set to 2, while the binning of the FLUO module is set to 4 in the spatial dimension and 2 in the spectral dimension.

2.2. Measurement protocol*

HyScreen can be used from two different measurement platforms: it can be installed (1) on a scaffolding at a height of 1.4 m of FLUO and a fixed height of 1.2 m of VNIR above ground (Figure 2.1(a)) or (2) on a mobile gantry system for phenotyping, where the distance between the sensors and the measurement

object is adjustable from 1 m up to 3 m above ground (Figure 2.1(b)). During measurement, the geometry of the sun, target and sensor have to be considered to avoid shadows from the platform being cast on targets. The sensors are mounted in the nadir position and levelled. Spatial and spectral binning, frame rate, integration time, scanning speed, dark-current measurements and measurement range are controlled by the manufacturer's proprietary software. Two sensors move simultaneously from the beginning of the linear axis to any point on the axis using a motor. Two images from FLUO and VNIR with a shared field of view can be produced by scanning lines and moving the sensors along the target. During data acquisition, the signal level is monitored by a live view that can also display saturated pixels.

Table 2.1. shows the standard measurement parameters, including the spatial and spectral binning options. To improve the SNR, the spatial and spectral binnings of the VNIR module are set to 2, while the binning of the FLUO module is set to 4 in the spatial dimension and to 2 in the spectral dimension. When measuring at a distance of 1 m between targets and sensors, the spatial resolutions of the FLUO and VNIR pixels are 1.53 mm and 0.89 mm, respectively. The frame rates of the VNIR and FLUO modules are 20 and 10 frames per second (fps), with maximum integration times slightly less than 50 and 100 ms, respectively. To acquire square pixels, the scanning speed is determined by the sensor–target distance and the acquisition frame rate. To focus the sensors, we use a sheet with black and white stripes before measurement whenever adjusting the height of the sensors. Additionally, 100 dark frames are recorded by closing the electro-mechanical shutter before each measurement. The average dark current is later subtracted from the raw data.

Solar downwelling radiance of HyScreen is derived by measuring calibrated Lambertian diffuse reflectance reference panels made from Zenith Polymer® (SphereOptics GmbH, Herrsching, Germany) placed at the beginning of the scanning area. To obtain the highest possible SNR of vegetation objects, it is recommended to use the panel with reflectance less than 50%. Meanwhile, at least two panels with differing reflectance are necessary for operating empirical line correction of reflected radiance for interpolating downwelling radiance. To avoid stray light across the FOV and spectrum, using strip panels that can cover the whole FOV is recommended other than putting light objects and dark panels together. During data acquisition, the reference panels should be horizontally levelled in the principal plane and kept free from shadows.

2.3. Image processing chain*

The HyScreen data processing chain consists of four clusters, as shown in Figure 2.2 The first cluster summarizes how spectral and radiometric calibration files complement the raw data consisting of the hyperspectral data cubes and header

files. The second cluster describes the transfer of raw hyperspectral image cubes recorded by the VNIR and FLUO modules to TOC upwelling radiance, downwelling radiance, and reflectance. Self-developed software using MATLAB 2021a is used for dark-current subtraction, radiometric calibration, point spread function (PSF) (Scharr et al., 2021) correction and Empirical Line Method (ELM) correction (Smith and Milton, 1999), converting at-sensor radiance into TOC radiance and reflectance values. The third cluster calculates vegetation indices from data recorded by the VNIR module, while the fourth cluster includes SIF retrieval at 687 and 760 nm based on the iFLD method.

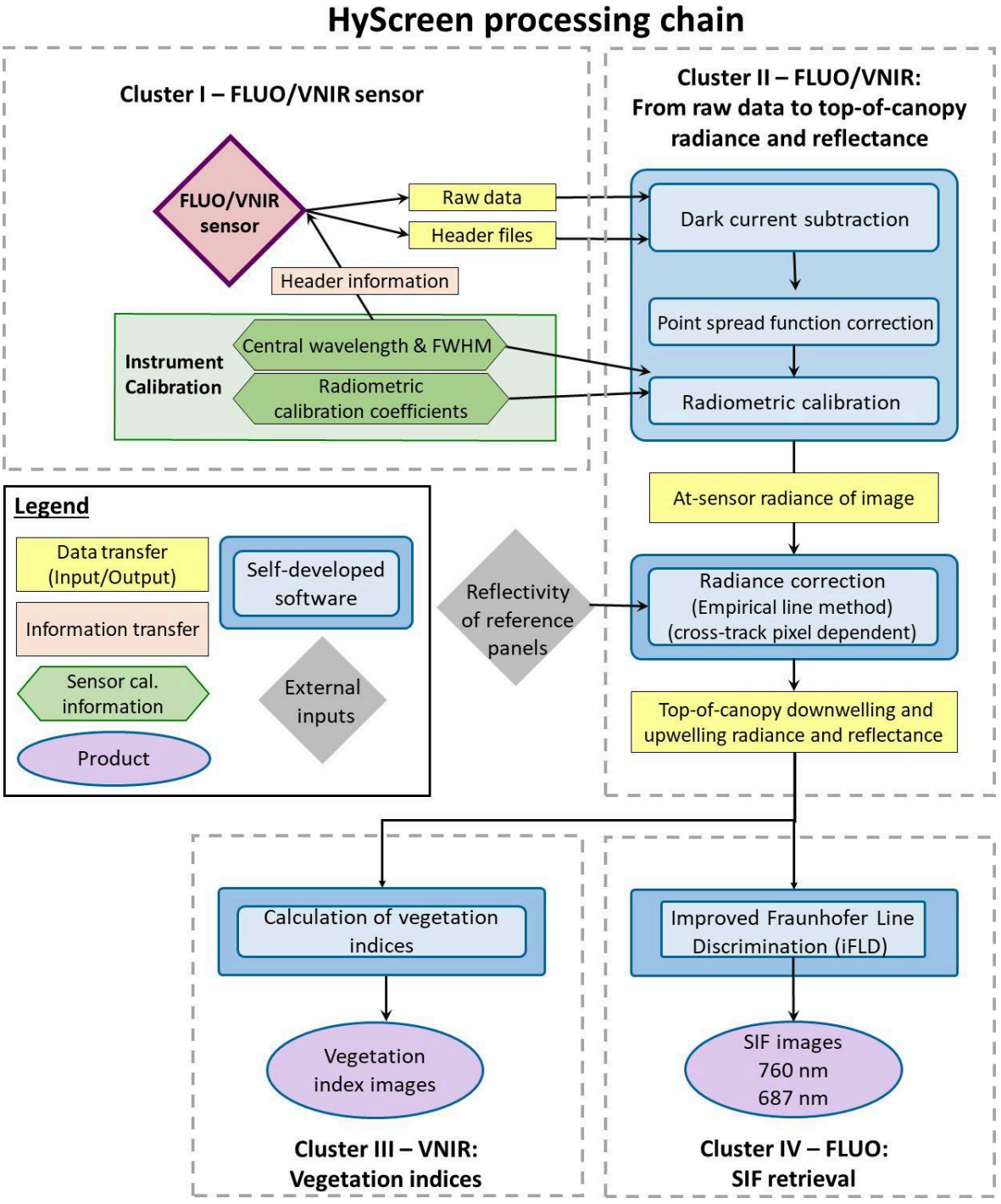

Figure 2.2 Flowchart of the HyScreen processing chain consisting of the fluorescence sensor (FLUO) and the visible and near-infrared sensor (VNIR) modules divided into four clusters: (I) raw data preparation, (II) from raw data to top-of-canopy downwelling and upwelling radiance and apparent reflectance, (III) vegetation indices and (IV) solar-induced chlorophyll fluorescence (SIF) retrieval. Spatial resolution is represented by full width at half maximum (FWHM).

2.3.1. Example scene

The example image is selected from a trial conducted at 11:03 on February 27, 2022 (UTC). The trial was performed on the lawn in front of IBG2 Plant Science of Forschungszentrum Jülich, Jülich, Germany (lat 50.9096382, long 6.4128086). During this trial, the upper four rows plants were exposed outdoors from 8:00 a.m. (3 h cold) and the lower four rows plants were brought outside just before the measurement (0 h cold). For each treatment, four genotypes with four replicates were randomized together with 4 empty pots containing only substrate. The four genotypes used in this trial were ecotype Col-0, violaxanthin de-epoxidase deficient *npq1*, PsbS protein deficient *npq4*, and blue-light photoreceptor cryptochrome 1 deficient *cry1-304*. The images were scanned by the cameras from left to right. Due to the differing FOV of FLUO and VNIR cameras, only three columns of the pots are overlapped, which reduced the replicates from the VNIR camera. To address this issue, the sensors should be mounted higher in the future trials. Meanwhile, four reference panels were used for getting the down-welling radiance, and the strip panel in the middle was necessary for the empirical line method correction of the radiance, and later for the interpolation of the down-welling radiance. The rectangular panel is also important for accounting for the variance from the spatial pixels across the track during radiance correction. Finally, the two square panels are unnecessary and even introduce artefacts such as stray light to the strip panel, so it is better to retain only the rectangular and strip panels for measurements. The Figure 2.3 below shows the false colour image from the FLUO and VNIR camera.

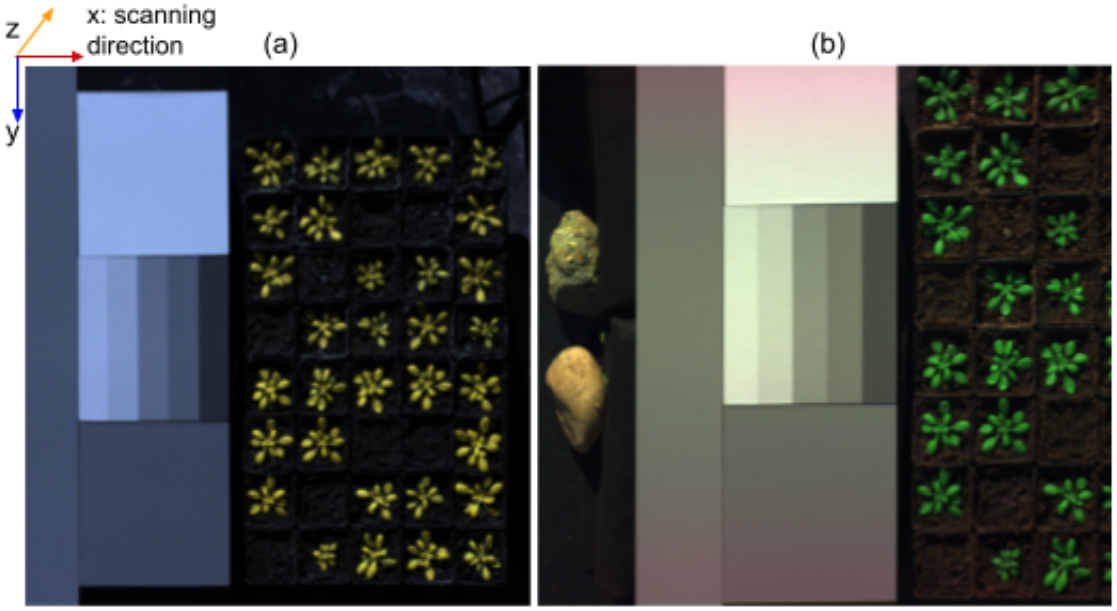

Figure 2.3 Raw data captured by FLUO and VNIR cameras at 11:03 on February 27, 2022 (UTC). (a) is the false colour image from FLUO camera, represented by the bands at 754.99 nm, 718.97 nm, and 689.52 nm. (b) is the RGB image from the VNIR camera, represented by bands at 679.27 nm, 556.97 nm, and 440.08 nm with adjustment. The scanning direction for both images was along the x axis from the left to right and the PSF correction was applied only for FLUO image spectrally (z axis) and in the direction of cross-track spatially (y axis). Due to limited length of scanning bar, the VNIR image missed the last two columns of *Arabidopsis* plants in this scene.

2.3.2. Dark current correction*

The first step is to correct the dark current (DC) in the raw images. Before each measurement, 100 frames of dark current are collected with shutter closed. These frames are averaged and subtracted from the raw digital numbers (DN) in the raw data in Equation (2.1). Figure 2.4 also presents the dark current levels for each sample and wavelength from the FLUO sensor and VNIR sensor when the integration time were set to 90 ms and 30 ms, respectively. We see the DC from FLUO is lower but also more inhomogeneous than VNIR sensor. There is pixel-by-pixel variation in both dimensions. Some wavelengths have relatively lower or higher DC than most wavelengths in both sensors. In the dimension of samples, the side pixels have obvious lower DC than the middle pixels in the FLUO sensor but not in the VNIR sensor.

$$Raw_{DN-DC} = Raw_{DN}(\lambda) - average(Raw_{DC}(\lambda)) \quad (2.1)$$

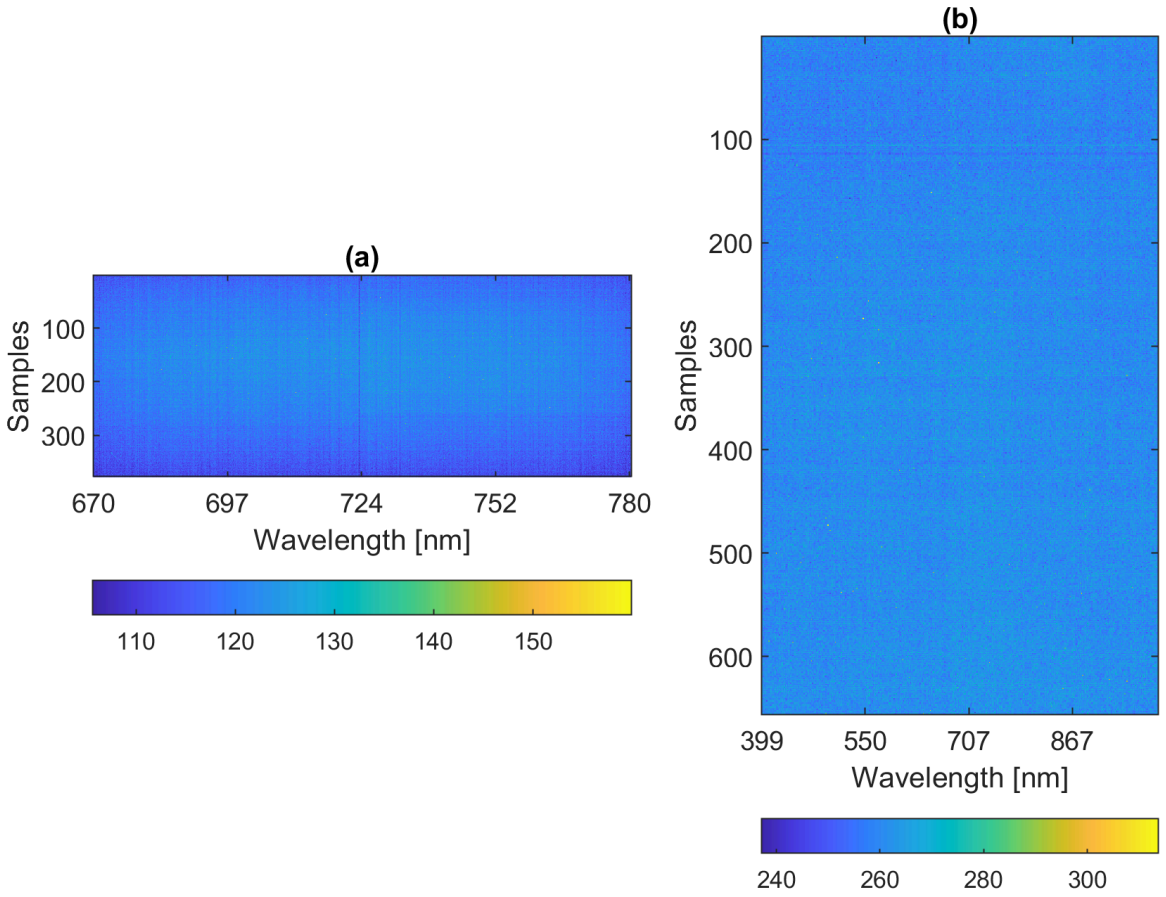

Figure 2.4 Averaged dark current in digital numbers from 100 frames from (a) the FLUO sensor with integration time of 90 ms and (b) the VNIR sensor with integration time of 30 ms.

2.3.3. Point spread function correction

Background of PSF correction

FLUO and VNIR are both push-broom spectrometers equipped with two-dimensional sensors that record spatial and spectral signals from each frame. Ideally, a given pixel in a detector is expected to measure photons of a specific frequency that hit that point exclusively. However, due to light diffraction, energy is distributed across a range, determined by the spatial PSF and the spectral instrument spectral spreadfunction (ISSF). For simplicity, both PSF and ISSF are referred to collectively as PSF in this text.

Additionally, light can be scattered by the optical and mechanical components of a instrument, creating stray light that contaminates signals on other pixels (Zong et al., 2006). In a detector matrix, pixels corresponding to specific bands and spatial positions with weaker signals are relatively prone to contamination from neighboring pixels. This is particularly relevant for SIF signals at the two oxygen absorption bands, where the downwelling radiance reaching the ground and the

corresponding reflected radiance are significantly lower than at other wavelengths (Scharr et al., 2021). Furthermore, due to the strong reflection of far-red wavelengths by vegetation, spatial pixels around plants are more susceptible to contamination from vegetation-related pixels. As a result, pixels corresponding to wavelengths having weak signals and darker objects are more vulnerable to stray signals from surrounding pixels. To improve measurement quality, it is advisable to avoid placing objects with contrasting reflectance across the track during measurements.

To address these problems, deconvolution can be exploited to reconstruct the original signal using the PSF measured in the laboratory with a monochromatic laser source Equation (2.2). Deconvolution effectively removes dispersed light but amplifies noise, requiring a tradeoff between signal accuracy and noise amplification through careful selection of the number of iterations in different algorithms.

$$I_{sensed} = I_{origin} * PSF \tag{2.2}$$

Stray light outside the spectral band range is typically reduced by applying pass filters, which allow only the expected wavelengths to pass, aiding in SIF retrieval (Grossmann et al., 2018; Rascher et al., 2009). However, stray light correction remains essential due to the faint nature of SIF signals. Several studies have focused on spectral stray light correction specifically (Albert et al., 2019, 2023). However, signals measured by detector pixels are inherently two-dimensional and should not be treated as independent components. Because SIF retrieval algorithms based on oxygen absorption bands are particularly sensitive to stray light, a 2-D stray light correction method was implemented for HyPlant. This was achieved using a single iteration of van Cittert deconvolution on the PSF, balancing the signal to noise ratio (Siegmann et al., 2019). Later improvements to stray light correction for the HyPlant FLUO module involved sharpening the PSF, which was measured by a monochromator of coarser spectral resolution than the FLUO sensor. Results showed that using the Wiener filtering algorithm improved SIF retrieval at the O_2A band but provided less satisfactory results at the O_2B band (Scharr et al., 2021).

Material and Methods

We use the iFLD method for SIF retrieval in Section 2.3.7. As Scharr et al. (2021) reported that a sharpened PSF kernel does not improve retrieval results when using iFLD algorithm, the kernel for deconvolution was not sharpened. Instead, the unsharpened Lucy-Richardson deconvolution algorithm with seven iterations was applied to deconvolve the PSF for every spatio-spectral pixel for each line. The complete process of PSF correction is illustrated in the flowchart in Figure 2.5.

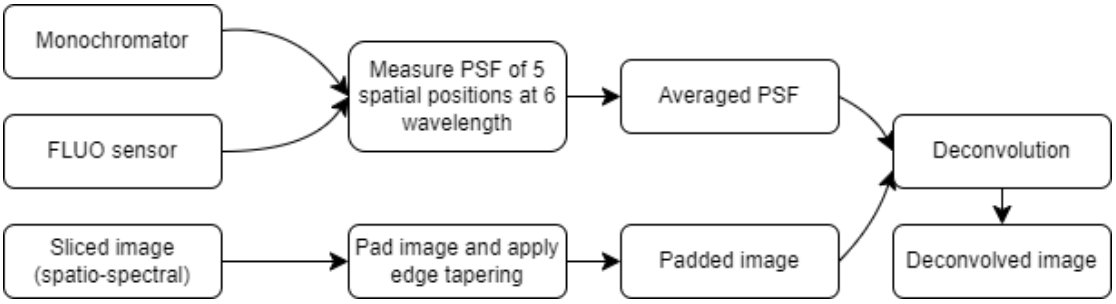

Figure 2.5 Flowchart of PSF correction including the calibration part and correction part.

To get the PSF from FLUO detector pixels, calibration data were acquired in the laboratory using a Lot-Oriel monochromator (MSH-300 (Quantum Design Europe, 2021) with a 0.14 nm bandwidth and unknown spatial PSF. Compared to the FLUO sensor's 0.06 nm spectral sampling interval, the point source is around two pixels wide in respect to the FLUO sensor, but it can still be considered as a point source after spectral binning of two of the FLUO sensor. Thirty points were measured from five spatial positions at six wavelengths, as described in Figure 2.6, with the resulting PSFs shown in Figure 2.7. The spatial and spectral PSF are observed to be quite similar, allowing them to be considered as a spatio-spectral point source for the FLUO image, which typically operates with four spatial and two spectral binning. Although the PSF differs slightly across detector locations, we assume a non-varying PSF for all spatio-spectral pixels in the FLUO detector during deconvolution due to limited measurements. The representative PSF was aggregated from the 30 measured PSFs. The peak positions of the PSFs were determined by selecting the maximum values and used to align all the PSFs, then the median was used instead of mean for aggregating a representative PSF, which can suppress potential widening of aggregated PSF caused by outliers (off-center PSFs) (Scharr et al., 2021). For the deconvolution, the Lucy-Richardson algorithm with 7 iterations is used for FLUO images without the need of providing a noise level (MathWorks Inc.).

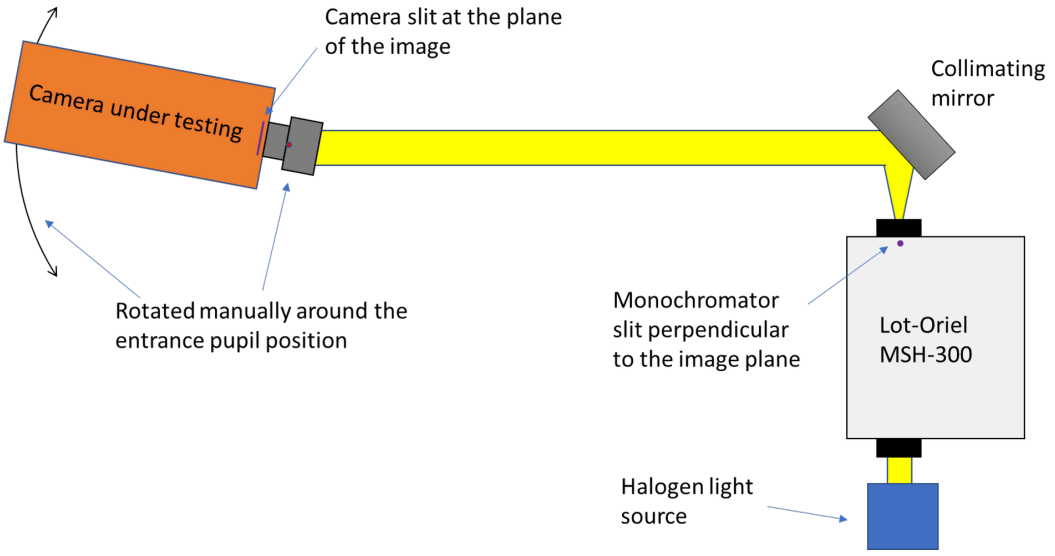

Figure 2.6 Schematics of the point spread function measurement setup of HyScreen's FLUO module using the Lot-Oriel MSH-300 monochromator. (Credit: Spectral Imaging Ltd., Oulu, Finland)

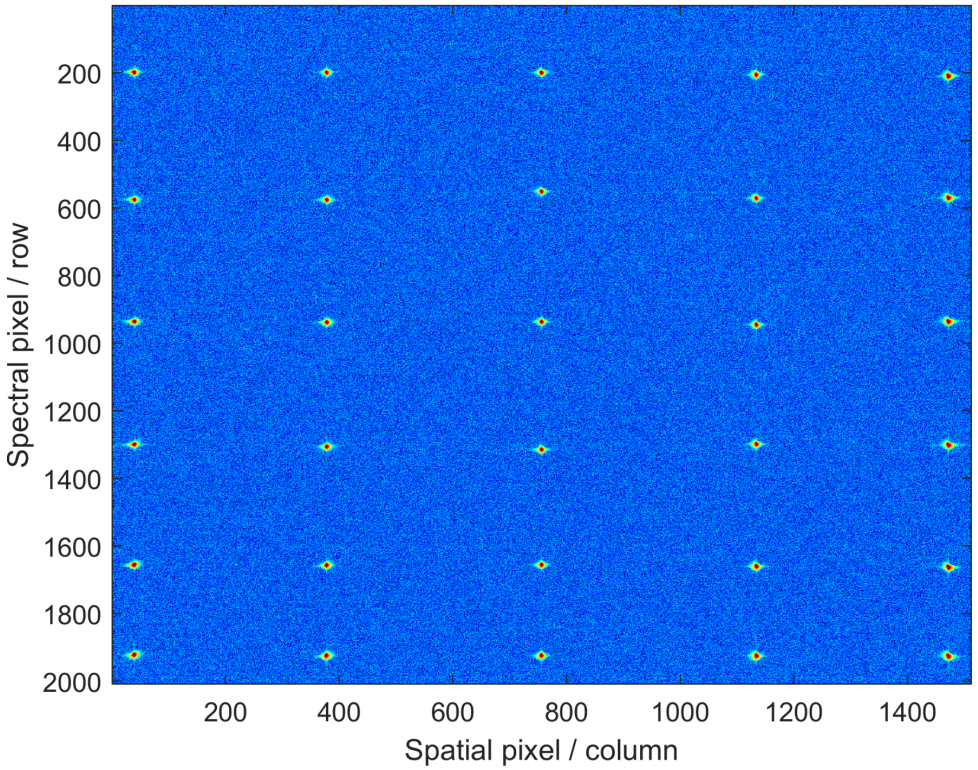

Figure 2.7 Measured PSF from 30 points from 5 spatial positions and 6 wavelengths from the FLUO sensor without binning. (Credit: Spectral Imaging Ltd., Oulu, Finland)

2.3.4. Radiometric calibration*

To convert data to at-sensor radiance in physical units, after dark current and PSF correction, the resulting digital number are normalized by integration time and

multiplied by radiometric calibration coefficients. This process is described by Equation (2.3),

$$L^{\uparrow}_{at-sensor}(\lambda) = [Raw_{DN}(\lambda) - Raw_{DC}(\lambda)] * PSF/IT \cdot coeff_{rad}(\lambda) \quad (2.3)$$

where ↑ denotes the upwelling signals, Raw_{DN} are digital numbers of the raw data cube, Raw_{DC} is the dark current, PSF is the point spread function correction described in Section 2.3.3, IT (ms) is integration time, and $coeff_{rad}$ represents the radiometric calibration coefficients presented in Figure 2.8. $L^{\uparrow}_{at-sensor}$ is the at-sensor radiance in mW m^{-2} sr^{-1} nm^{-1}, and λ indicates the corresponding wavelength. The radiometric calibration coefficients provided by the sensor manufacturer are pixel- and wavelength-dependent. Figure 2.8 shows the variation of the coefficients across wavelengths in both sensors, with a degradation from the edges to the center, especially in the FLUO sensor. The FLUO sensor also exhibits high variation of coefficients across spatial samples.

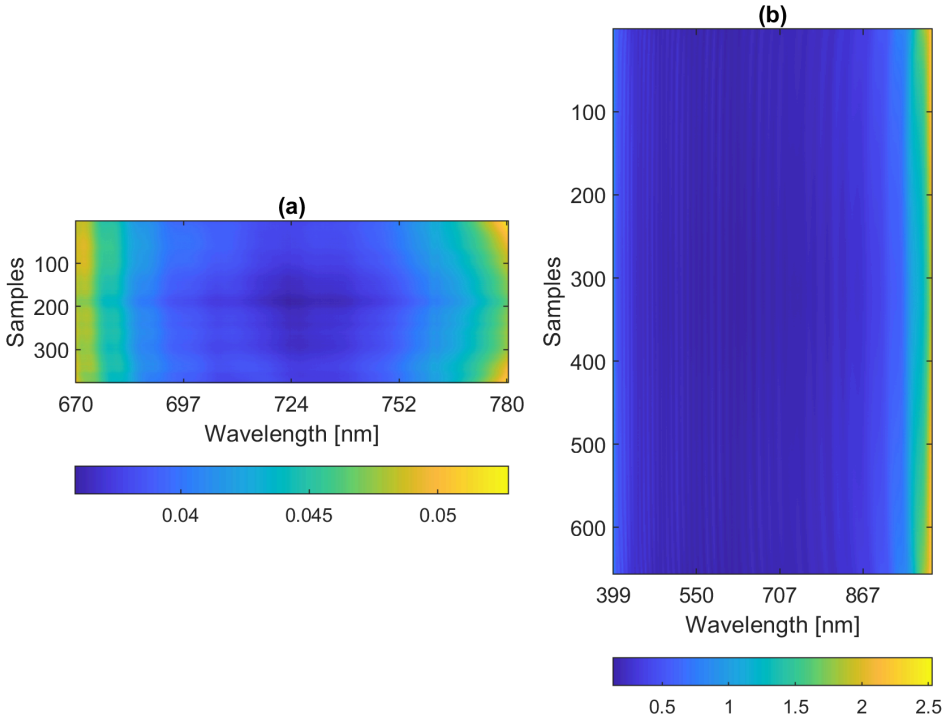

Figure 2.8 Radiometric calibration coefficients for each sample and wavelength. (a) Coefficients from the FLUO sensor when spectral binning is 4 and spatial binning is 2; (b) the Coefficients from the VNIR sensor when the spectral binning is 2 and spatial binning is 2.

2.3.5. Empirical line method correcting radiance and apparent reflectance*

The sensor radiometric and spectral calibrations, along with the optical characterization uncertainties (e.g., non-linearity and point-spread function) sa well as atmospheric scattering, introduce distortion between the at-sensor radiance and the TOC radiance. Here, we refer to this difference as "offset radiance". Darker targets and the oxygen absorption bands are more affected by this offset than brighter targets and bands outside the absorption features, as the ratio of offset-to-radiance, i.e., the SNR, is relatively higher (Arroyo-Mora et al., 2021; Sabater et al., 2018).

In this study, we apply the ELM to convert at-sensor radiance ($L^{\uparrow}_{at-sensor}$) to TOC radiance ($L^{\uparrow}_{TOC}$), which we refer to as "radiance correction". At least two reference panels with known reflectance (R) must be used to establish a linear relationship with the $L^{\uparrow}_{at-sensor}$ of HyScreen. Calibration of the reflectance of these reference panels is conducted in the laboratory by the manufacturer. Here, we show the updated ELM from two sides compared to the previous version described in Peng (2022). Firstly, we increased the amount of data for building the linear relationships between radiance and reflectance by using a strip panel with five reflectance. Secondly, a rectangular panel covering almost the whole FOV was used to correct the offset for each pixel across-track.

In the at-sensor radiance image, an ROI is selected from each strip of the strip reference panel, and an additional ROI is selected for the rectangular panel shown in Figure 2.9. The radiance of each ROI is average along lines but still remains spectral and sample dependent (i.e., across-track dependent). We use the strip panel, which has reflectance ranging from 10% to 50%, to calculate the offset ($L^{\uparrow}_{offset}$) for the sample pixels it covered. Based on the known R and the measured $L^{\uparrow}_{at-sensor}$ of the reference strips, a linear relationship can be determined for each wavelength and each sample pixel. The y-intercept indicates the offset ($L^{\uparrow}_{offset}$) caused by the various artefacts mentioned above. In this way, only a subset of sample pixels gets the $L^{\uparrow}_{offset}$ across wavelengths. To obtain the $L^{\uparrow}_{offset}$ for additional samples across of the FOV, we calculate the ratio between the radiance of the rectangular panel and the $L^{\uparrow}_{offset}$ from the pixels covered by the strip panel. Then, the $L^{\uparrow}_{offset}$ for the sample pixels covered by the rectangular panel is determined by dividing their radiance by the averaged ratio. These offsets are then subtracted from $L^{\uparrow}_{at-sensor}$ to obtain $L^{\uparrow}_{TOC}$, thereby forcing the fitted line to

pass through the origin. TOC downwelling radiance ($L^{\downarrow}_{TOC}$) is defined as the $L^{\uparrow}_{TOC}$ when the reflectance equals one. For VNIR sensor, the $L^{\uparrow}_{at-sensor}$ is still used to calculate vegetation indices which are not sensitive to offset radiance.

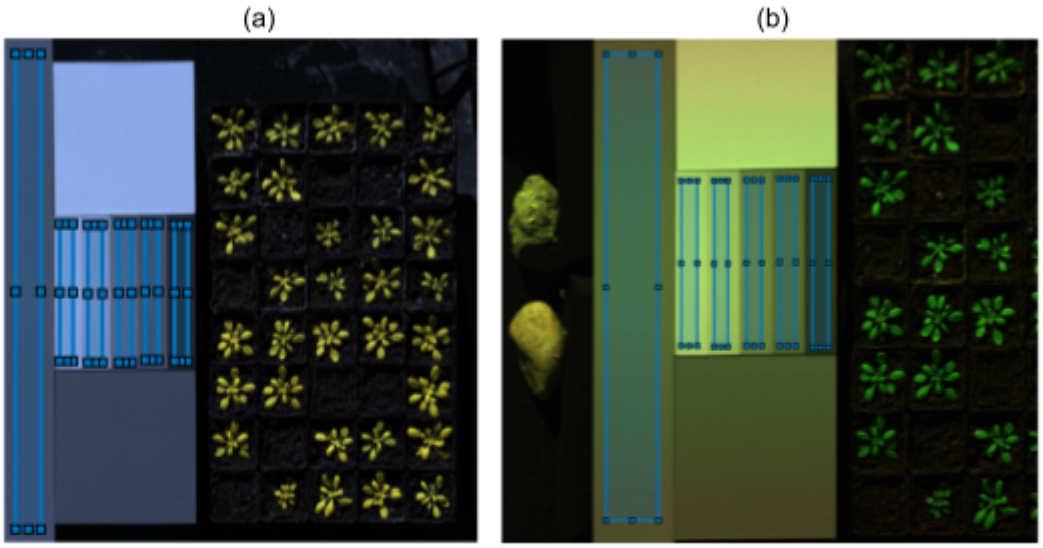

Figure 2.9 Demonstration of empirical line method for radiance correction using one rectangular panel and one strip panel. The reflectance of the rectangular panel is approximately 20%, and the strip panel consists of four sections with reflectance values of approximately 50%, 43%, 30%, 20%, and 10% from left to right. (a) regions of interest from the FLUO sensor, and the false colour image is represented by the bands at 754.99 nm, 718.97 nm, and 689.52 nm. (b) regions of interest from the VNIR sensor, and the RGB image is represented by bands at 679.27 nm, 556.97 nm, and 440.08 nm.

The $L^{\uparrow}_{TOC}$ represents the sum of the actual reflected radiance from vegetation and the emitted radiance of fluorescence. Therefore, the reflectance calculated using Equation (2.4) is termed apparent reflectance (R_{app}) because it represents a combination of the actual reflectance and the fluorescence contribution, expressed as the ratio of fluorescence to $L^{\downarrow}_{TOC}$.

$$R_{app}(\lambda) = L^{\uparrow}_{TOC}(\lambda)/L^{\downarrow}_{TOC}(\lambda) \quad (2.4)$$

Due to the low downwelling radiance in the oxygen absorption features, the ratio of offsets to downwelling radiance within the O_2A and O_2B bands are distinctly larger than those in the bands on the shoulders of both absorption features. Consequently, offsets within the absorption bands lead to infilling features similar to SIF. Thus, given the current optical characterization of the system, the ELM correction to the offset radiance is significant for SIF retrieval.

2.3.6. Solar-Induced chlorophyll fluorescence retrieval*

Due to the high spectral resolution of the HyScreen FLUO module, fluorescence emitted at both 760 nm and 687 nm can be successfully retrieved. In this workflow, the iFLD method (Alonso et al., 2008) was implemented to retrieve SIF from the HyScreen FLUO module. Detailed descriptions are provided by Cendrero-mateo (2019). Table 2.2 summarizes how the iFLD was implemented in the HyScreen processing chain.

Table 2.2. Description of the parameters, wavelength ranges, wavelength intervals (WI) and interpolation/model functions for the iFLD method used in this processing chain. Downwelling radiance ($L^{\downarrow}$), reflectance (R), fluorescence (F), absorption feature (Abs. feature) are presented in the table.

Band	$L^{\downarrow}$ **and** R **Interpolation WI**	**Abs. Feature WI**	**Interpolation Method**
O_2A	750–780 nm	759.3–768.0 nm	$L^{\downarrow}$: polynomial 2nd grade R: linear smoothing spline
O_2B	665–716 nm	683.3–696.9 nm	$L^{\downarrow}$: polynomial 2nd grade R: linear smoothing spline

Here shows the final results of SIF from FLUO sensor. Moreover, the importance of PSF correction for SIF retrieval shown in Figure 2.10 by comparing the SIF images without and with PSF correction. Figure 2.11 shows the SIF results from the vegetation parts only, which is more clear without background.

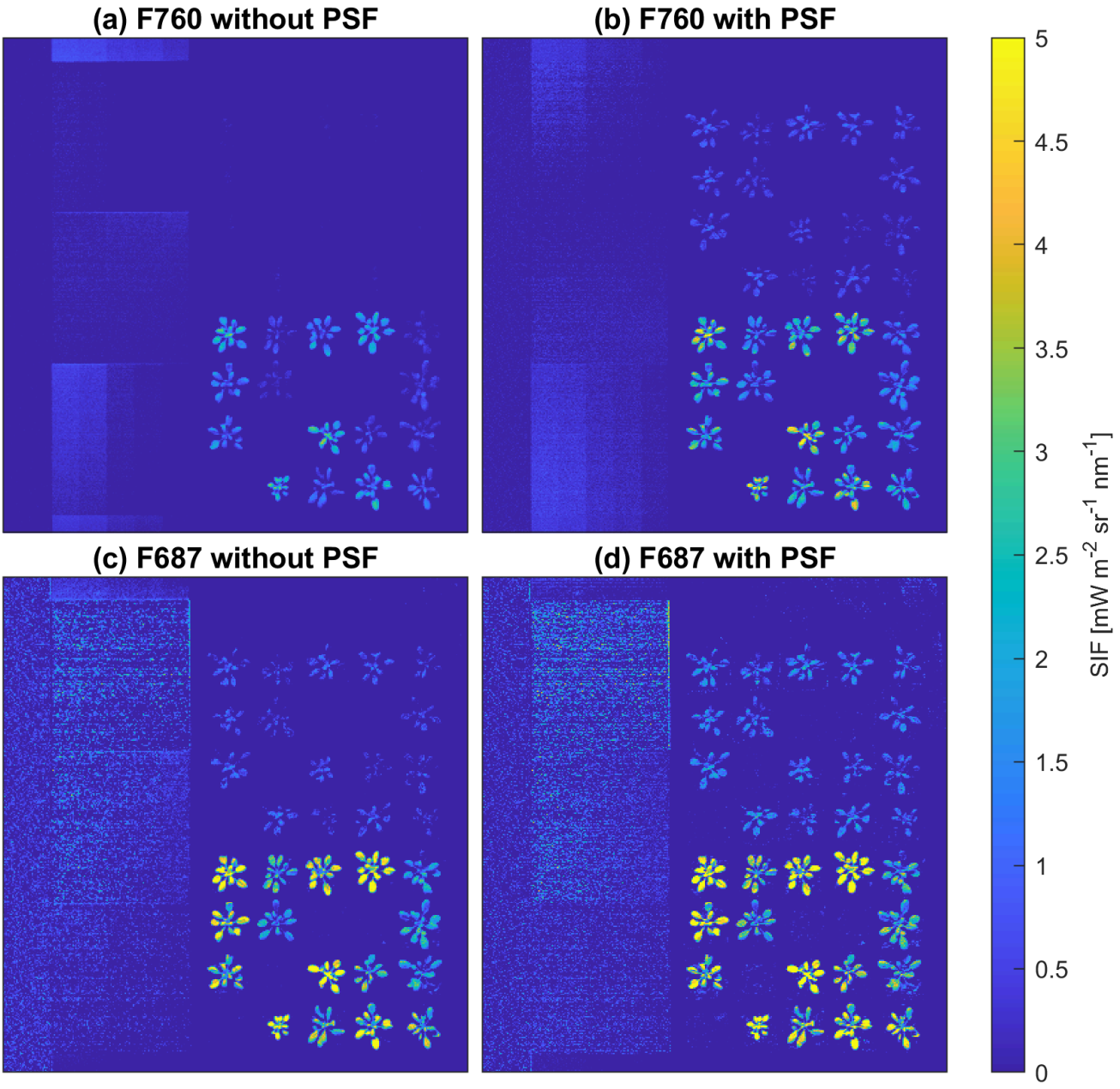

Figure 2.10 SIF results with and without point spread function correction. (a) and (b) are SIF at 760 nm; (c) and (d) are SIF at 687 nm. This example was selected from a trial, and plants from the upper four rows were exposed to 3 h cold (exposed treatment) and the lower four rows plants were 2 minutes cold (instant treatment). For each treatment, four genotypes with four replicates were randomized together with 4 empty pots containing only substrate.

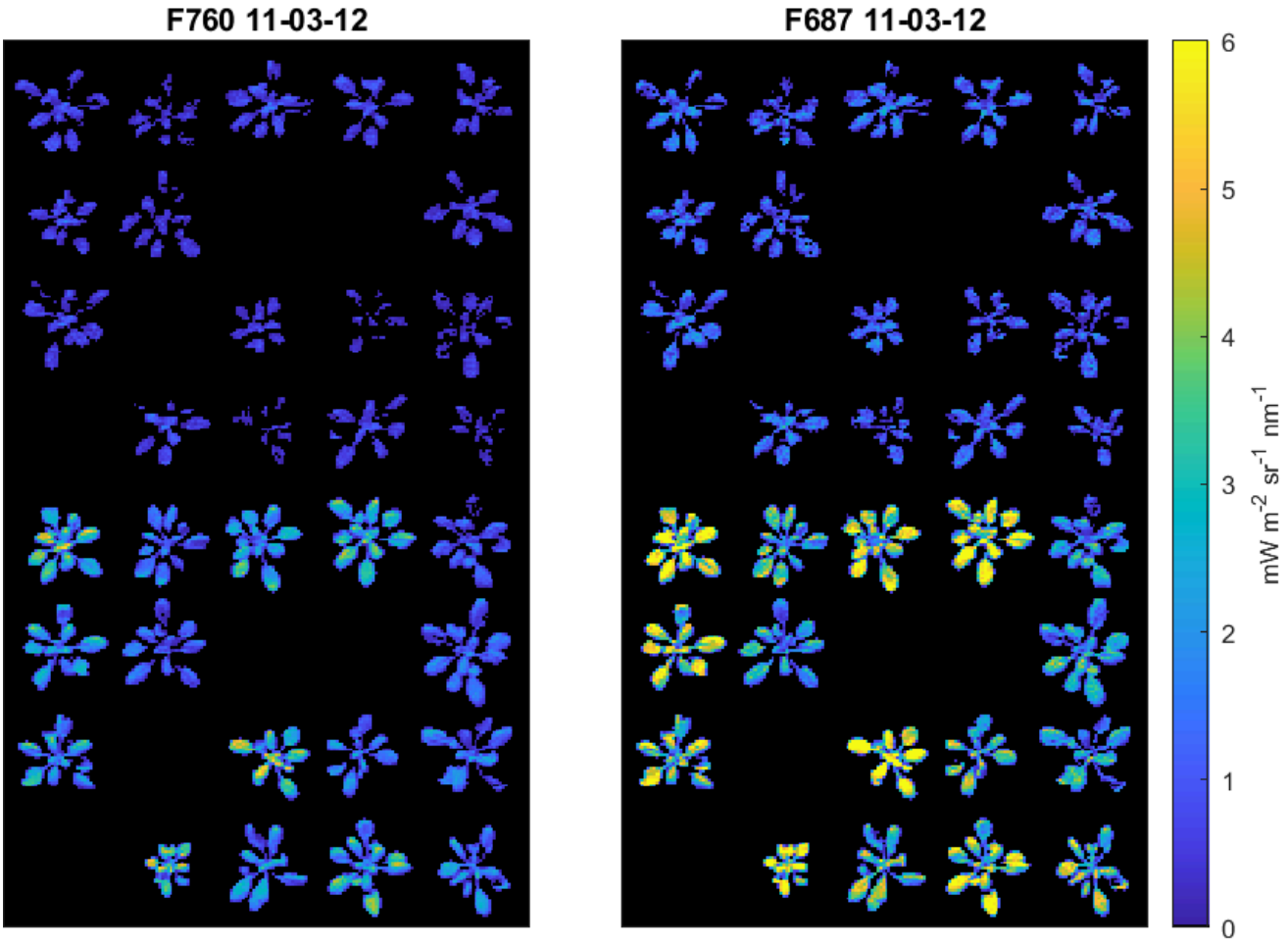

Figure 2.11 SIF results from vegetation parts and values below zero were excluded. The left is SIF at 760 nm and the right is SIF at 687 nm. This example was selected from a trial, and plants from the upper four rows were exposed to 3 h cold (exposed treatment) and the lower four rows plants were 2 minutes cold (instant treatment). For each treatment, four genotypes with four replicates were randomized together with 4 empty pots containing only substrate.

2.3.7. Vegetation indices*

Vegetation indices (VIs) were calculated from TOC reflectance image data without correcting the radiance offset, in order to reduce potential noise. Due to the limited spectral range of the FLUO sensor, only eight relevant VIs, listed in Table 2.3, were extracted and are shown in Figure 2.12. For the VNIR data, 15 VIs were extracted, as listed in Table 2.4 and presented in Figure 2.13. The VIs include wavelengths from the green, red, red-edge, NIR regions, capturing information related to pigment contents such as chlorophylls, Carotenoids, and anthocyanins, as well as leaf structure characteristics and water content. The normalized difference vegetation index (NDVI) and simple ratio (SR) were calculated from red and NIR bands due to their sensitivity to chlorophyll, which strongly absorbs red light, and to the spongy mesophyll structure of leaves, which reflects NIR light

strongly. Higher NDVI and SR values indicate healthier green leaves (Asrar et al., 1984; Rouse et al., 1973). The NIR reflectance of vegetation (NIRv) and NIR radiance of vegetation (NIRvR) are indices derived from NDVI and reflectance or radiance in the NIR bands. These indices were calculated to help extract fluorescence yield by mitigating the effects of canopy structure and sun-sensor geometry on SIF (Zeng et al., 2022b, 2019). The red-edge normalized difference vegetation index (NDVIre) and the chlorophyll index red-edge (CIre) are correlated to leaf chlorophyll content and plant stress, taking advantage of the high sensitivity of red-edge reflectance to chlorophyll levels(Gitelson and Merzlyak, 1994; Gitelson et al., 2003).

While the VIs above can be derived from both FLUO and VNIR data, information from shorter wavelengths and longer NIR wavelengths is missing, particularly signals associated with carotenoids and anthocyanins, which are important indicators of plant stress response. The photochemical reflectance index (PRI), an indicator of the state of the xanthophyll cycle, is inversely correlated with NPQ (Gamon et al., 1992). The chlorophyll/carotenoid index (CCI) can track changes in pigment levels and indicate photosynthetic activity (Gamon et al., 2016). The modified carotenoid reflectance index (mCRIgreen) and the modified anthocyanin reflectance index (mARI) are correlated with the contents of carotenoids and anthocyanins, respectively (Gitelson et al., 2006). The water band index (WBI) is inversely correlated with water content, serving as an indicator of plant stress levels (Peñuelas et al., 1994). Fluorescence correction vegetation index (FCVI) is used to disentangle photosynthetic and physical effects on far-red SIF by accounting for PAR absorption and scattering effects (Yang et al., 2020). With these VIs, it is possible not only to extract biophysical and biochemical parameters from spectra, but also to consider radiative transfer processes between the sun, the object, and the sensor, thereby facilitating our investigations into photosynthetic activities in plants.

Table 2.3 The vegetation indices calculated from TOC reflectance data recorded by FLUO sensor on HyScreen. The spectral sampling interval of FLUO sensor is around 0.11 nm after the twofold binning applied during measurements. R represents the averaged reflectance over central wavelength ± 4 bands (indicated as ±4, corresponding to approximately 1 nm in total). These VIs are derived from red, red-edge, and near-infrared wavelengths, providing information about chlorophyll content and leaf structural characteristics.

Index	**Equation**	Reference
$^{*}NDVI_{FLUO}$	$(R_{775\pm4} - R_{675\pm4})/(R_{775\pm4} + R_{675\pm4})$	(Rouse et al., 1973)
$NIRv_{red}$	$NDVI{\cdot}R_{675\pm4}$	(Zeng et al., 2019)

$NIRvR_{red}$	$NDVI{\cdot}Rad_{675\pm4}$	(Zeng et al., 2019)
$NIRv_{farred}$	$NDVI{\cdot}R_{775\pm4}$	(Zeng et al., 2019)
$NIRvR_{farred}$	$NDVI{\cdot}Rad_{775\pm4}$	(Zeng et al., 2022b)
SR	$R_{775\pm4}/R_{675\pm4}$	(Asrar et al., 1984)
$NDVI_{re}$	$(R_{742\pm4}-R_{702\pm4})/(R_{742\pm4}+R_{702\pm4})$	(Gitelson and Merzlyak, 1994)
CI_{re}	$R_{790\pm2}/R_{700\pm2}-1$	(Gitelson et al., 2003)

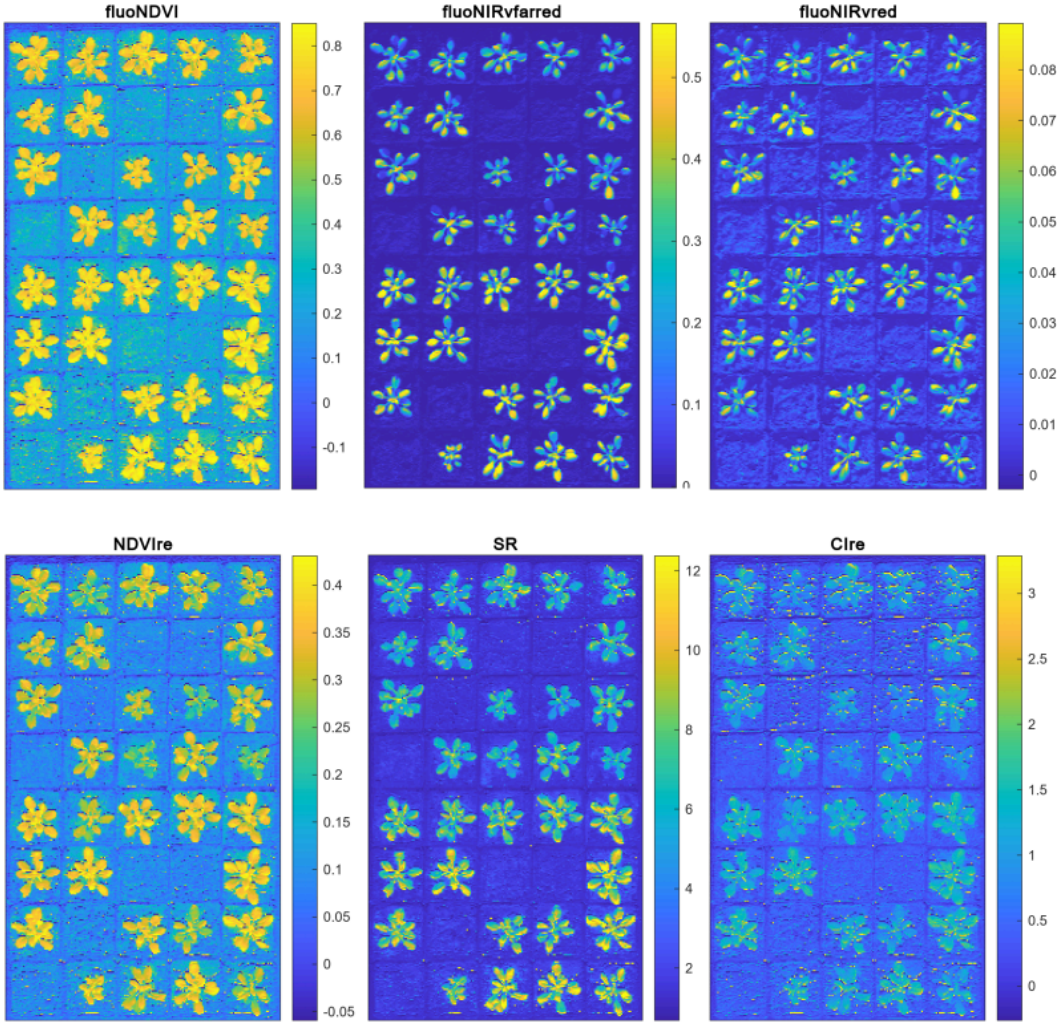

Figure 2.12 Demonstration of Vegetation indices (VIs) calculated from FLUO data. Only the plates were retained for a clearer demonstration of VIs from plants. The equations used to calculate these VIs are provided in Table 2.3. This example was selected from

a trial, and plants from the upper four rows were exposed to 3 h cold (exposed treatment) and the lower four rows plants were 2 minutes cold (instant treatment). For each treatment, four genotypes with four replicates were randomized together with 4 empty pots containing only substrate.

Table 2.4 The vegetation indices calculated from TOC reflectance data recorded by VNIR sensor on HyScreen. The spectral sampling interval of the VNIR sensor is approximately 1.5 nm after the twofold binning applied during measurements. R represents the averaged reflectance over the central wavelength ± several bands (indicated as ±). These VIs are derived from green, red, red-edge, and near-infrared wavelengths, providing information on carotenoid content, chlorophyll content, anthocyanin content, water content and leaf structural characteristics.

Index	**Equation**	Reference
$NDVI_{VNIR}$	$(R_{802\pm4} - R_{672\pm4})/(R_{802\pm4} + R_{672\pm4})$	(Rouse et al., 1973)
$NIRv_{red}$	$NDVI{\cdot}R_{672\pm4}$	(Zeng et al., 2019)
$NIRvR_{red}$	$NDVI{\cdot}Rad_{672\pm4}$	(Zeng et al., 2022a)
$NIRv_{farred}$	$NDVI{\cdot}R_{802\pm4}$	(Zeng et al., 2019)
$NIRvR_{farred}$	$NDVI{\cdot}Rad_{802\pm4}$	(Zeng et al., 2022a)
$NDVI_{FLUO}$	$(R_{775} - R_{675})/(R_{775} + R_{675})$	(Rouse et al., 1973)
SR	$R_{802\pm4}/R_{672\pm4}$	(Asrar et al., 1984)
$NDVIre$	$(R_{742\pm4} - R_{702\pm4})/(R_{742\pm4} + R_{702\pm4})$	(Gitelson and Merzlyak, 1994)
$FCVI$	$R_{770\pm4} - R_{550\pm95}$	(Yang et al., 2020)
$CIre$	$R_{790\pm2}/R_{700\pm2} - 1$	(Gitelson et al., 2003)
$mCRIgreen$	$(1/R_{515\pm2} - 1/R_{565\pm2}) * R_{790\pm2}$	(Gitelson et al., 2006)
PRI	$(R_{531} - R_{570})/(R_{531} + R_{570})$	(Gamon et al., 1992)

CCI	$(R_{531} - R_{645})/(R_{531} + R_{645})$	(Gamon et al., 2016)
$mARI$	$(1/R_{550\pm2} - 1/R_{700\pm2}) * R_{790\pm2}$	(Gitelson et al., 2006)
WBI	$(R_{962\pm4} - R_{897\pm4})/(R_{962\pm4} + R_{897\pm4})$	(Peñuelas et al., 1994)

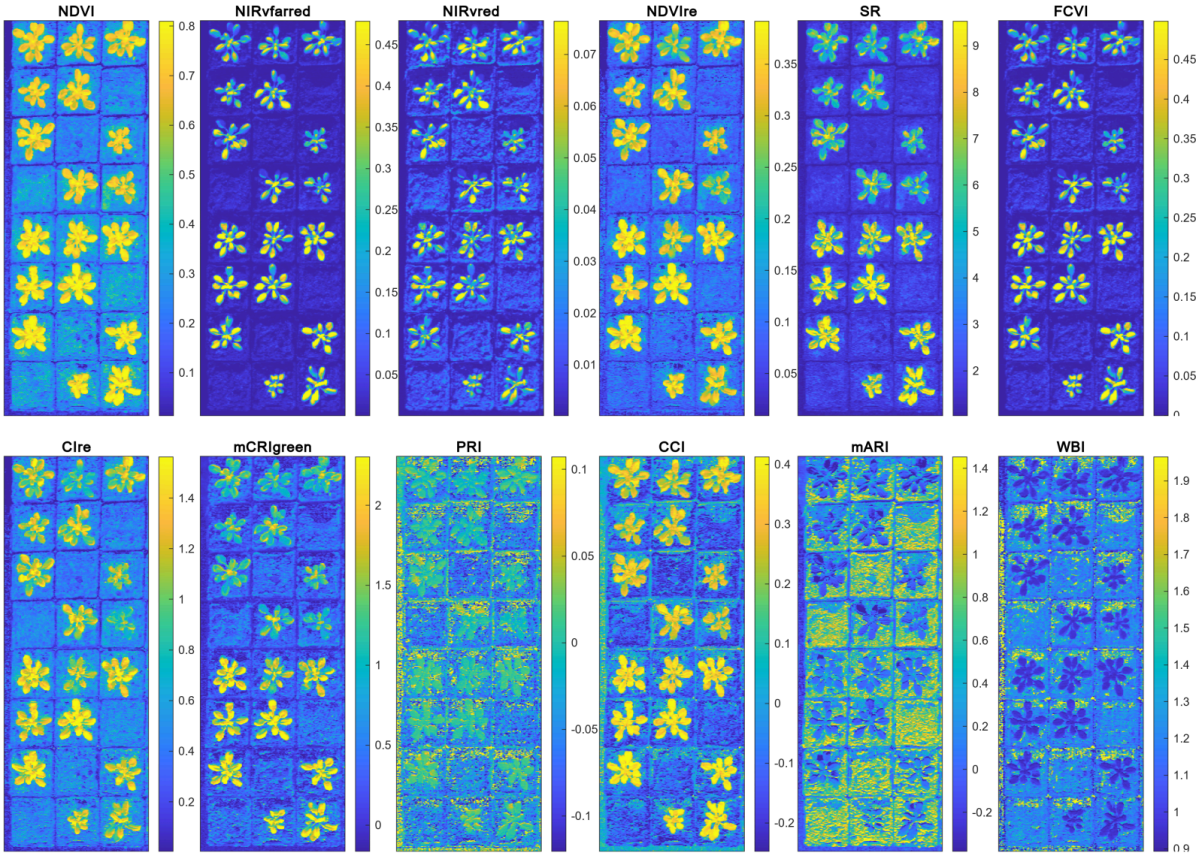

Figure 2.13 Demonstration of Vegetation indices (VIs) calculated from VNIR data. Only the plates were retained to provide a clearer demonstration of VIs from plants. The equations used to calculate these VIs are listed in Table 2.4.

2.4. SNR and NER*

To determine the SNR and the corresponding noise-equivalent-radiance (NER) of HyScreen's FLUO module, images of Lambertian reference panels with different reflectance values were recorded. Four panels were used: one rectangular panel with a reflectance of 20% and size of 0.8 × 0.2 m; two square panels with reflectances of 50% and 20%, each with size of 0.2 × 0.2 m; and one strip panel with size of 0.2 × 0.2 m, consisting of five strips with reflectance values of 50%,

43%, 30%, 20%, and 10%. ROIs were defined shown in Figure 2.14 to calculate SNR and NER. Since SNR and NER are slightly influenced by the across-track pixel position, the final values were computed as the mean of the across-track samples.

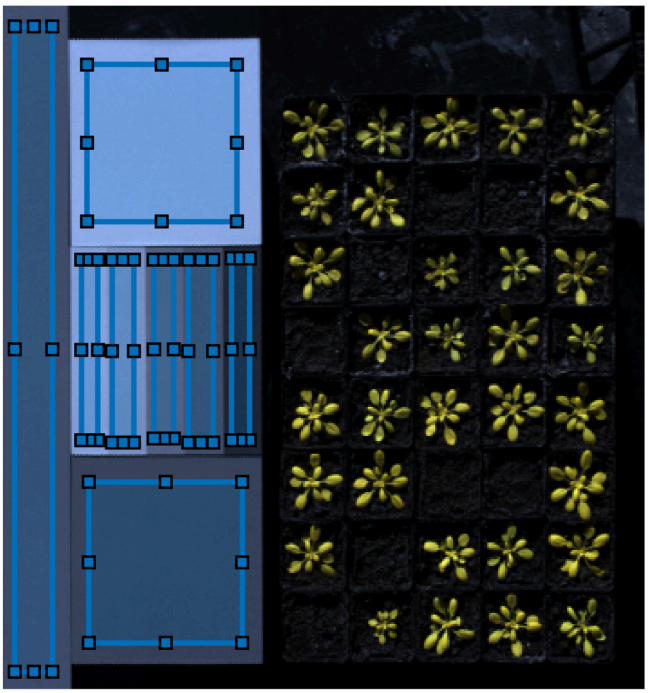

Figure 2.14 Demonstration of regions of interest (ROI) from both FLUO sensor for signal-to-noise ratio (SNR) and noise-equivalent-radiance (NER) calculations. One rectangular panel, two square panels, and one strip panel were used. From left to right and from top to down, the reflectance of the rectangular panel is approximately 20%, the first square panel has a reflectance of 50%, the strip panel consists of five sections with reflectance values of approximately 50%, 43%, 30%, 20%, and 10% from left to right, and the final square panel has a reflectance of 20%.

2.4.1. SNR and NER calculation*

As SNR is crucial for assessing the sensor's suitability for retrieving SIF, in this section, we present the methods used to estimate SNR and NER. For a specific ROI, according to (Schaepman and Dangel, 2000), SNR is calculated for each wavelength using Equation (2.5).

$$SNR(\lambda) = S(\lambda)/N(\lambda) = mean(Raw_{ROI}(\lambda))/std(Raw_{ROI}(\lambda)) \quad (2.5)$$

$$= [mean(Raw_{DN}(\lambda)) - mean(Raw_{DC}(\lambda))]/[std^2(Raw_{DN}(\lambda)) + std^2(Raw_{DC}(\lambda))]^{1/2}$$

Here S and N represent signal and noise, respectively, while $mean(Raw_{ROI})$ and $std(Raw_{ROI})$ denote the mean and standard deviation of the pixel values covered by the ROI. The mean value is computed from the raw data (Raw_{DN}) after

subtracting the dark current (Raw_{DC}). The noise corresponds to the standard deviation of the signal and is determined as the square root of the sum of variances of the raw data ($std^2(Raw_{DN})$) and dark-current ($std^2(Raw_{DC})$). When calculating NER, the SNR is set to 1 (i.e., the signal equals the noise). Thus the noise-equivalent signal (NES) can be computed using Equation (2.6).

$$NES(\lambda) = [std^2(Raw_{DN}(\lambda)) + std^2(Raw_{DC}(\lambda))]^{1/2} \quad (2.6)$$

Finally, the NER is determined by multiplying the NES by the radiometric calibration coefficients and normalising by integration time (IT), as shown in Equation (2.7).

$$NER(\lambda) = NES(\lambda)/IT * coeff_{rad}(\lambda) \quad (2.7)$$

2.4.2. Results of SNR and NER of reference panels

The SNR and NER results for each reference panel are shown in Figure 2.15. We can observe that both SNR and NER increase with increasing reflectance of the panels in Figure 2.14. For the two square panels with reflectance of 20% and 50%, their SNR appears lower than those of the strip and rectangular panels with the same reflectance. This may be due to larger area cross scanning lines covered by the square panels, thus we focus on the quantitative results from the remaining panels. For wavelengths outside of oxygen absorption bands, the SNR for the 10%, 20%, 30%, 43%, and 50% reference panels are around 60, 80-90, 95, 110 and 130, respectively. The corresponding NER are around 0.04, 0.06, 0.07, 0.09, and 0.09 $mW \cdot m^{-2} \cdot sr^{-1} \cdot nm^{-1}$ (Figure 2.15). Since downwelling radiance within the O_2 absorption bands is significantly lower than in the rest of the spectral range, the SNR and NER of each reference panel at O_2A and O_2B are distinctly reduced (Figure 2.15).

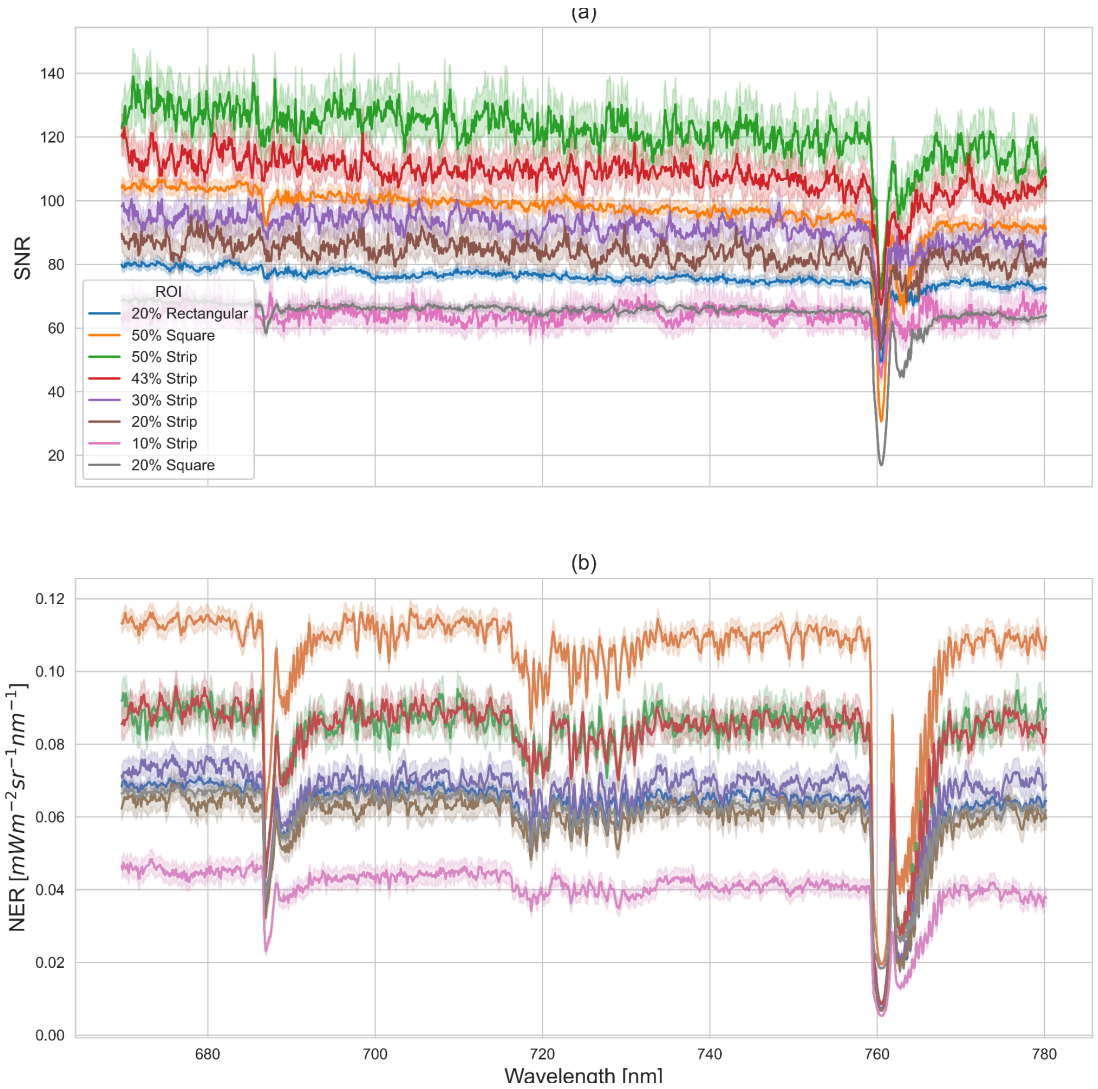

Figure 2.15 Wavelength and sample dependent signal-to-noise ratio (SNR) and corresponding noise-equivalent-radiance (NER) from four reference panels measured by HyScreen's FLUO module.

The SNR and NER of reference panels at 760.04 nm and 687.04 nm are listed in Table 2.5 SNR at 760.04 nm are lower than those at 687.04 nm due to stronger absorption of downwelling radiance in the O_2A band compared to the O_2B band. The NER at 760.04 nm are fairly consistent around 0.01 $mW \cdot m^{-2} \cdot sr^{-1} \cdot nm^{-1}$ except for the two square panels. This indicates that darker panels show relatively higher noise than brighter panels, which may lead to increased uncertainty in the SIF retrieval for dark objects.

Table 2.5. The signal-to-noise ratio (SNR) and corresponding noise-equivalent-radiance (NER) of reference panels at O_2A (760) nm and O_2B (687) nm absorption bands, measured by HyScreen's FLUO sensor.

Wavelength	O_2B @ 687.04 nm		O_2A @ 760.04 nm	
Reference Panel	SNR	NER	SNR	NER
20% Rectangular	75.4	0.04	59.01	0.01
50% Square	92.18	0.06	49.72	0.02
20% Square	58.6	0.04	26.23	0.02
50% Strip	122.43	0.05	89.17	0.01
43% Strip	109.14	0.05	83.78	0.01
30% Strip	88.31	0.04	68.82	0.01
20% Strip	80.95	0.04	65.73	0.01
10% Strip	63.88	0.02	54.39	0.01

Figure 2.16 and Figure 2.17 show the sample-dependent SNR and NER from the reference panels at 760.04 nm and 687.04 nm. Notable fluctuations are observed across the samples, particularly for the strip panel. However, according to the 20% reflectance rectangular panel, which covered the entire FOV, the variations in SNR and NER remain within a consistent range. Additionally, the SNR and NER at 760.04 nm vary more than those at 687.04 nm.

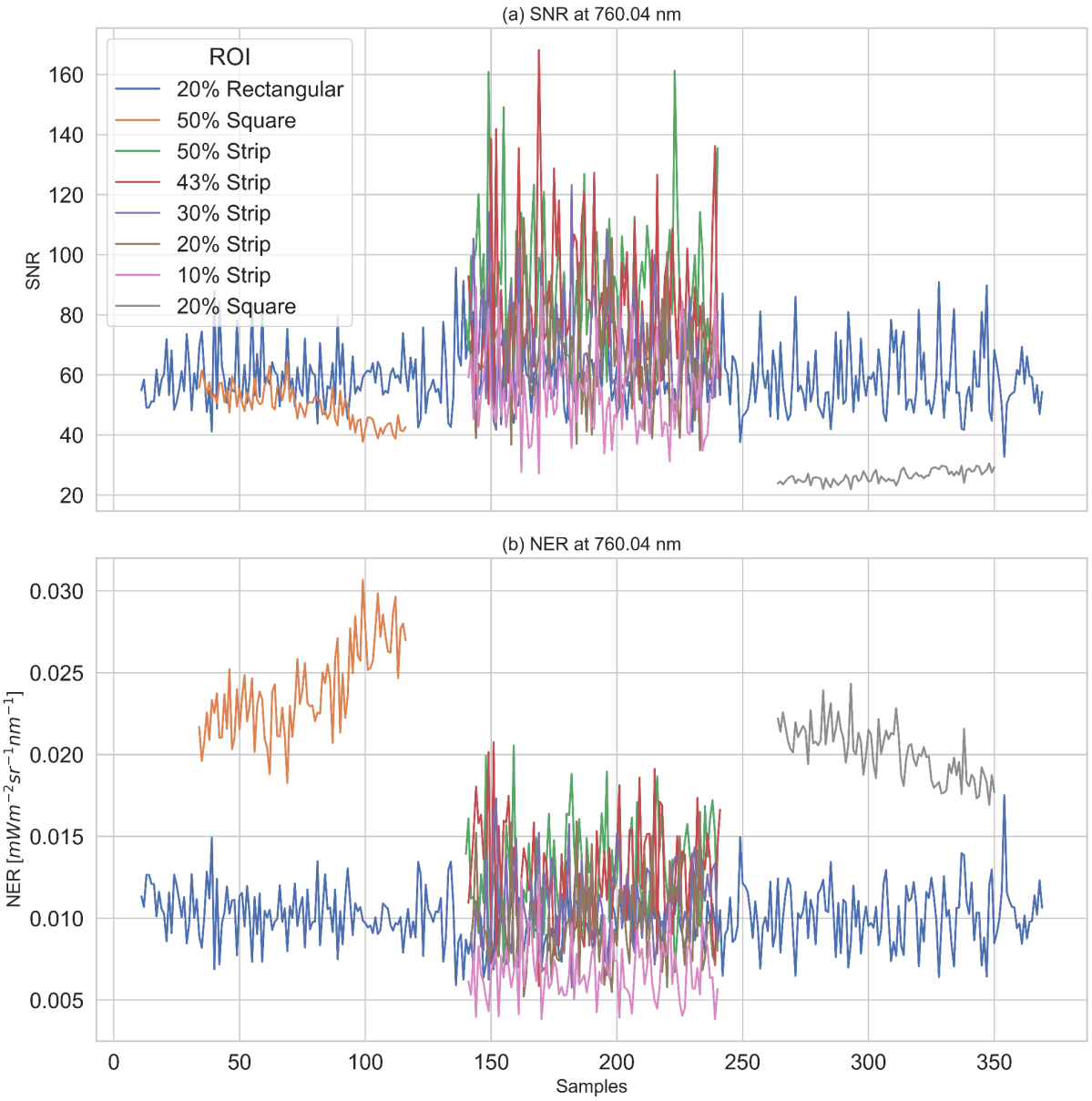

Figure 2.16 The sample-dependent signal-to-noise ratio (SNR) and corresponding noise-equivalent-radiance (NER) at the O_2A band (760.04 nm) from four reference panels measured by HyScreen's FLUO sensor.

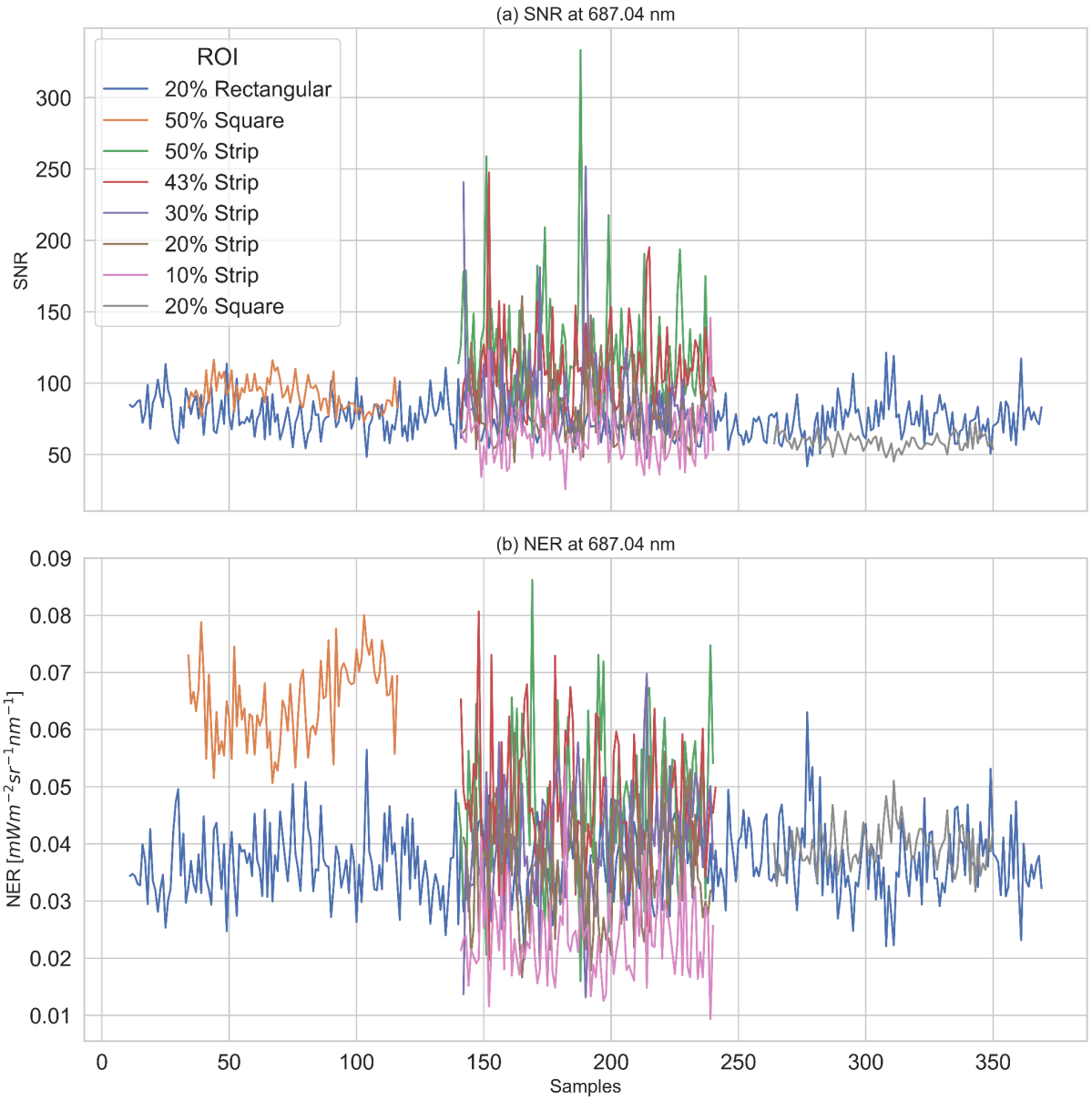

Figure 2.17 The sample-dependent signal-to-noise ratio (SNR) and corresponding noise-equivalent-radiance (NER) at the O_2B band (687.04 nm) from four reference panels measured by HyScreen's FLUO sensor.

3. Energy partitioning in PSII of *Arabidopsis* under cold stress

3.1. Materials and methods

SIF is regarded as a proxy for quantifying the dynamics of photosynthetic efficiency remotely; however, the spatio-temporal mechanisms underlying their relationship are not fully clear. To better understand these mechanisms, additional parameters are required, such as NPQ capacity and responses of chlorophyll fluorescence under varying environmental conditions. In this study, cold stress was deployed on *Arabidopsis* plants with differing NPQ capacity to demonstrate how NPQ pathways, photoinhibition, leaf pigments, and leaf age affect the dynamics of SIF across space and time.

3.1.1. Plant materials and growth conditions

Four genotypes of *Arabidopsis thaliana* Columbia (Col) accessions were used in the cold stress experiment, summarized in Table 3.1. Col-0 is ecotype as control, *npq1* is violaxanthin de-epoxidase (VDE)-deficient, *npq4* is PsbS deficient, and *cry1-304* lacks the blue-light photoreceptor cryptochrome 1. The *npq1* mutant has a lesion in the enzyme violaxanthin de-epoxidase, which converts carotenoid violaxanthin to zeaxanthin in the chloroplast xanthophyll cycle. Zeaxanthin not only protects photosynthetic pigments from excess excitation energy but also mediates blue light-stimulated stomatal opening via its role as a blue-light photoreceptor in guard cells. The conversion of violaxanthin to zeaxanthin depends on the pH of the thylakoid lumen (Taiz et al., 2015). The *npq4* mutant characterized by deficient PsbS protein showed no conformational change in the LHC complex, thus lacking the rapid induction of NPQ (Peterson and Havir, 2001). The *cry1-304* stimulates less chloroplast transcription than Col-0 which slows down the recovery of the PSII reaction centre under stress conditions (Mockler et al., 1999).

Table 3.1 Summary of *Arabidopsis thaliana* genotypes used in this experiment. qE represents pH-dependent NPQ, while qZ represents pH-independent NPQ.

Genotypes	Abbreviation	Properties	qE	qZ
Col-0	0	Wild type	normal	normal
npq1	1	violaxanthin de-epoxidase (VDE) enzyme deficient	less	absent
npq4	4	PsbS protein deficient in LHCII	absent	normal
cry1-304	c	cryptochrome deficient	normal	normal

The seeds were sown on January 25, 2022, in a tray of 30 cm by 50 cm with 576 plugs. The substrate for germination was Einheitserde Typ Pikier (Einheitserde Werkverband e.V.). After sowing and watering, the tray was moved into a cooling room for three days to mimic the vernalization process. Germination took place in a climate chamber set to 20℃ with a day length of 18 h. When the fourth leaf appeared on February 14, 2022, 16 plants of each genotype were transplanted to 7*7 cm pots containing Dachstaudensubstrat soil (Hawita, Vechta, Germany) and transferred to a glasshouse for further growth. Each treatment consisted of four replicates for each genotype, along with four pots containing soil only.

3.1.2. Experimental design

The experiments were conducted over two consecutive days. Figure 3.1 shows the experimental design. On the first day, SIF and VI were measured outdoors throughout the day using HyScreen, and Φ_{PSII} was measured using LIFT. On the second day, measurements were conducted indoors to determine ΦP_{max} using Maxi-PAM and LIFT.

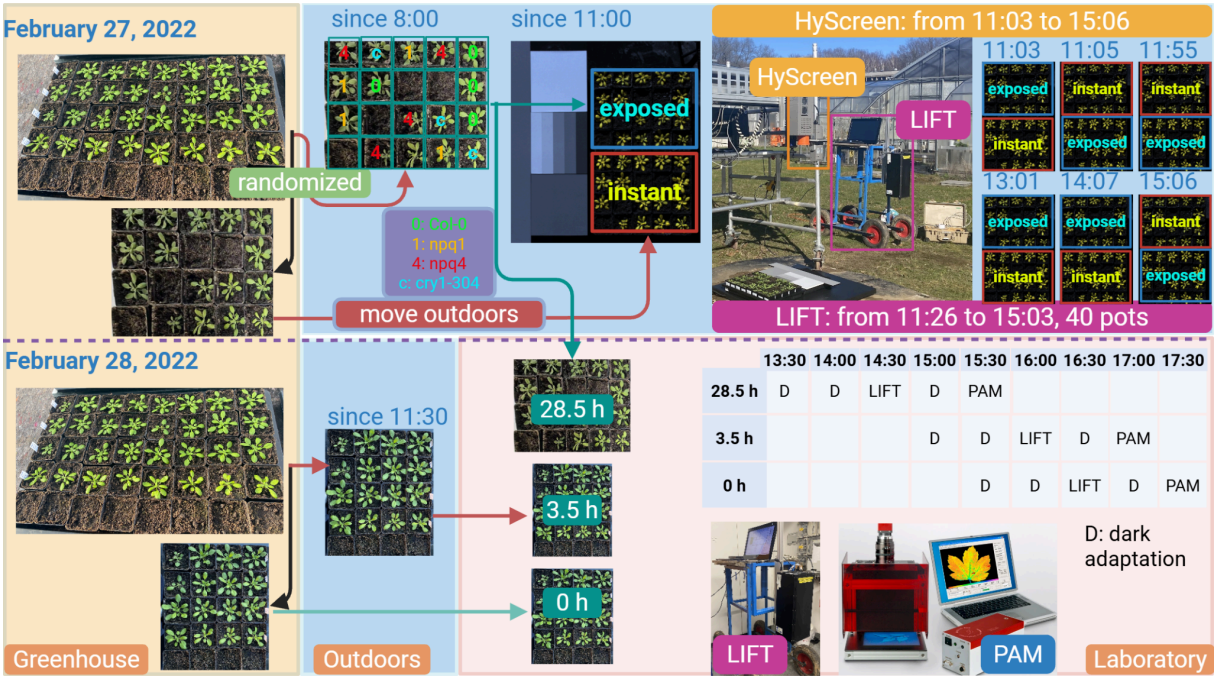

Figure 3.1 Design of cold stress experiments conducted outdoors for SIF dynamics (HyScreen) and ΦP measurements (LIFT), and in laboratory for ΦP_{max} (Maxi-PAM and LIFT). The different background colours represent three locations. Sixteen replicates per genotype were raised in the greenhouse from the same batch. On February 27, 2022, exposed plants were moved outdoors at 8:00 a.m. to acclimate to cold conditions, while instant plants were placed outdoors only immediately before the first measurement. Exposed plants remained outdoors overnight and were measured again the next day in the laboratory as the 28.5-h cold stress treatment together with 3.5 h cold treatment and

non-cold 0 h treatment. The figure also shows the schedule of LIFT and Maxi-PAM measurements for each treatment on February 28, 2022.

3.1.3. Setup of additional instruments

PAM imaging of maximum photosynthetic efficiency

An Imaging-PAM M-Series (Walz, Effeltrich, Germany) in MAXI version, shown in Figure 3.1, was used to measure active fluorescence. The measuring light, actinic light and saturating light were set to <1 $\mu mol_{photon} m^{-2} s^{-1}$, approximately 370 $\mu mol_{photon} m^{-2} s^{-1}$, and >5000 $\mu mol_{photon} m^{-2} s^{-1}$, respectively and applied for 800 ms. The wavelength of the measuring light was <680 nm to reduce the interference with induced fluorescence. Plants were dark-adapted for at least 30 minutes before F_0 and F_m were measured. The ImagingWinGigE V2.56zn Software (Walz, Effeltrich, Germany) was used to operate the device to acquire fluorescence images.

LIFT measurement of plant-level photosynthetic efficiency

The LIFT instrument (Version LIFT-REM, Soliense Inc., New York, USA) used in this experiment was designed to measure active fluorescence remotely. The Q_A flash protocol was employed in this experiment to measure the minimal and maximal ChlaF, which depend on the state of the primary quinone electron acceptor, Q_A, ranging from initial redox state of to the fully reduced state. The 0.75 ms induction phase consists of 300 flashlets with a 2.5 µs interval, and the 209 ms relaxation phase consists of 127 flashlets with a 1.6ms interval. A blue LED at 445 nm is embedded into LIFT as the excitation light, and fluorescence at 685 (± 10) nm is detected via its coaxial optical path. The LIFT monitors any background signal during inter-flashlet intervals and subtracts this signal from the in-flashlet ChlaF signal. The ChlaF yield is internally normalised to the excitation power of each flashlet, which remains constant throughout the entire FRR excitation phase.

The LIFT used was calibrated at a distance of 0.6 m to have an excitation power of 40,000 $\mu mol_{photon} m^{-2} s^{-1}$ during the ChlaF induction phase. The measurements were performed at the same distance from the TOC to obtain a focused area of 4 cm^2. The LIFT data collection and analysis were based on the methods described by Keller et al. (2019).

For estimating photosynthetic efficiency using LIFT measurements, F_{o-LIFT} and F'_{s-LIFT}, the first fluorescence transient recorded from the first excitation flashlet of the Q_A protocol, and F_{m-LIFT} and F'_{m-LIFT}, the average fluorescence transient from the 301st and 302st flashlets, are required. The ΦP_{max} from dark-adapted plants is calculated using Equation (3.1). The ΦP from plants under ambient light

is calculated by Equation (3.2). Finally, *NPQ* is calculated according to Equation 3.3.

$$F_v/F_m = (F_{m-LIFT} - F_{o-LIFT})/F_{m-LIFT} \quad (3.1)$$

$$F'_q/F'_m = (F'_{m-LIFT} - F_{s-LIFT})/F'_{m-LIFT} \quad (3.2)$$

$$NPQ = (F_{m-LIFT} - F'_{m-LIFT})/F'_{m-LIFT} \quad (3.3)$$

3.1.4. Light-adapted outdoor experiment

SIF and VI measurements outdoors

To quantify the diurnal changes of SIF, reflectance, and active fluorescence among different genotypes and treatments, six scenes of HyScreen and one set of LIFT measurements were acquired throughout the day on February 27, 2022. Two treatments with different cold exposure durations were implemented to investigate cold acclimation. The "exposed" treatment was taken outdoors starting at 8:00 a.m. to adapt to cold conditions, while the "instant" treatment was put outside just before the first measurement.

The trial was performed at Forschungszentrum Jülich, Jülich, Germany (lat 50.9096, long 6.412) (Figure 3.2) from 11:03 to 15:06 local time with a day air temperature from 0.9°C to 9.0°C (Figure 3.3). HyScreen was used to image the SIF and reflectance six times (shown in Figure 3.1) during the measurement period, and the pots in each treatment were randomised in the same way and measured together to ensure the same light condition. The measurement protocol was described in Section 2.2, and the data processing chain was described in Section 2.3. Additionally, the active fluorescence of each pot was measured once using LIFT in a random order starting at 11:36 using the protocol described in Section 3.1.3.

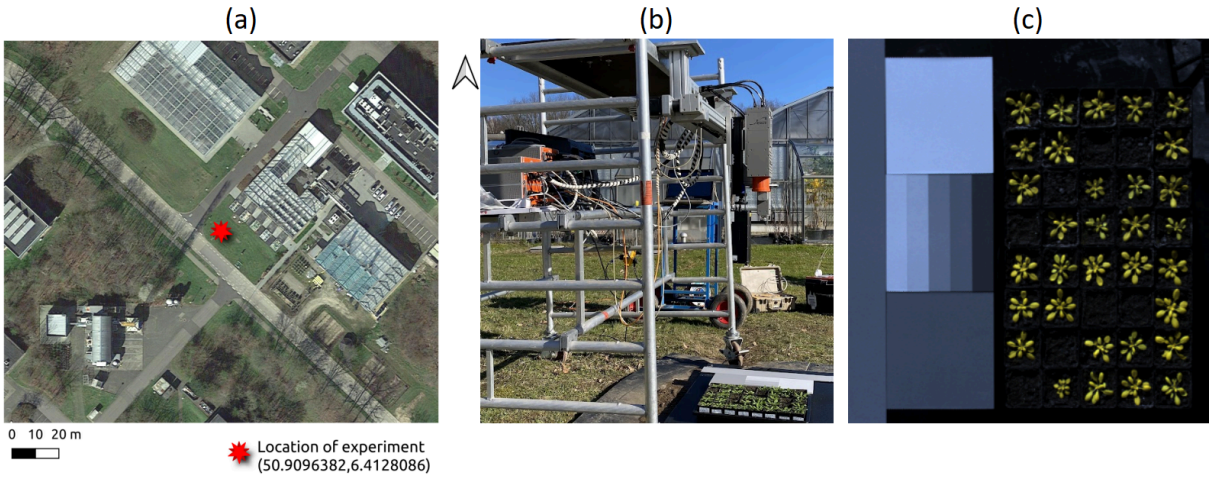

Figure 3.2 Outdoor measurements. a. Satellite image showing the measurement location. b. The setup of the HyScreen and measurement objects. c. False colour (R: 777.48 nm, G: 718.97 nm, and B: 689.52 nm) image representation of the experiment in nadir view acquired with the HyScreen FLUO module.

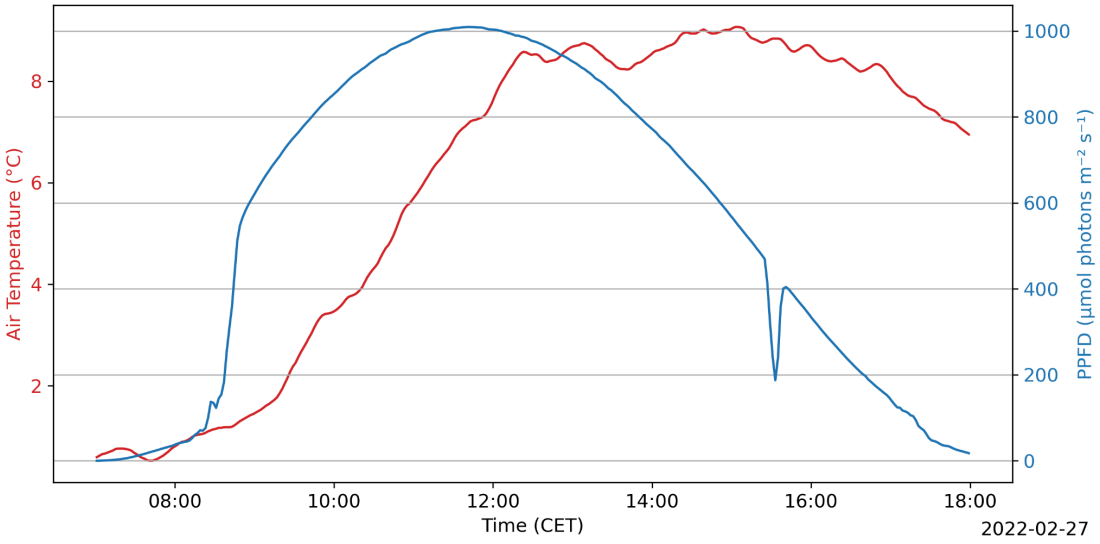

Figure 3.3 The temperature and photosynthetic photon flux density (PPFD) on the day of the experiment, February 27, 2022, are shown.

Individual plant segmentation for spatial analysis

Individual plant segmentation was conducted to allow genotype-level analysis, following the workflow from the Plantcv Python Package tutorial (Gehan et al., 2017). Instead of using the A-channel (green-red) of the CIELAB colour space, which is a colour model based on human colour perception, the NIRvR index derived from HyScreen hyperspectral imagery was used to separate vegetation from background (Figure 3.4 (a)). Based on the NIRvR histogram, a threshold value of two was applied to separate vegetation pixels from non-vegetation pixels (Figure 3.4 (b)), yielding a binary mask of vegetation Figure 3.4 (c). After removing noise by filtering out connected regions smaller than ten pixels, each remaining region was treated as an individual object Figure 3.4 (d). Next, circular ROIs corresponding to each pot arranged in an 8-row by 5-column grid. The grid was anchored at the plate's upper-left corner, to specify the inter-pot spacing, and to draw circles of 10-pixel radius to represent pot locations (blue circles in Figure 3.4 (e)). Each ROI was assigned a unique label for identification. Finally, labeled masks of individual plants were generated by intersecting each overlapped object (pot) with a labeled ROI (Figure 3.4 (f)). This workflow successfully isolated individual plants for downstream statistical analysis, providing that pots remained spatially separated. This workflow was also applied to VNIR imagery.

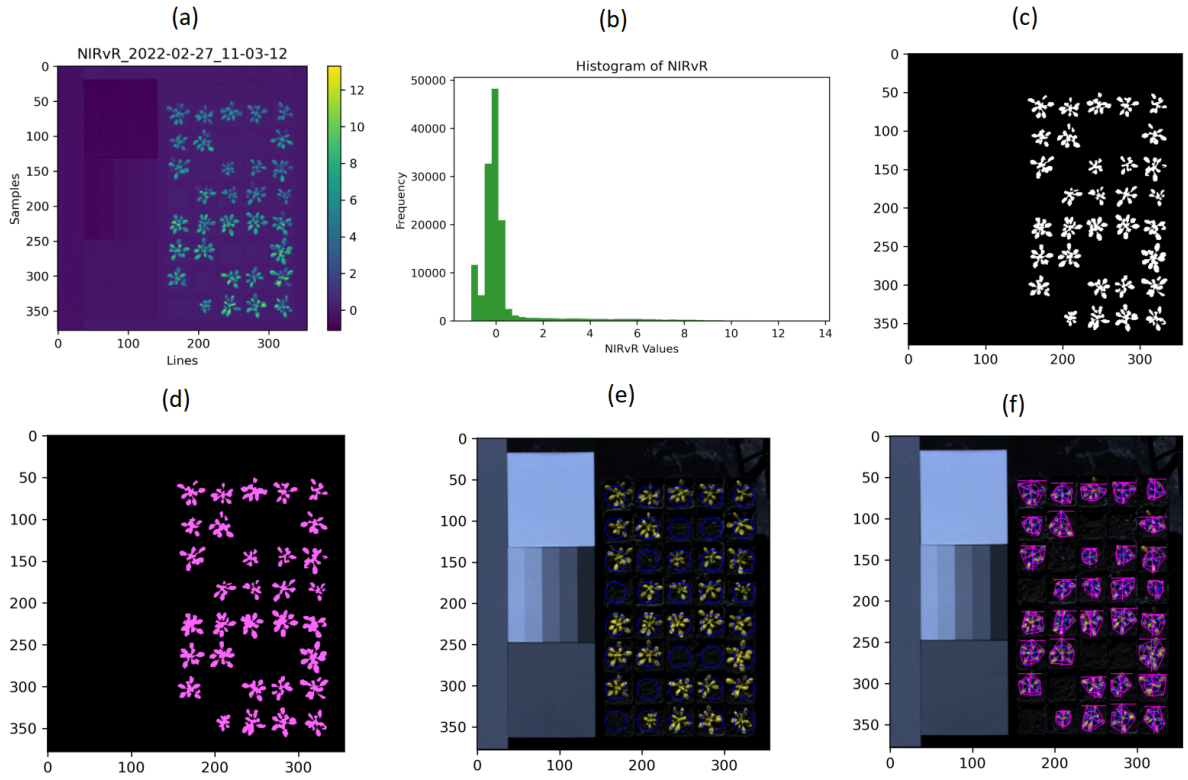

Figure 3.4 Workflow for segmenting individual plants from a HyScreen FLUO image. (a) NIR radiance of vegetation (NIRvR) image used for thresholding vegetation. (b) Histogram of NIRvR values. The threshold was set at NIRvR =2, so pixels with NIRvR > 2 were considered vegetation. (c) Binary vegetation mask after threshold segmentation. (d) Detected objects extracted from the vegetation mask. (e) Grid of region of interests (ROIs) in an 8-row by 5-column format, defined by the pot layout and position on the image. (f) Final segmented and separated individual plants by overlapping ROIs with the detected objects from (d).

Leaf-level sampling from HyScreen images

To investigate the effects of the leaf age, leaves from each individual plant were classified into two groups: young and mature. Young leaves were identified as those without an obvious petiole in the images. The image processing software Fiji (Schindelin et al., 2012) was used to annotate the ROIs of young leaves, and its overlap with plant mask (results from section 3.1.4) are considered the young leaf mask. The remaining parts of the plant mask were considered as the mature leaf mask. The 'Mask(s) from ROI(s)' plugin in Fiji was used to convert the annotated ROIs into binary masks shown in Figure 3.5. Due to the limited spatial resolution and manual annotation, some variability in this process is unavoidable. Additionally, the limited FOV of the VNIR sensor only allowed for imaging three columns of plants, which poses a limitation for statistical analysis.

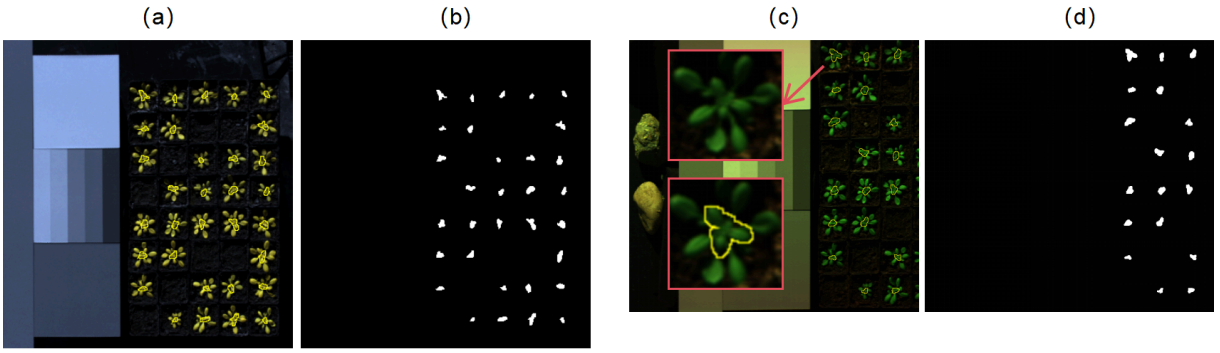

Figure 3.5 Original RGB images and their corresponding masks of ROIs for young leaves. Panels (a) and (b) are from the FLUO image, (c) and (d) are from the VNIR image.

3.1.5. Dark-adapted laboratory experiment

Laboratory measurement of maximum photosynthetic efficiency and photoinhibition

The Maxi-PAM and LIFT were used to measure the ΦP_{max} of individual plants in the lab on February 28, 2022, following the protocols described in Section 3.1.3. All the plants were dark-adapted at least for 30 minutes before measurement. To quantify the effects of cold exposure length in hours, the three treatments were "0 h", "3.5 h", and "28.5 h". Table in Figure 3.1 describes the schedule of LIFT and Maxi-PAM measurements. LIFT measurements began around 14:30 local time. Each plant was measured five times using the Q_A protocol, and the values were averaged to reduce noise. After the 30-minute LIFT measurements of 16 pots, each treatment plate underwent a 30-minute dark adaptation period before the Maxi-PAM measurement, which also took around 30 minutes per treatment plate.

Leaf-level sampling from Maxi-PAM images

The F_v/F_m (Equation (1.3)), from individual plants was extracted from nine regions of interest (ROIs) and then averaged. Three of the ROIs were selected from young leaves at the centre of each plant, and six were selected from mature leaves which have petioles. This approach allowed comparison F_v/F_m between young and mature leaves. Moreover, to quantify the photoinhibition level induced by cold stress, the average F_v/F_m from the “0 h” treatment for each genotype was used as a reference. The qI for each cold-treated (“3.5 h” or “28.5 h”) genotype was determined by Equation 3.4.

$$qI = (F_v/F_m)_{0\,h} - (F_v/F_m)_{cold} \quad (3.4)$$

3.1.6. Statistical analysis

For each individual plant, the outliers of SIF and VIs results were removed using the interquartile range (IQR = the data value at 75th percentile (Q3) - value at 25th percentile (Q1)) method, which exclude data points with values below the lower bound (Q1 - 1.5*IQR) and above the higher bound (Q3 + 1.5*IQR). For F760 and F687, the values less than zero were also excluded during statistical analysis. A two-way ANOVA function aov in stats package from base R (R Core Team, 2024) was used to compare the differences between treatments and between genotypes. Tukey's multiple comparison (function TukeyHSD) was used for significance calculation between groups.

3.2. Results of cold stress experiments

3.2.1. Spatio-temporal response of SIF during cold treatments

At the beginning of the measurements, plants under the instant treatment exhibited higher SIF yield than those under the exposed treatment. However, this difference gradually diminished as cold exposure progressed and eventually reversed (Figure 3.6). The temporal dynamics are shown in Figure 3.7. The instant treatment displayed a response resembling the Kautsky effect, characterized by a rapid decline in SIF yield immediately following the onset of cold stress, particularly within the first hour. In contrast, plants under the exposed treatment, which had experienced approximately 3 hours of cold exposure prior to the first measurement, showed a slight decrease and relatively stable SIF yield throughout the measurement period.

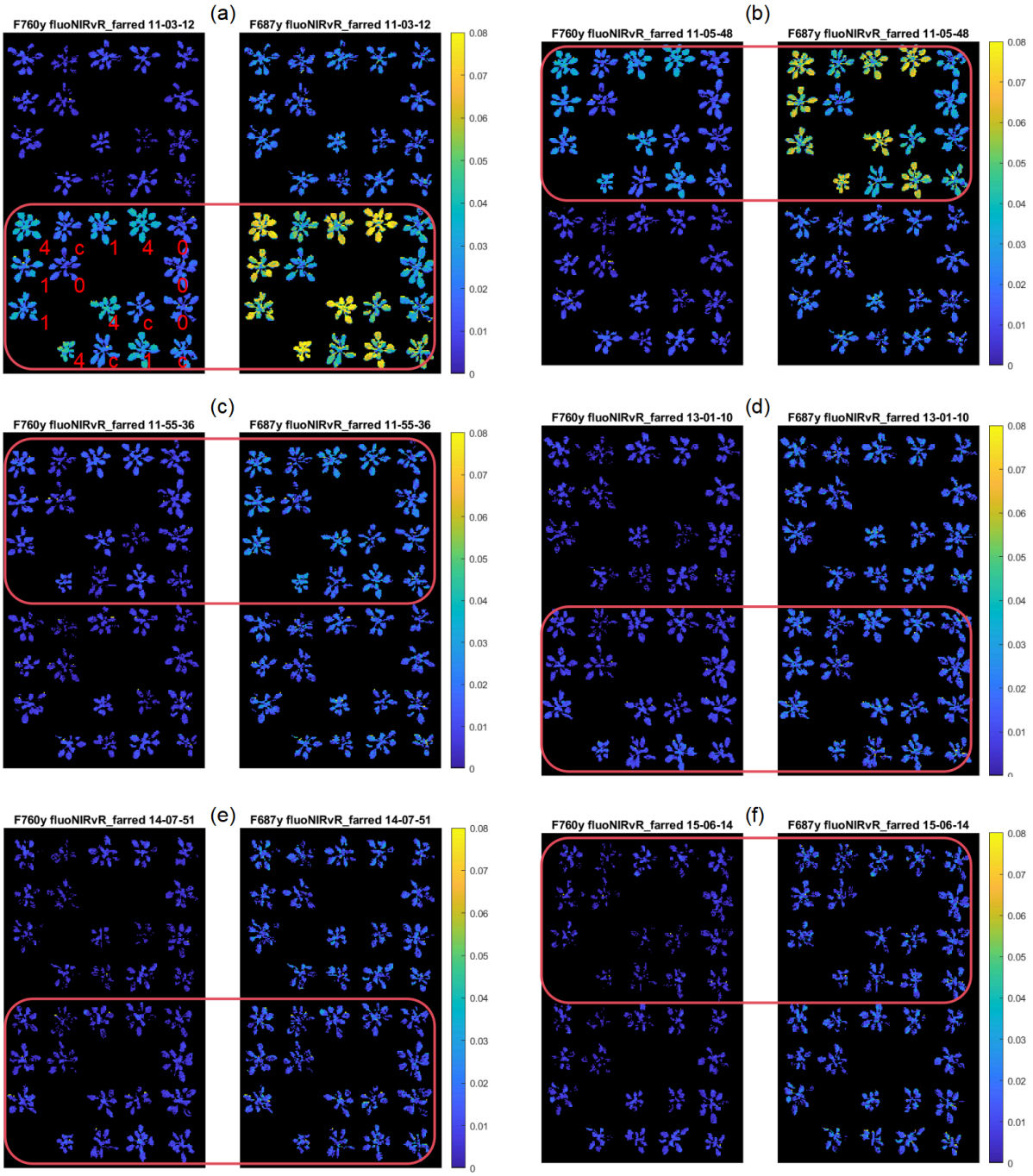

Figure 3.6 Time-series images of red and far-red solar-induced chlorophyll fluorescence (SIF) yield acquired by the FLUO sensor, with background pixels removed. Titles indicate the red or far-red SIF yield calculated as SIF/NIRvR and the corresponding measurement time (hh:mm:ss). Panels (a)–(f) show measurements at different time points. For each image, outliers and negative SIF values were excluded on a per-plant basis. Annotations "0," "1," "4," and "c" denote Col-0, *npq1*, *npq4*, and *cry1-304*, respectively. The red rectangle marks the instant treatment, which was transferred from the greenhouse to outdoor conditions immediately before the first measurement at 11:03. The remaining plants represent the exposed treatment, which had been subjected to low-temperature exposure since 08:00 on the measurement day. Treatment positions were rearranged for randomization.

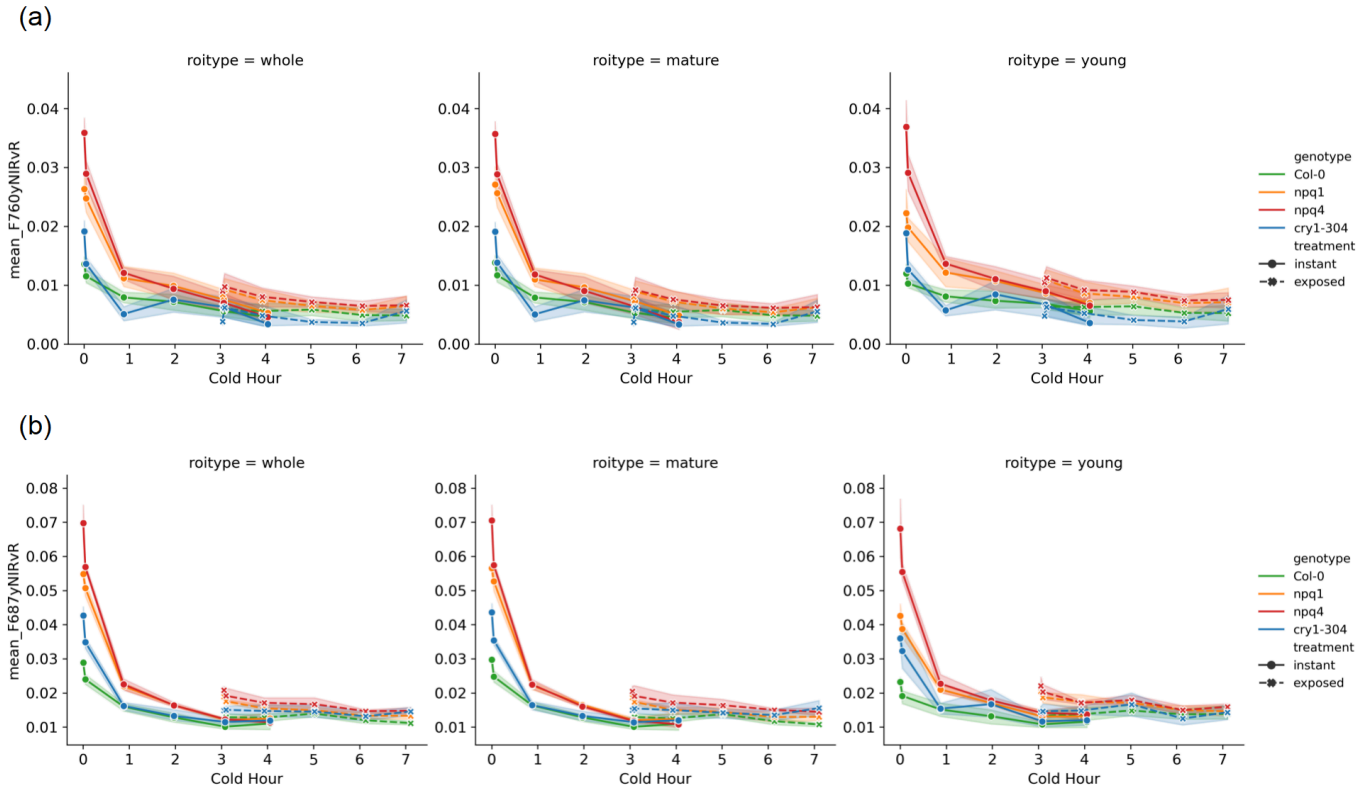

Figure 3.7 Time series of (a) F760 yield (F760y) and (b) F687 yield (F687y) under instant and exposed treatments. Results for "whole," "mature," and "young" leaves are shown in separate columns. Shaded bands indicate 95% confidence intervals. The x-axis represents the duration of cold stress experienced by the plants. The instant treatment was transferred from the greenhouse to outdoor conditions immediately before the first measurement at 11:03, whereas the exposed treatment had been subjected to low-temperature exposure since 08:00 on the measurement day.

3.2.2. Effect of reduced NPQ and cryptochrome deficiency on SIF

To assess the effects of NPQ deficiency and cryptochrome deficiency on SIF, time series of F760 yield (F760y) and F687 yield (F687y) were compared among genotypes shown in Figure 3.7. Under the instant treatment, *npq* mutants exhibited consistently higher SIF yield at both wavelengths than wild-type Col-0 and *cry1-304* during the first three hours of cold stress, with no clear differences thereafter. In the first two measurements (11:03 and 11:05; panels (a) and (b) in Figure 3.6), *npq4* showed the highest SIF yield, followed by *npq1*, *cry1-304*, and Col-0 shown in a closer comparison in Figure 3.8. Under the exposed treatment, SIF yields were similar among genotypes, although *npq4* and *npq1* still exhibited slightly higher SIF yield at both wavelengths at the beginning of the measurements.

For the cryptochrome-deficient mutant, *cry1-304* showed higher SIF yield than Col-0 at both wavelengths in the first two measurements under the instant treatment, with no clear differences thereafter. In contrast, under the exposed treatment, *cry1-304* exhibited lower F760y than Col-0 after prolonged cold exposure, while an opposite pattern was observed for F687y.

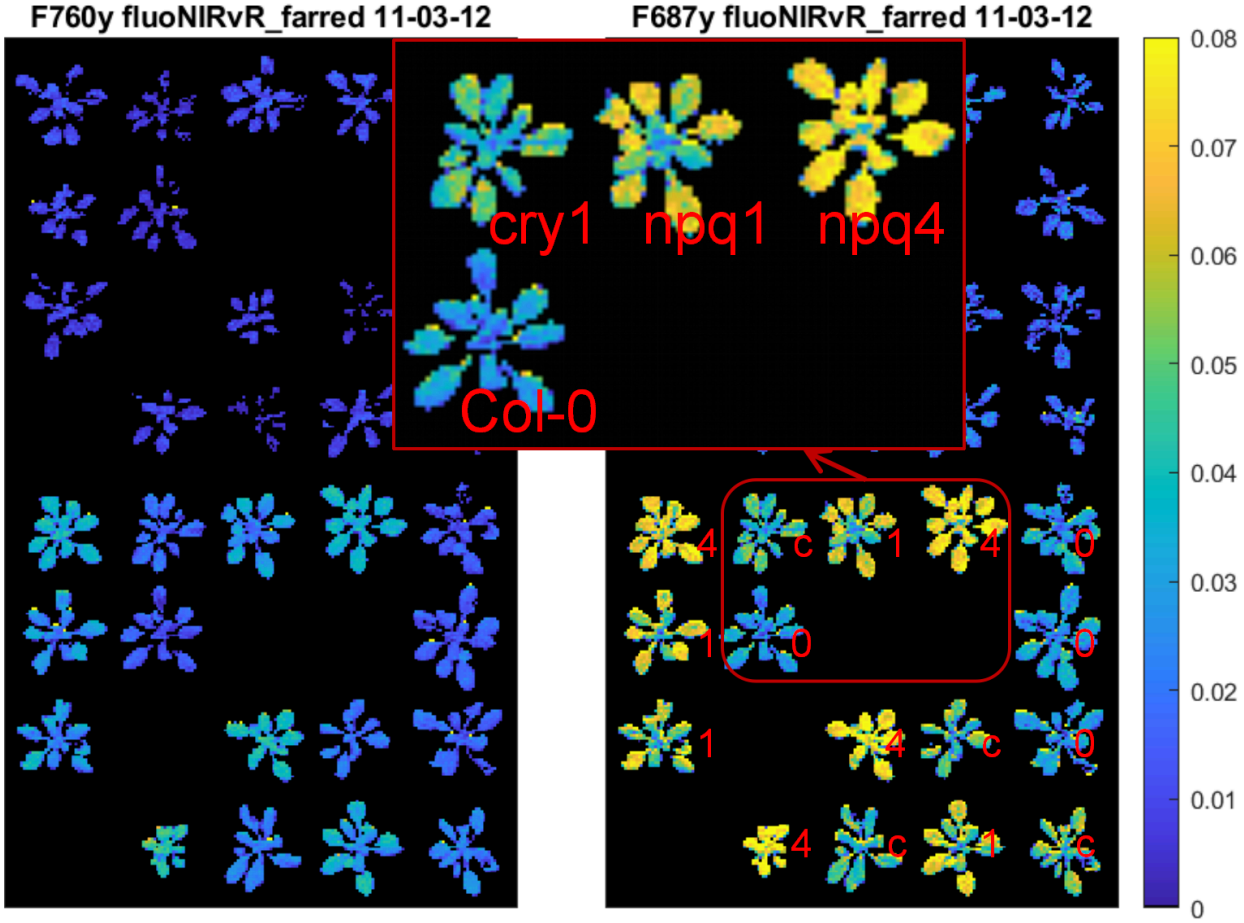

Figure 3.8 Spatial variation in solar-induced chlorophyll fluorescence (SIF) yield among Arabidopsis genotypes and leaves during the first measurement. The inset shows representative plants from four genotypes, highlighting differences between young and mature leaves, particularly in *npq4* under the instant cold treatment. Outliers and negative SIF values were excluded on a per-plant basis. Annotations "0," "1," "4," and "c" denote Col-0, *npq1*, *npq4*, and *cry1-304*, respectively.

3.2.3. Different response of leaf age in SIF

The first two measurements under the instant treatment (Figure 3.8) showed that young leaves exhibited lower F760y than mature leaves in *npq1* and Col-0, and lower F687y than mature leaves in all genotypes except *npq4*. At later time points, SIF yield in young leaves remained higher than in mature leaves, as indicated by the comparable or higher mean SIF values shown in Figure 3.9.

Under the exposed treatment, young leaves generally exhibited slightly higher SIF yield than mature leaves across all genotypes at both F760y and F687y, except for *cry1-304*, which showed minimal differences between leaf age groups in F687y.

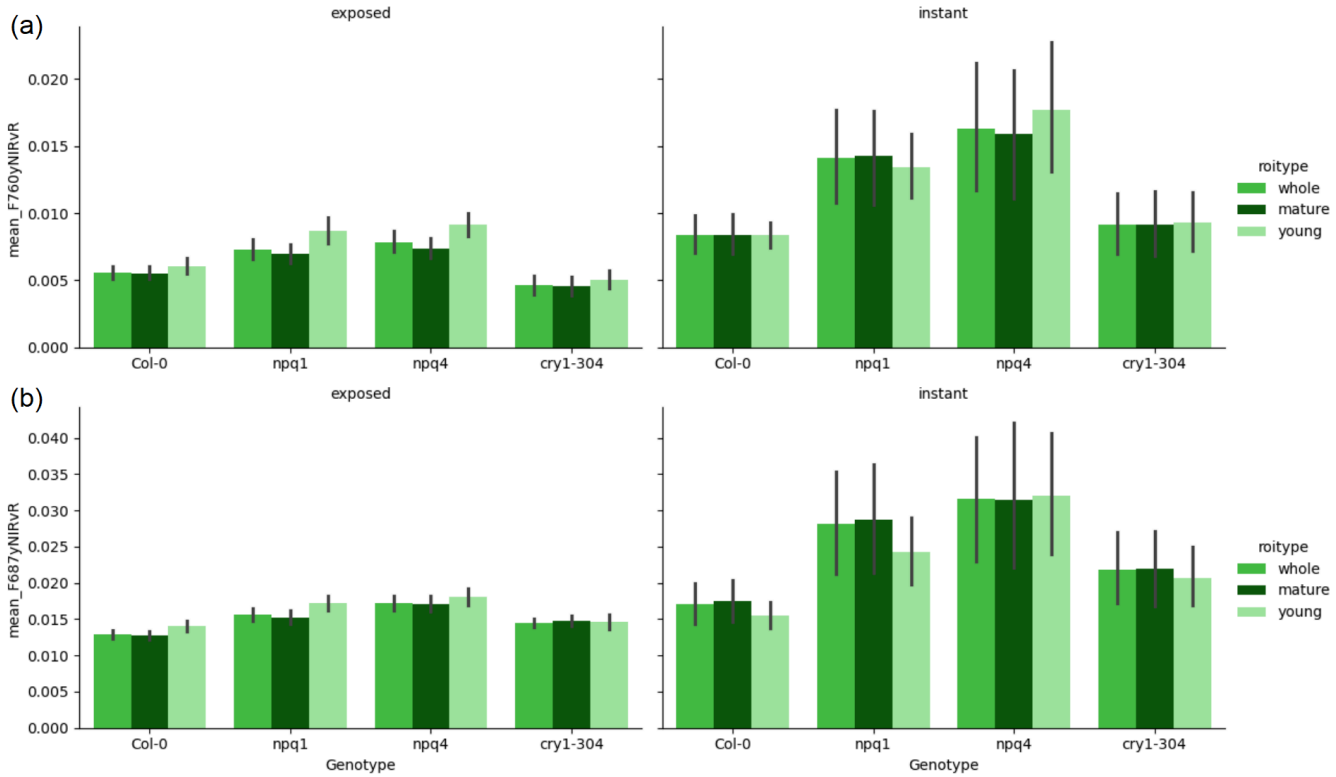

Figure 3.9 Bar plots comparing the effects of leaf age on SIF yield across all genotypes under both treatments. The instant treatment was transferred from the greenhouse to outdoor conditions immediately before the first measurement at 11:03, whereas the exposed treatment had been subjected to low-temperature exposure since 08:00 on the measurement day.

3.2.4. Reflectance spectra reveal changes in SIF and pigments

Reflectance spectra at oxygen absorption bands

The VNIR image captured at 11:03 (the first measurement) having both treatments were used for spectral analysis. Figure 3.10 illustrates spectral variations across genotypes and treatments. Comparison of the reflectance ratios between instant and exposed treatments for each genotype (Figure 3.11) shows that plants under the instant treatment exhibited higher reflectance at 687 nm and 760 nm relative to their shoulder bands across all genotypes, with a more pronounced effect in the *npq* mutants.

Figure 3.12 further compares spectral differences between mutants and wild-type Col-0 under the two treatments. Under the instant treatment, larger differences between Col-0 and the mutants were observed at the oxygen

absorption bands than at their shoulder bands. Under the exposed treatment, such differences were smaller and primarily at the O_2A absorption band and its shoulder band when comparing Col-0 with the *npq* mutants.

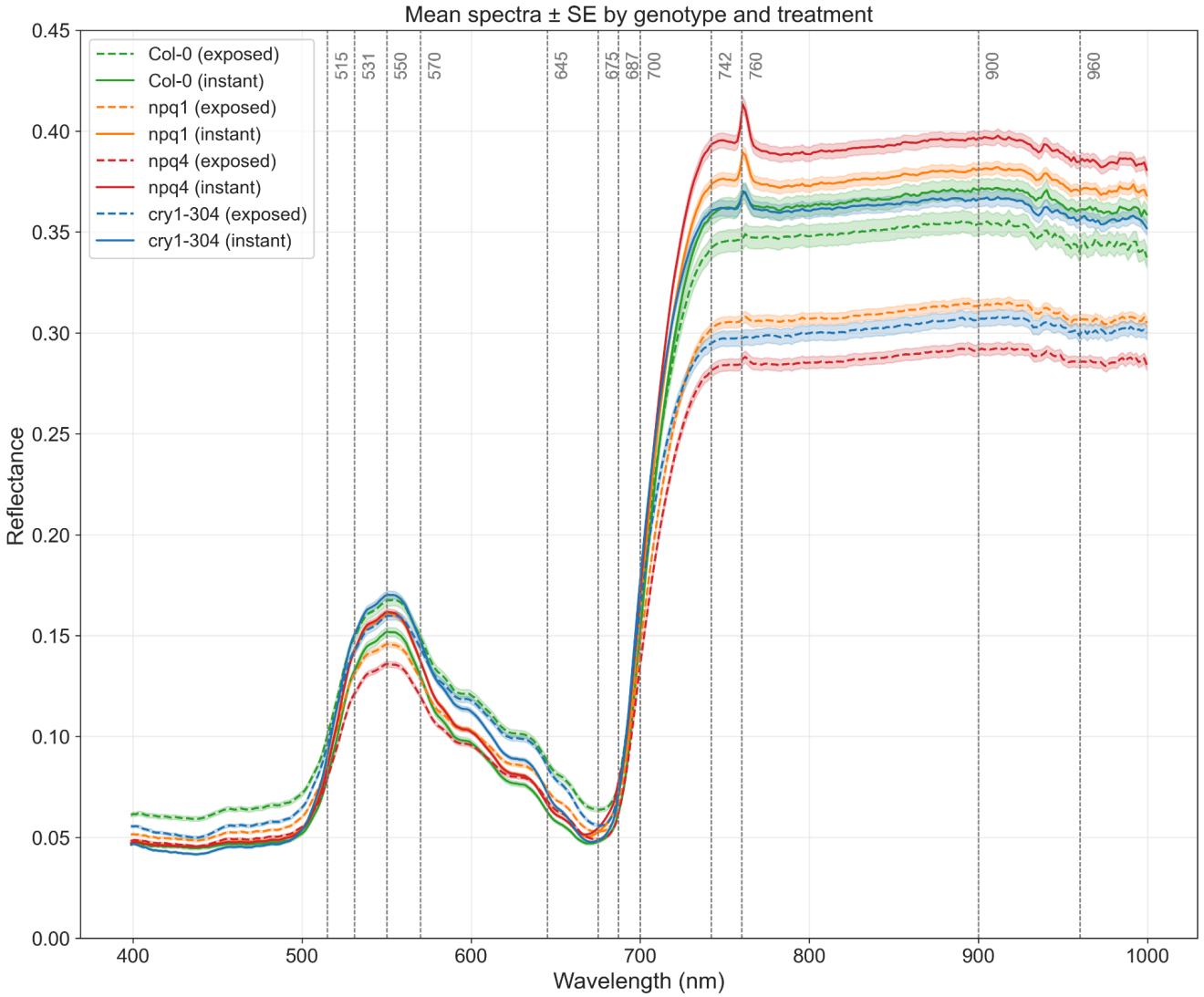

Figure 3.10 Spectral comparison derived from the VNIR image acquired at 11:03. Vertical gray lines mark selected wavelengths with labels. The instant treatment was transferred from the greenhouse to outdoor conditions immediately before the first measurement at 11:03, whereas the exposed treatment had been subjected to low-temperature exposure since 08:00 on the measurement day.

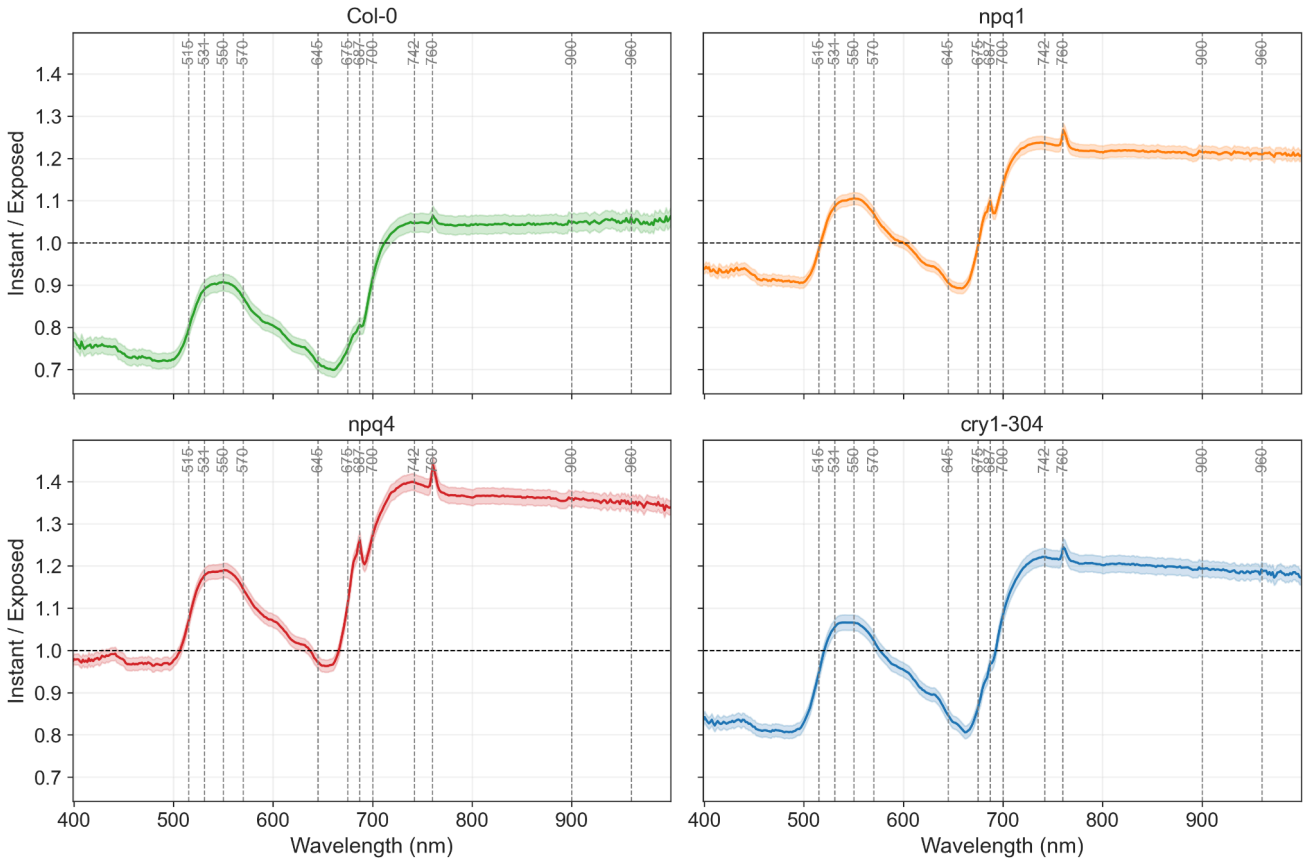

Figure 3.11 Ratio of reflectance between the instant and exposed treatments across genotypes. Values greater than 1 indicate higher reflectance under the instant treatment than under the exposed treatment. Vertical gray lines mark selected wavelengths with labels. Spectra were extracted from the first outdoor measurement at 11:03 by the VNIR sensor. The instant treatment was transferred from the greenhouse to outdoor conditions immediately before the first measurement at 11:03, whereas the exposed treatment had been subjected to low-temperature exposure since 08:00 on the measurement day.

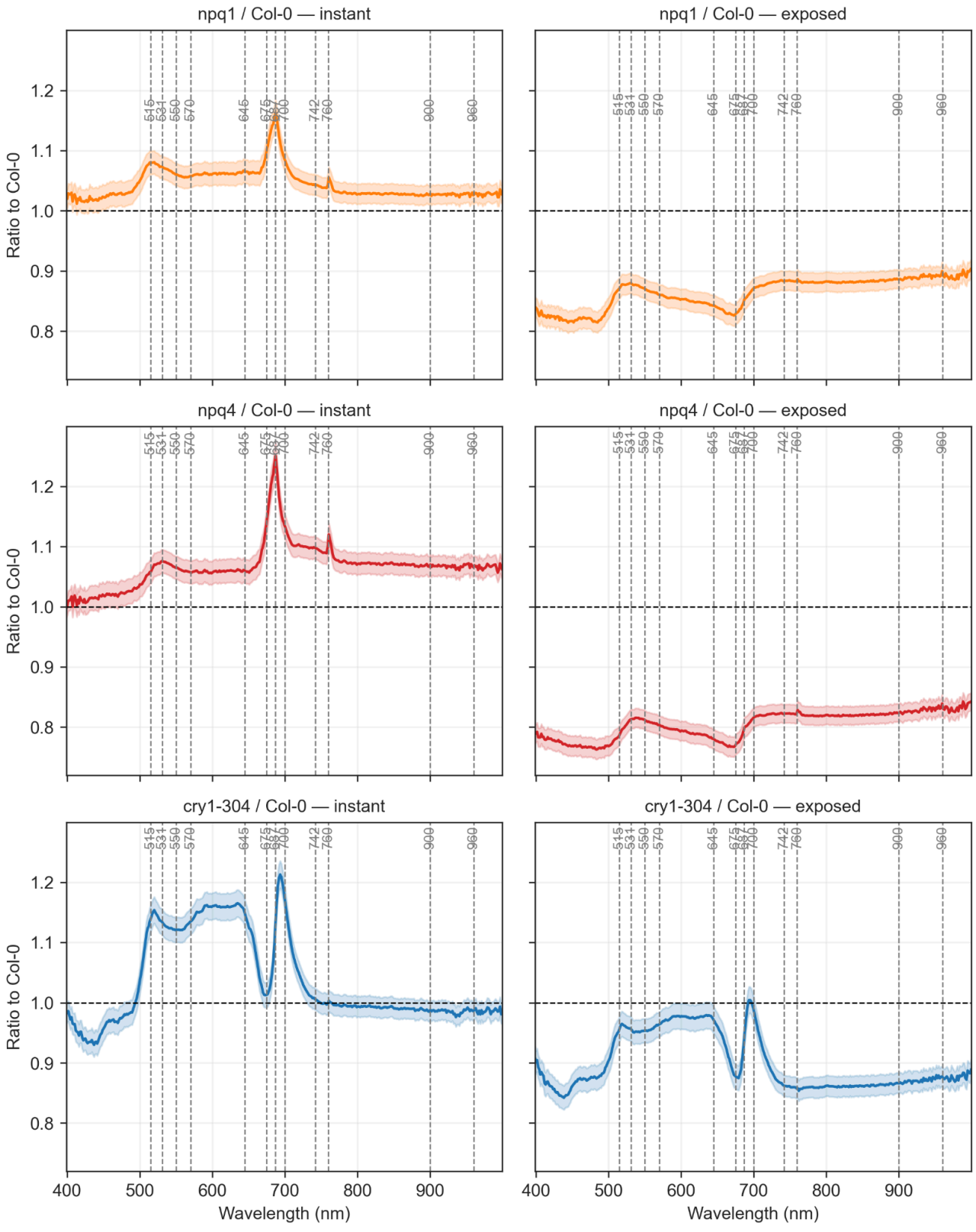

Figure 3.12 Ratio of reflectance spectra of *npq1*, *npq4*, and *cry1-304* relative to wild-type Col-0 under the two treatments. Values below 1 indicate higher reflectance in wild-type Col-0 than in the mutants. Vertical gray lines mark selected wavelengths with labels. Spectra were extracted from the first outdoor measurement at 11:03 by the VNIR sensor.

The instant treatment was transferred from the greenhouse to outdoor conditions immediately before the first measurement at 11:03, whereas the exposed treatment had been subjected to low-temperature exposure since 08:00 on the measurement day.

Different reflectance responses across spectrum under cold stress

Comparison of reflectance between the instant and exposed treatments (Figure 3.11) shows that, in the near-infrared (NIR) region, instant-treated plants exhibited markedly higher reflectance than exposed plants. In the visible (VIS) region, reflectance responses differed between the green and the blue/red spectral ranges. In the green region, instant-treated plants generally showed higher reflectance than exposed plants, with the exception of Col-0. In contrast, in the blue/red regions, exposed plants exhibited higher reflectance than instant-treated plants, except for *npq4*, for which little difference was observed between treatments.

Genotype differences in reflectance

As shown in Figure 3.12, under the instant treatment, Col-0 exhibited lower reflectance than both *npq* mutants across most wavelengths, with particularly pronounced differences in the 515–531 nm region and at the SIF-related bands (687 nm and 760 nm). Compared with Col-0, *cry1-304* showed higher reflectance from the green to red regions but lower reflectance in the blue region. Both genotypes exhibited similar reflectance near 675 nm and in the NIR, while differences were observed at the red-edge wavelengths and oxygen absorption bands. Under the exposed treatment, reflectance spectra of *npq1*, *npq4*, and *cry1-304* were consistently lower than those of Col-0 across wavelengths, although their overall spectral shapes were similar to those observed under the instant treatment.

3.2.5. Vegetation indices

Representative VI images derived from the first measurement of the VNIR sensor are shown in Figure 3.13. In addition to the VIs obtained from the FLUO sensor (Figure 2.12), the VNIR sensor provides complementary indices, particularly those related to carotenoids, anthocyanins, and water content. Based on the VI images from a representative scene (Figure 3.13), the indices can be grouped into five categories.

The first group, comprising NDVI and SR, effectively distinguishes between the two treatments but shows limited ability to differentiate among genotypes. These indices are also largely insensitive to illumination effects. The second group includes NDVIre and CIre, which combine one red-edge band with one NIR band and were normalized to reduce illumination effects. Both indices distinguish not only between treatments but also between *cry1-304* and the other genotypes. The third group consists of NIRv indices derived from red and NIR bands, which

primarily indicate APAR and pixel-level illumination. These indices exhibit nearly identical spatial patterns, although NIRv derived from the red band is several times lower than that derived from the NIR band, reflecting lower vegetation reflectance in the red and higher reflectance in the NIR region. FCVI shows similar pattern, capturing the influence of leaf angle and orientation on illumination. In all cases, higher values were observed under the instant treatment than under the exposed treatment.

The fourth group includes carotenoid-related indices, such as mCRIgreen, PRI, and CCI, all of which exhibited higher values under the instant treatment than under the exposed treatment. The final group comprises indices related to anthocyanin and water content. Both mCRI and mARI showed higher values in young leaves than in mature leaves.

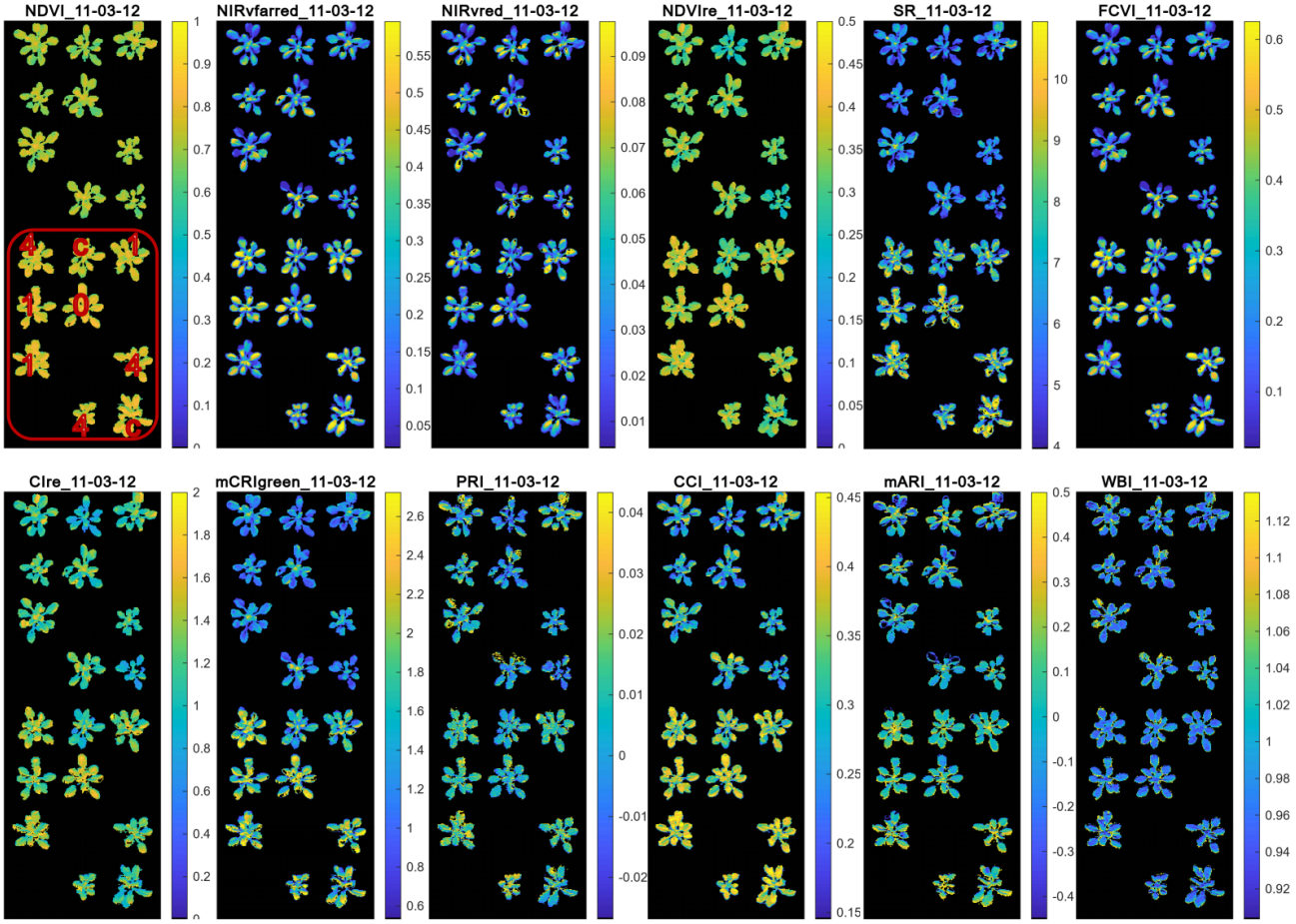

Figure 3.13 Vegetation index (VI) images derived from the first measurement of VNIR sensor with background pixels removed, corresponding to Figure 2.13. For each image, outliers were excluded on a per-plant basis. Annotations “0,” “1,” “4,” and “c” denote Col-0, *npq1*, *npq4*, and *cry1-304*, respectively. The red rectangle marks the instant treatment, which was transferred from the greenhouse to outdoor conditions immediately before the first measurement at 11:03. The remaining plants represent the exposed treatment, which had been subjected to low-temperature exposure since 08:00 on the measurement day. Treatments positions were rearranged for randomization.

Reduced chlorophyll content in *cry1-304* and under prolonged cold stress

Figure 3.14 shows the time series of NDVIre, highlighting consistently lower values in the exposed treatment across all genotypes. Under the instant treatment, NDVIre values declined primarily during the first hour of cold exposure. Among genotypes, *cry1-304* exhibited lower NDVIre than the other three genotypes under both treatments. In addition, young leaves showed higher NDVIre values than mature leaves for all genotypes under both treatments.

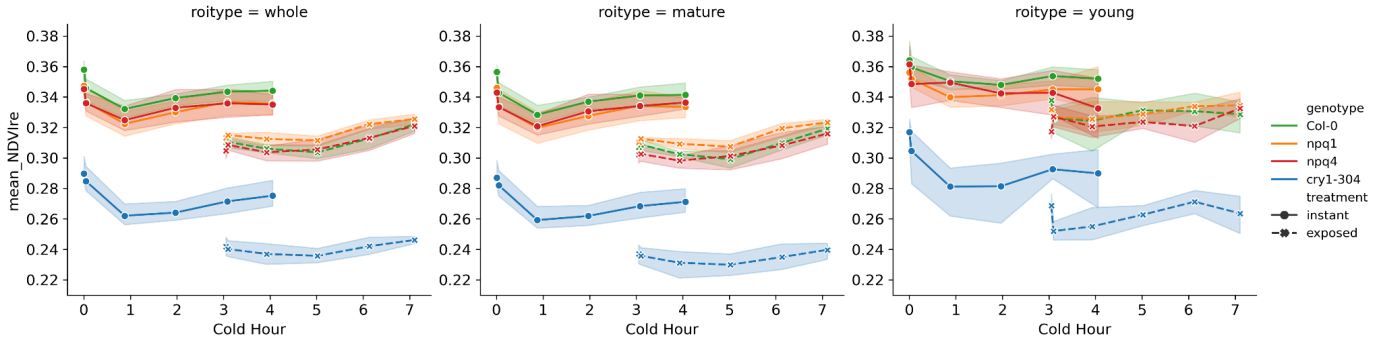

Figure 3.14 Time series of NDVIre under instant and exposed treatments derived from the VNIR sensor. Results for “whole,” “mature,” and “young” leaves are shown in separate columns. Shaded bands indicate 95% confidence intervals. The x-axis represents the duration of cold stress experienced by the plants. The instant treatment was transferred from the greenhouse to outdoor conditions immediately before the first measurement at 11:03, whereas the exposed treatment had been subjected to low-temperature exposure since 08:00 on the measurement day.

Xanthophyll cycle dynamics under cold stress

Time-series PRI revealed generally higher PRI values under the instant treatment than under the exposed treatment shown in Figure 3.15. Among genotypes, the *npq1* mutant, which lacks the ability to convert violaxanthin to zeaxanthin, exhibited the highest PRI, followed by *npq4*, Col-0, and *cry1-304*. Under the instant treatment, the largest decline in PRI occurred within the first hour after the onset of cold stress.

In mature leaves, PRI dynamics under both treatments closely followed changes in PAR, with the lowest PRI coinciding with the highest PAR across all genotypes. An exception was observed for the *npq* mutants under the exposed treatment, where the minimum PRI lagged approximately one hour behind the PAR maximum. In young leaves, PRI values under both treatments did not recover to initial levels during the measurement period.

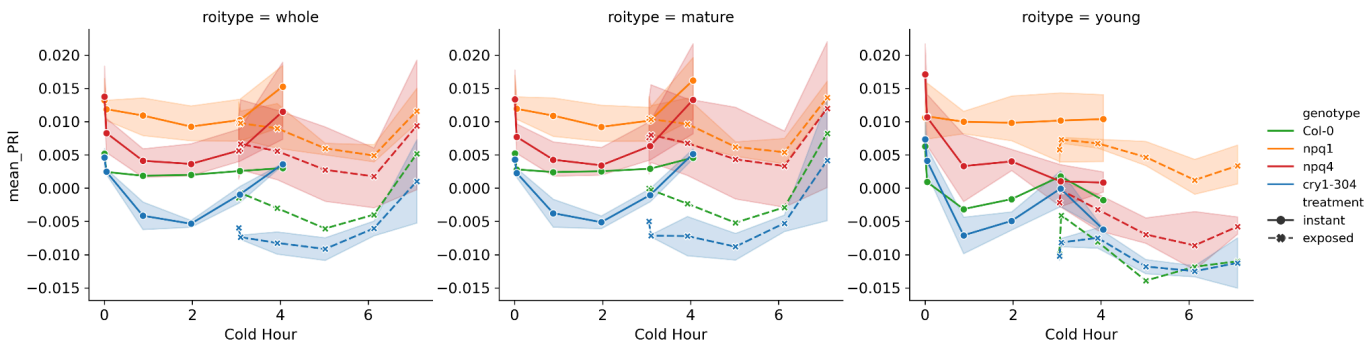

Figure 3.15 Time series of PRI under instant and exposed treatments derived from the VNIR sensor. Results for "whole," "mature," and "young" leaves are shown in separate columns. Shaded bands indicate 95% confidence intervals. The x-axis represents the duration of cold stress experienced by the plants. The instant treatment was transferred from the greenhouse to outdoor conditions immediately before the first measurement at 11:03, whereas the exposed treatment had been subjected to low-temperature exposure since 08:00 on the measurement day.

3.2.6. Dynamic energy partitioning quantified by active ChlaF

Photoinhibition increases with prolonged cold stress

The results from the Maxi-PAM measurements quantify the photosynthetic capacity and photoinhibition among the genotypes. Figure 3.16, reveals a substantial effect of periods of cold treatment on Fv/Fm. Fv/Fm decreases with an increase in the duration of cold exposure. The Fv/Fm exhibited no substantial variations across 0 hour cold treatment among the genotypes. The photoinhibition is defined as the difference between the Fv/Fm measured at 0 hours of cold and 3.5 or 28.5 h of cold exposure. In the 3.5-hour cold treatment, the *cry1-304* genotype exhibited a substantial decrease of Fv/Fm (~0.1) in comparison to the other three genotypes (>0.3). In the 28.5-hour cold treatment, Col-0 exhibited a significantly higher Fv/Fm than the remaining genotypes. In summary, *cry1-304* exhibited the most significant photoinhibition, with this effect being observed after a short time of 3.5 hours. In contrast, the Col-0 genotype demonstrated the least pronounced photoinhibition among the genotypes examined. Figure 3.17 showed that LIFT had similar results as Maxi-PAM. For each sample, the result is derived from the average of five Q_A flash protocol measurements. The overall pattern of the results is similar to that from Maxi-PAM.

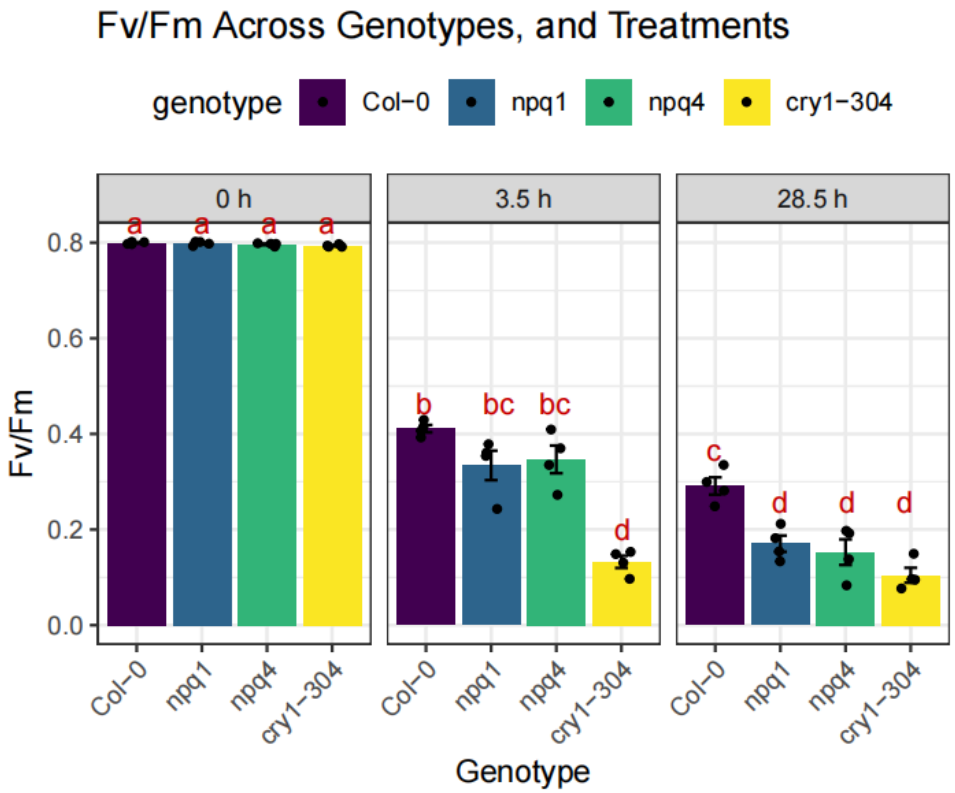

Figure 3.16: Maximum photosynthetic efficiency from PSII Fv/Fm of three differing periods of cold treatments and four genotypes. The error bars represent the standard error of the mean, with n = 4. The different letters above the bars indicate statistically significant differences between the samples (Two-way ANOVA analysis followed by Tukey's multiple comparisons test, $p < 0.05$.)

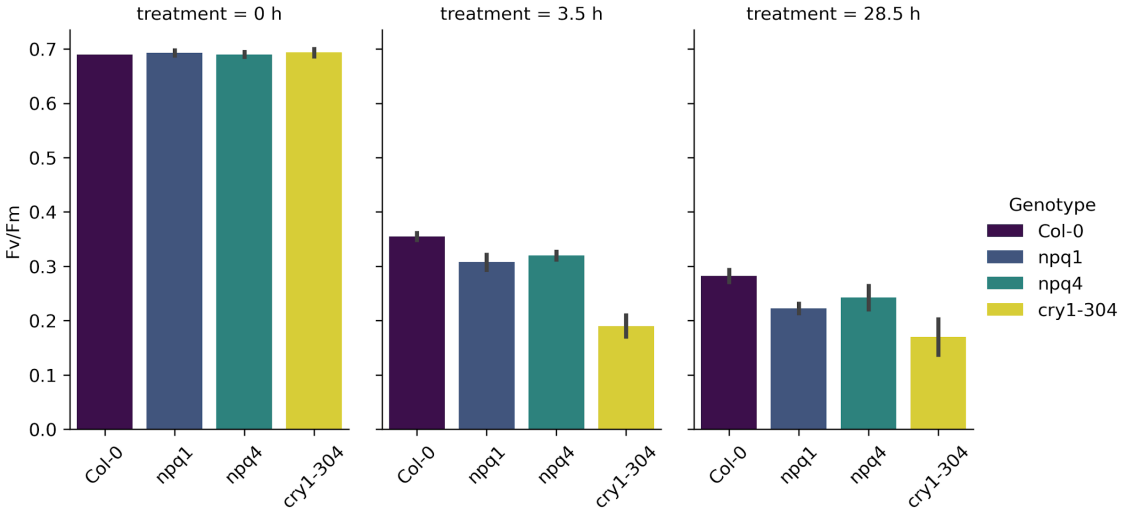

Figure 3.17 Maximum photosynthetic efficiency from PSII Fv/Fm of three differing periods of cold treatments and four genotypes. The error bars represent the standard error of the mean, with n = 4.

Younger leaves had lower photoinhibition than mature leaves under cold

Fv/Fm from LIFT and Maxi-PAM measurements in the laboratory showed consistency across treatments and genotypes. In terms of leaf age effects, under 0-h cold treatment, mature leaves exhibited slightly higher Fv/Fm than young leaves. In contrast, under both 3.5-h and 28.5-h cold treatments, young leaves consistently showed higher Fv/Fm than mature leaves (Figure 3.18). Across all treatments and genotypes, Fv/Fm differed significantly between young and mature leaves ($p < 0.0007$; young leaves: $n = 144$, mature leaves: $n = 288$), as determined by the Wilcoxon rank-sum test (Mann–Whitney test). Within each treatment–genotype group, the non-parametric two group Mann–Whitney test revealed significant Fv/Fm differences between young and mature leaves ($p < 0.01$; young leaves: $n = 12$, mature leaves: $n = 24$).

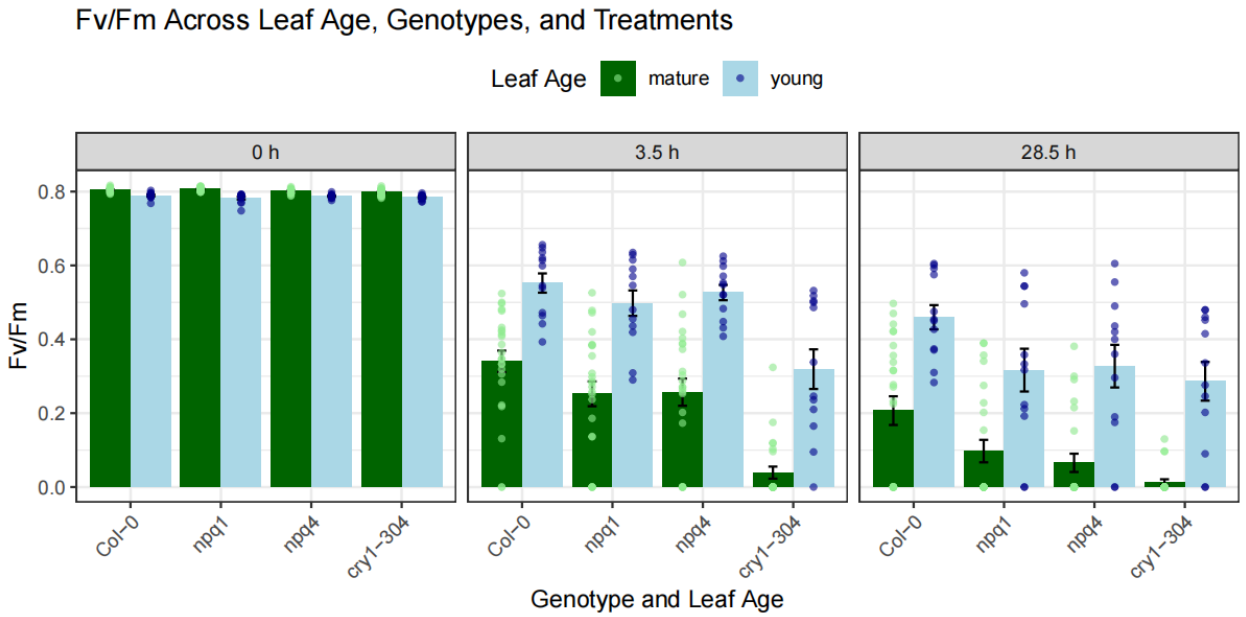

Figure 3.18: Comparison of the Fv/Fm between young and mature leaves across three periods of cold treatments and four genotypes. Within each treatment–genotype group, the non-parametric two group Mann–Whitney test revealed significant Fv/Fm differences between young and mature leaves ($p < 0.01$; young leaves: $n = 12$, mature leaves: $n = 24$).

Change of ChlaF parameters during the cold stress

Both F′ and Fm′ decreased during outdoor cold exposure under both treatments. In contrast, Fq′/Fm′ initially declined and then increased under the instant treatment, showing an inverse pattern relative to PAR, whereas it did not decrease under the exposed treatment shown in Figure 3.19. At the first measurement under the instant treatment, Col-0 exhibited noticeably higher Fq′/Fm′ than the other three genotypes.

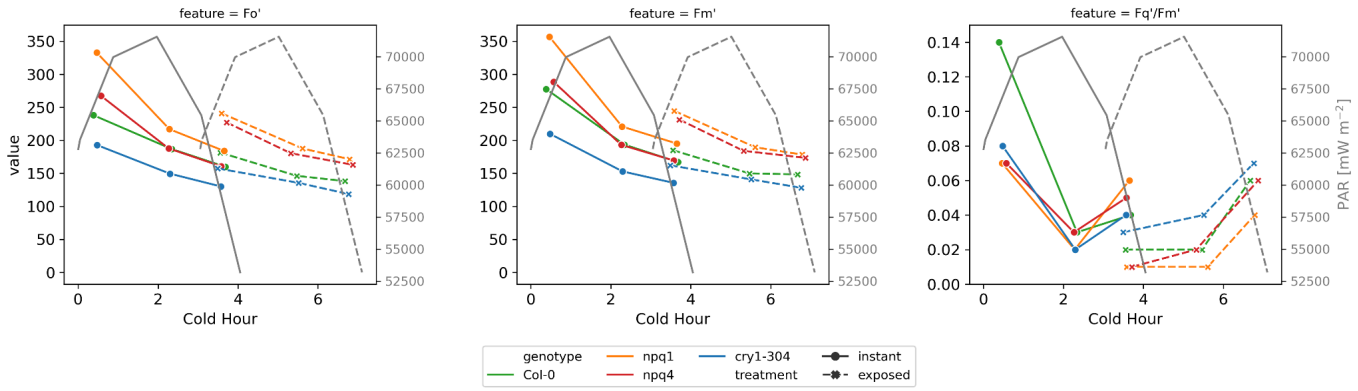

Figure 3.19 Time-series ChlaF parameters measured outdoors using LIFT. Note the lower temporal sampling density compared with the HyScreen measurements. Fs denotes ChlaF from light-adapted plants, Fm' denotes the maximum ChlaF from light-adapted plants, and Fq'/Fm' represents the operating photosynthetic efficiency, calculated as (Fm'-Fs)/Fm'.

Increase in NPQ during cold stress

Using Fm values measured in the laboratory from non-cold-stressed plants, NPQ was calculated for outdoor measurements over time following Equation 3.3. NPQ increased under both treatments during cold exposure, with stronger increases during periods of rising PAR and weaker increases during declining PAR shown in Figure 3.20. Under the instant treatment, NPQ followed the order *cry1-304* > Col-0 > *npq4* > *npq1*. Under the exposed treatment, *cry1-304* and Col-0 exhibited similar NPQ levels, both higher than those of the *npq* mutants, which also showed comparable NPQ levels.

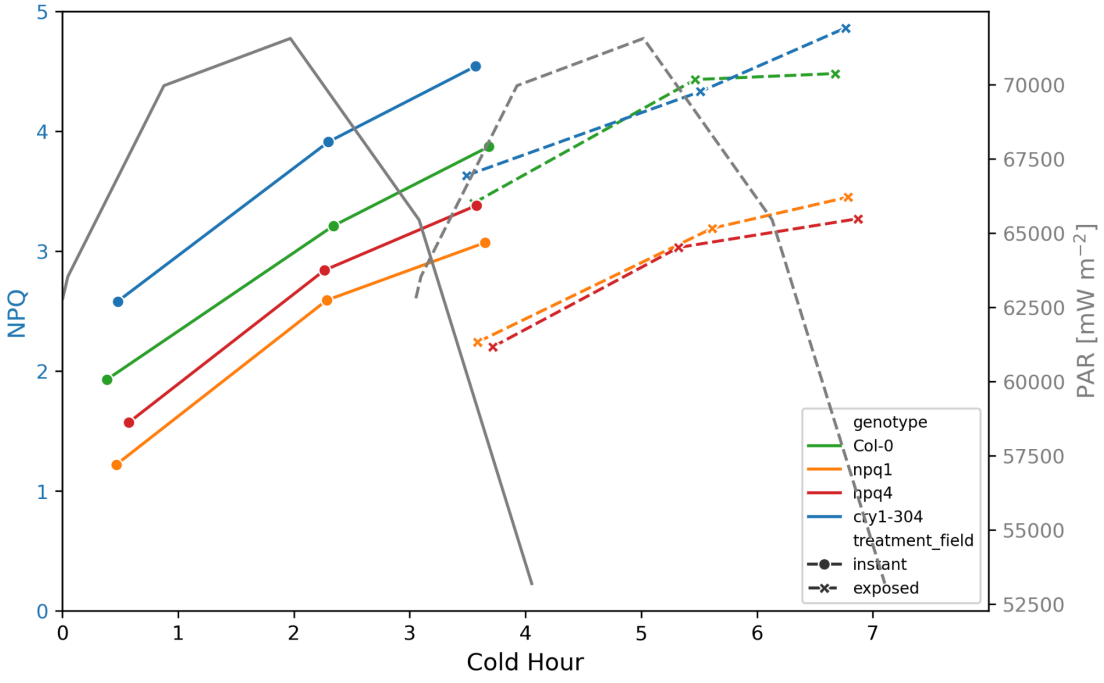

Figure 3.20 Time series of NPQ for plants under cold stress. The Fm values from non-cold control plants of each genotype were used to calculate *NPQ*. Note the lower temporal sampling density compared with the HyScreen measurements.

Less reversible NPQ in *cry1-304* and *npq* mutants than Col-0

Using Fv/Fm values measured in the laboratory after 3.5 hours of cold exposure, reversible NPQ was estimated for plants measured outdoors at a comparable duration of cold stress. Figure 3.21 shows that Col-0 exhibited higher reversible NPQ than *cry1-304* and the *npq* mutants. When considered together with total NPQ estimated in Figure 3.20, these results indicate that *cry1-304* experienced greater photoinhibition than Col-0.

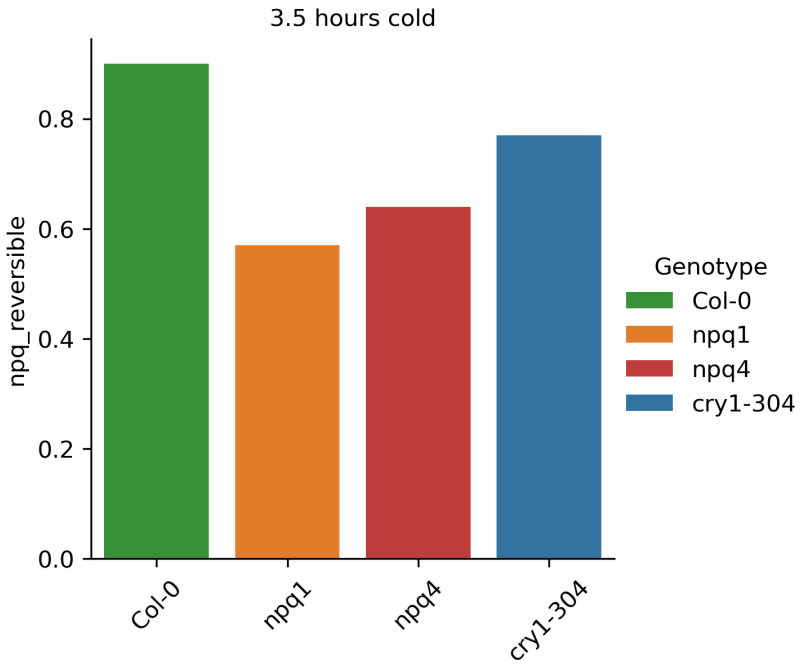

Figure 3.21 Reversible NPQ, calculated as ($Fm_{3.5h}$- Fm')/Fm', for plants exposed to 3.5 hours of cold under the instant treatment. $Fm_{3.5h}$ denotes the maximum fluorescence measured in the laboratory using LIFT from plants after 3.5 hours of cold exposure, and Fm' denotes the maximum light-adapted fluorescence of plants measured outdoors using LIFT.

4. Discussion

Parts of this chapter have been published in peer-reviewed journals:

Huaiyue Peng, Maria Pilar Cendrero-Mateo, Juliane Bendig, Bastian Siegmann, Kelvin Acebron, Caspar Kneer, Kari Kataja, Onno Muller, and Uwe Rascher. 2022. "HyScreen: A Ground-Based Imaging System for High-Resolution Red and Far-Red Solar-Induced Chlorophyll Fluorescence" Sensors 22, no. 23: 9443. https://doi.org/10.3390/s22239443

The table below indicates the origin of different sections within this chapter:

Newly added	Adapted *	Original
	Section 4.1.2	Everything else

4.1. Potential improvements in HyScreen data processing chain

4.1.1. Non-linearity and smile and keystone effects

Based on the results from the case study, we identified potential improvements for data collection as well as additional corrections for sensor characteristics that could be incorporated into the processing chain.

The ELM approach is based on the assumption that reflectance is linearly related to upwelling radiance. However, non-linearity is a known effect in spectroradiometers: meaning that an increase in the number of incident photons does not result in a proportional increase in the digital numbers recorded by the detector (Nehir et al., 2019; Schaepman and Dangel, 2000). Non-linearity is strongest at the lower and upper ends of the dynamic range of a detector. In our measurement protocol, the integration time is optimized for the scene, avoiding signal saturation while still reaching higher ends of the dynamic range. Meanwhile, calibration data from the FLUO sensor indicate that its linearity is quite good. The sensor's response to changes in integration time is relatively homogenous across wavelengths Figure 4.1. As shown in Figure 4.2, signal levels increase linearly with increasing integration time, even at short integration times. Therefore, non-linearity correction was not applied in the processing chain, considering the marginal benefits of such correction and potential risks of introducing other artefacts.

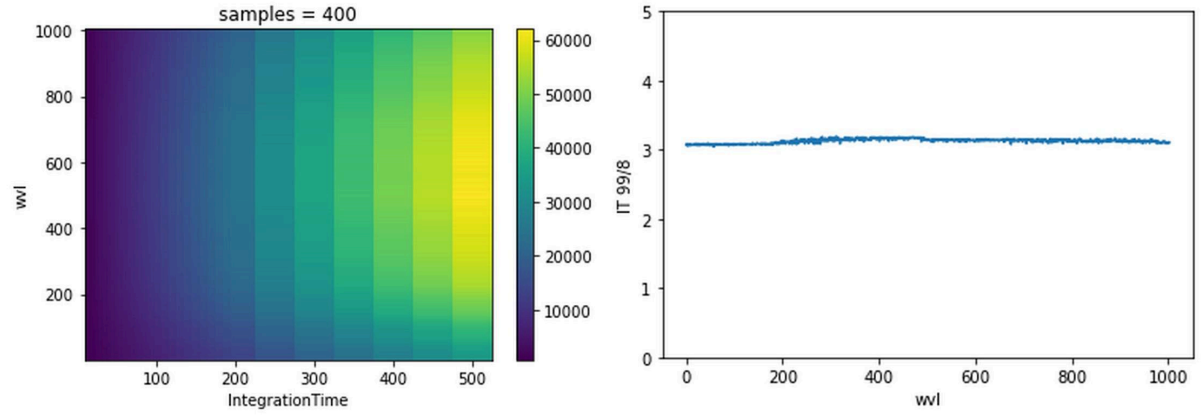

Figure 4.1. Non-linearity observation at the 400th spatial pixel. The left panel shows the signal level across different wavelengths as integration time increases. The right panel shows the ratio of signal levels with integration times of 99 ms and 8 ms, and the nearly flat line indicates consistent slopes of increase, suggesting a linear response.

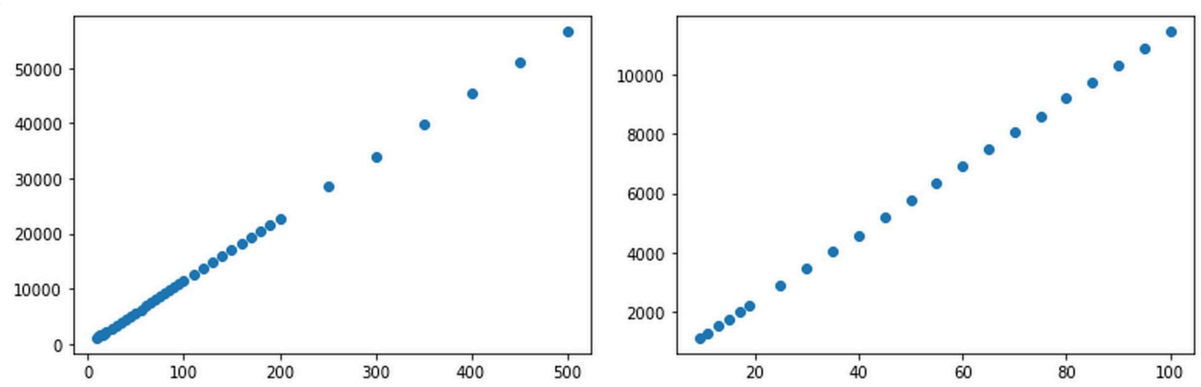

Figure 4.2. Linearity of signals at the 400th spatial pixel and 830th spectral pixel (760 nm). The left panel shows the linear increase in signal with increasing integration time (x axis); the right panel shows the signal linearity over the integration time range from 9 ms to 100 ms.

Grating-based spectrographs also suffer from smile and keystone distortions. Smile distortion results in a shift in wavelength in the spectral domain. This means that for spatial pixels in the same column, the recorded signals may not correspond to the same wavelength (Leung et al., 2022). Figure 4.3 shows the smile distortion observed in the FLUO sensor's detector. This is why we apply spatial sample-dependent radiometric calibration and ELM of radiance, as described in Section 2.3.4 and 2.3.5. Without these corrections, artefacts can appear in the reflectance data due to the mixing of spectra from different spatial samples. By using spatial sample-dependent methods, we can mitigate the impact of smile distortion during data processing.

Keystone distortion leads to the misregistration of the same object across different spatial pixels at different wavelengths. As a result, the spectrum from a given spatial pixel may contain signals from adjacent objects, which is particularly problematic at object edges. Unfortunately, HyScreen doesn't currently have calibration data to correct for keystone distortion during data processing. Both smile and keystone distortion correction should be included in future data processing chains. This would also simplify the measurement protocol, eliminating the need for spatial sample-dependent radiance correction, which requires a reference panel covering the entire FOV.

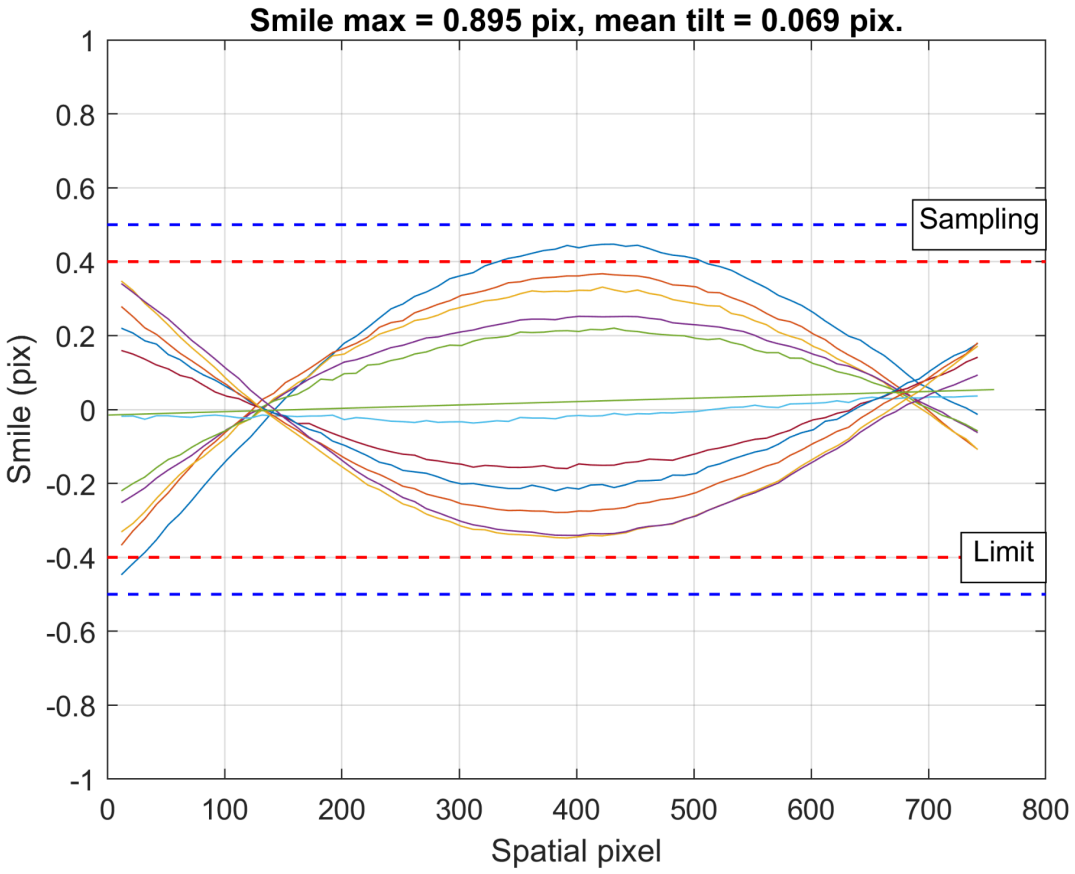

Figure 4.3 Smile distortion observed in the FLUO sensor. It shows that for different spatial pixels, the same wavelength (coloured lines) is registered on different rows of spectral pixels. The Oriel Instrument's spectral calibration lamps (Neon, Agron) were used for the wavelength calibration. (Credit: Spectral Imaging Ltd., Oulu, Finland)

Location effects may also influence SIF retrieval. For example, in the first two consecutive measurements, the same exposed-treatment plants exhibited higher F760 values in the second image, suggesting a position-dependent effect on SIF estimates. Although the randomized experimental design minimizes such effects in genotype comparisons, temporal trends within each treatment may appear less smooth due to this spatial variability.

4.1.2. Signal-to-noise ratio*

For SIF measurements, the SNR and spectral resolution are among the most critical parameters. They can even account for up to 40% of the error in SIF retrieval accuracy (Damm et al., 2011). The NER results in Section 2.4.2 indicate that darker panels exhibit relatively higher noise than brighter panels, which can lead to greater uncertainty in the SIF retrieval. These findings are consistent with the definition of SNR, where SNR is dependent on signal amplitude. For example, considering a typical vegetation target with 50% reflectance at the O_2A band, the relative error in SIF due to noise would range from approximately 0.2% to 0.5%

when the true SIF at 760 nm has value lies between 5 and 2 $mW \cdot m^{-2} \cdot sr^{-1} \cdot nm^{-1}$. For vegetation with only 5% reflectance at the O_2B band, the relative error would be at least between 0.4% and 1.0% when true SIF at 687 nm ranges from 2 to 5 $W \cdot m^{-2} \cdot sr^{-1} \cdot nm^{-1}$. In most modern spectroradiometers, the dominant source of noise is photon noise, which arises from the inherent random number of captured photons forming a Poisson distribution. The greater the expected hits of photons during the integration time, the higher the ratio of the expected value to its standard deviation of hits is, and thus the higher SNR is (Arroyo-Mora et al., 2021). Thus, to optimize SNR, the key is to both increase signal and reduce noise. First, measurements should be conducted under high illumination conditions, such as clear skies and solar zenith angles below 60° (Cendrero-Mateo et al., 2018). Additionally, spatial and spectral binning can reduce noise by averaging values of multiple pixels (Pinto et al., 2017). Furthermore, the integration time should be optimized to reach approximately 75% of the sensors' dynamic ranges to achieve optimal SNR (Medina et al., 2019). Based on these insights, we recommend using reference panels with reflectance not higher than those of the vegetation. This ensures the integration time can be optimized for the vegetation signal without causing saturation from brighter reference panels.

4.2. SIF and VIs as indicators of cold stress

By jointly analyzing the temporal dynamics of SIF, NDVIre, and spectra, plant responses to cold stress can be interpreted from biophysical, biochemical and physiological perspectives. Under the combined effects of low temperature and high illumination, photochemical processes were rapidly constrained, leading to an initial SIF response resembling the "Kautsky effect" (a rapid rise followed by subsequent decline in fluorescence) assuming relatively low steady-state SIF prior to cold exposure (Figure 3.7). This relatively high SIF yields was followed by progressive SIF quenching dominated by NPQ (Figure 3.20), with a rapid phase transitioning from fast to slower quenching over time. Most of these changes occurred within the first hour after acute cold exposure. In parallel, cold stress caused a reduction in NIR reflectance (Figure 3.10), indicating structural damage to leaf tissues. The reduced absorption in the blue and red spectral regions (Figure 3.10), seen from spectral comparisons between treatments, suggests degradation of chlorophyll content under prolonged cold exposure. Together, these results demonstrate that temporal SIF and VNIR-derived vegetation indices provide complementary information on both functional and structural plant responses to cold stress.

4.2.1. NPQ as the dominant mechanism of SIF quenching under cold stress

The timing of cold exposure strongly influenced the magnitude and kinetics of SIF yield by modulating the balance between photochemical and non-photochemical energy dissipation pathways. Consequently, SIF dynamics reflect the dominant quenching mechanisms operating during cold stress. Comparison of the instant and exposed treatments, Figure 3.7 shows that plants under the instant treatment exhibited higher SIF yield at the beginning of measurements. This was caused by the reduced photochemical activity seen from the large decline in Fq'/Fm' (Figure 3.19) and not yet fully developed NPQ as revealed in Figure 3.20 to the sudden increase in excess energy, including higher PAR, following transfer from the greenhouse to outdoor cold conditions.

Most SIF quenching occurred within the first hour of cold exposure (Figure 3.7), suggesting rapid establishment of NPQ during this period, then followed by slow components of NPQ afterwards. This is indicated by the relative steeper increase of NPQ in the first two hours shown in Figure 3.20. The reduction in Fv/Fm measured after 3.5 hours of cold stress (Figure 3.16) indicates that sustained NPQ accounted for at least half of the maximal Fv/Fm (~0.8) decline relative to unstressed controls, highlighting the dominant role of sustained NPQ associated with photoinhibition. These observations are in agreement with findings by Acebron et al. (2021) during the first day of the cold spell experiment. Ehlert and Hincha (2008) also demonstrated that decreasing temperatures led to substantial reductions in Fv/Fm and photosynthetic performance in Arabidopsis accessions. After approximately five hours of chilling, plants in the exposed treatment exhibited relatively stable SIF yield, consistent with near-saturation of NPQ (Figure 3.20).

These results also help answer the question whether cold stress increases or decreases SIF. The magnitude of SIF level depends strongly on the physiological state of the plant and the duration of cold exposure. Therefore, interpretation of cold-induced SIF responses requires explicit consideration of both steady-state SIF under non-stressed conditions and the timing of stress exposure. We can therefore infer that short-term cold exposure (within approximately one hour) is associated with increased SIF, whereas prolonged cold exposure leads to reduced SIF.

4.2.2. Structural and pigment-related changes under cold stress

Spectral analysis further revealed cold-induced changes in leaf structure and pigment change. As shown in Figure 3.10, prolonged cold exposure led to decreased NIR reflectance, which is indicative of alterations in leaf internal structure after 3 hours of cold stress. Wei et al. (2017) reported minimal changes

in SPAD-derived chlorophyll content during freezing stress but observed gradually decreasing leaf reflectance across wavelengths, attributing these changes to cellular structural modifications, including cell wall disruption and increased intercellular spaces. These structural damages likely reduced the total area of air–cell wall interfaces, thereby lowering reflectance in the NIR region (Jacquemoud and Ustin, 2019, p. 146).

In agreement with these observations, Vella et al. (2012) reported swollen and rounded chloroplasts under chilling stress, while Takahashi et al. (2024) showed that cold acclimation in Arabidopsis involves increased pectic galactan content in cell walls. Mutants with reduced galactan exhibited impaired freezing tolerance during early stages of cold acclimation, further supporting the role of cell wall modification in cold stress responses. Collectively, these studies indicate that cold stress reduces NIR reflectance primarily through structural changes in leaf tissues.

In addition, higher blue and red reflectance and lower green reflectance was observed in mutants, as well as higher visible reflectance in Col-0 under the exposed treatment compared with the instant treatment (Figure 3.11). The combined changes in reflectance across the VIS and NIR regions resulted in reduced NDVIre (Figure 3.14), indicating chlorophyll degradation under prolonged cold stress.

4.3. SIF and VIs in quantifying NPQ capacity

The kinetics of SIF yield provide insight into the qE capacity of each genotype, consistent with their genetic background. SIF yield, PQ, and different NPQ components (qE, qZ, and qI) are dynamic during photoprotection, particularly under stress conditions. For genotypes with comparable chlorophyll content, higher qE capacity is generally associated with lower development of qI, as demonstrated by comparisons between wild-type Col-0 and the *npq* mutants shown in Figure 3.7. However, chlorophyll degradation and slow PSII recovery become additional limiting factors. In *cry1-304*, relatively high qE capacity compared with the *npq* mutants appears insufficient to get less photoinhibition, indicating that photoprotection in this genotype is compromised despite intact qE machinery indicated by the first datapoint in Figure 3.7 and Figure 3.21. Moreover, PRI can serve as a useful proxy for total NPQ under prolonged cold stress, particularly when considering both its amplitude and temporal profile (Figure 3.15). NDVIre, as an indicator of chlorophyll content, showed larger fluctuations under cold stress in sensitive genotype *cry1-304*, suggesting that greater instability in NDVIre reflects increased susceptibility to the combined effects of cold and high light.

4.3.1. SIF yield under acute cold reflects qE capacity

As shown in Figure 3.7, the initial SIF yields under the instant treatment at both wavelengths reflect the qE capacity of the four genotypes, with lower SIF yield indicating higher qE capacity, particularly at 687 nm, which is dominated by fluorescence from PSII. This relationship is evident when comparing wild-type Col-0 with the two *npq* mutants. Both *npq* mutants exhibited higher SIF yield than Col-0, with *npq4*, which is deficient in PsbS, showing the weakest qE and the highest SIF yield, and *npq1*, which is deficient in the xanthophyll cycle, showing intermediate SIF yield. Similar patterns have been reported by Acebron et al. (2021) and Nilkens et al. (2010) for Col-0 and *npq* mutants genotypes. Although *cry1-304* has intact PsbS and a functional xanthophyll cycle, its qE capacity appears lower than that of Col-0 based on the SIF dynamics. At this early stage, SIF yield was generally inversely related to Fq′/Fm′ measured by LIFT (Figure 3.19), with Col-0 exhibiting the highest photochemical efficiency. The infilling features (bumps) at both 687 and 760 nm observed in SIF spectra (Figure 3.12) further support genotype-dependent differences in SIF amplitude.

4.3.2. Contributions of qE, qZ, and qI to SIF quenching

Across all genotypes, SIF yield decreased throughout the measurement period, indicating continuous quenching by NPQ. During the first hour, not only qE but also qZ and qI were developing as estimated by the formation time (Nilkens et al., 2010). In npq1, which lacks qZ, SIF quenching can be attributed mainly to increased qE and qI. In *npq4*, quenching was dominated by qZ and qI due to the absence of PsbS-dependent qE. In Col-0 and *cry1-304*, all three NPQ components contributed to total SIF quenching. Figure 3.20 shows that total NPQ amplitude followed the order *cry1-304* > Col-0 > *npq4* > *npq1*. When this pattern is compared with qE capacity inferred from the first two measurements (Col-0 > *cry1-304* > *npq1* > *npq4*) (Figure 3.7), it becomes evident that *cry1-304* accumulated more qI than Col-0 to reach a similar level of F687y or even lower F760y. This indicates a greater reliance on sustained NPQ and photoinhibition in *cry1-304*.

4.3.3. Relationship of changes in PRI and qZ

PRI is closely related to zeaxanthin content, with lower PRI values indicating higher zeaxanthin accumulation. However, absolute PRI values are not directly comparable across genotypes, as PRI also depends on baseline pigment composition. A more appropriate metric is $\Delta PRI = PRI - PRI_0$, where PRI_0 is measured under dark conditions. Although PRI_0 was not measured in this study, it can be assumed to be related to chlorophyll content (Tsujimoto and Hikosaka, 2021). Under this assumption, Col-0, *npq1*, and *npq4* have similar PRI_0, whereas *cry1-304* has a lower PRI_0. Based on the first measurement, Col-0 and *cry1-304*

likely accumulated zeaxanthin rapidly within the first minutes of cold exposure. The time-series PRI (Figure 3.15) shows that *npq1* exhibited the highest PRI, consistent with its deficiency in VAZ conversion. The general amplitudes of PRI among genotypes showed an inverse relationship with total NPQ (Figure 3.20), consistent with findings by Acebron et al. (2021).

Interestingly, PRI in Col-0 remained relatively stable after the first hour of acute cold exposure under the instant treatment, suggesting near-saturation of qZ. In contrast, PRI in *cry1-304* and *npq4* continued to decrease as PAR increased, indicating ongoing zeaxanthin accumulation at a slower rate which could be related to qI (Verhoeven, 2014). Towards the end of the day, although PAR decreased and qZ relaxed, SIF yield remained low, indicating accumulation of qI, consistent with the high level of NPQ (Figure 3.20) and reduced Fv/Fm measured in the laboratory (Figure 3.16).

4.3.4. Chlorophyll content, cryptochrome deficiency, and cold stress sensitivity

Chlorophyll degradation occurred during cold stress across all genotypes, with the strongest effect observed in *cry1-304*. This is evident from time-series NDVIre (Figure 3.14) and spectral analysis (Figure 3.11). Intrinsically, *cry1-304* has lower chlorophyll content than the other genotypes due to cryptochrome deficiency. Cryptochromes play a critical role in photoprotection under high light by promoting anthocyanin accumulation, maintaining chlorophyll content, and activating ROS-responsive genes in Arabidopsis (D'Amico-Damião and Carvalho, 2018; Kleine et al., 2007). Under cold stress, the accumulated ROS can damage the photosynthetic apparatus, leading to photobleaching and chlorophyll degradation. In the absence of CRY1, *cry1-304* is therefore more sensitive to the combined effects of high irradiance and low temperature. The largest decrease in NDVIre occurred within the first hour of cold exposure, highlighting the rapid onset of pigment degradation or chloroplast avoidance movement (Dall'Osto et al., 2014; Schmalstig and Jainandan, 2021; Schramma et al., 2023). Consequently, the capacity to maintain chlorophyll content under cold stress emerges as an additional indicator of photoprotection efficiency. Genotypes with higher chlorophyll stability are less susceptible to cold-induced photodamage.

4.4. Young leaves are more tolerant to cold stress

Young leaves have greater tolerance to cold stress, supported by their higher Fv/Fm measured in the laboratory (Figure 3.18) and existing studies (Bielczynski et al., 2017; Luklová et al., 2025). Comparison of young and mature leaves using SIF, PRI, and NDVIre indicates that young leaves exhibited higher qE capacity, higher qZ levels, and less chlorophyll degradation (indicated by higher NDVIre, Figure 3.14) during cold exposure. In addition, higher carotenoid- and

anthocyanin-related indices (mCRIgreen and mARI; Figure 3.13) in young leaves indicate greater amount of photoprotective pigments compared with mature leaves. Together, these traits suggest that young leaves dissipate excess energy more effectively and are less susceptible to photoinhibition under cold stress.

4.4.1. Enhanced qE capacity in young leaves

As shown in Figure 3.7, young leaves generally exhibited lower SIF yield than mature leaves from the first two measurements, which is indicative of higher qE capacity and stronger photoprotective energy dissipation. An exception was observed in npq4, where young leaves showed higher SIF yield than mature leaves. This suggests that the npq4 mutation, which disrupts PsbS-dependent qE, affects young leaves more strongly than mature leaves. However, the higher Fv/Fm observed in young leaves suggests that photoprotection over several hours involves mechanisms beyond NPQ, such as the accumulation of antioxidants including carotenoids (except β-carotene), vitamin E (α- and γ-tocopherol), and non-photosynthetic pigments such as anthocyanins and other flavonoids (Havaux and Kloppstech, 2001). In contrast, npq1 plants exhibited lower SIF yield in young leaves than in mature leaves, indicating relatively stronger photoprotection in young leaves despite impaired xanthophyll cycling, in agreement with the findings of Havaux et al. (2000). The distinct spatial patterns of SIF yield in npq1 and npq4 highlight genotype-specific differences in photoprotection across leaf developmental stages. These results emphasize the critical role of PsbS-dependent qE for protecting young leaves during early leaf development, particularly under cold stress.

4.4.2. Greater contribution of qZ to total NPQ in young leaves

Differences between young and mature leaves were also evident in PRI dynamics (Figure 3.15). In mature leaves, PRI exhibited a pronounced “U-shaped” temporal pattern, whereas in young leaves PRI decreased and then remained relatively stable until the end of the measurement period, even as irradiance declined. This behavior suggests more qZ activity in young leaves compared with mature leaves. In *npq1*, PRI in young leaves remained nearly constant, consistent with the absence of a functional VAZ process, whereas mature leaves showed slight PRI variation, indicating limited zeaxanthin dynamics. Notably, young leaves of *npq4* exhibited Fv/Fm values comparable to those of *npq1* (Figure 3.18), despite retaining a functional xanthophyll cycle. This suggests that qZ plays a particularly important compensatory role in protecting the under stress, especially in young leaves where PsbS-dependent qE is most strongly reduced.

4.5. Uncertainties in estimation of SIF yield

Multiple factors contribute to uncertainty in the estimation of SIF yield, most notably APAR and the SIF escape probability. With respect to APAR, the incident PAR reaching different points on a leaf surface varies substantially due to the geometry among solar position, leaf inclination, and sensor viewing angle. In addition, the fraction of PAR actually absorbed by leaves depends on biophysical, biochemical, and physiological properties, including leaf thickness, pigment content, and developmental stage. As a result, APAR is highly dynamic, influenced by solar movement, leaf motion, and changes in plant physiological status. For example, in Arabidopsis, leaf inclination angles increase under low light as a shade-avoidance response and decrease under high light, a response mediated by blue-light signaling (Ballaré and Pierik, 2017). I observed that plants grown in the greenhouse exhibited larger leaf inclination angles than plants exposed to cold stress for more than 24 hours. However, this pattern was not observed in the plants used in this cold stress experiment, maybe due to their younger developmental stage. Moreover, reductions in chlorophyll fluorescence yield are not always driven by regulated NPQ. They can also arise from decreased light absorption due to chloroplast avoidance movements or state transitions under high irradiance (van Amerongen and Croce, 2025). Quantifying the relative contributions of these mechanisms across different environmental conditions remains challenging (Porcar-Castell et al., 2021).

4.6. Conclusion and outlook

In summary, HyScreen provides reliable SIF and VI products through a carefully designed measurement protocol and data-processing chain. A key advantage of the HyScreen system is its high spatial resolution, which allows separation of vegetation signals from soil background and resolving individual leaves. As such, HyScreen serves as an intermediate-scale instrument bridging the gap between the photosystem and the canopy. This capability offers opportunities to better constrain APAR and SIF escape probability by accounting for leaf-scale structural and biochemical heterogeneity. For example, it enables segmentation of individual plants and even individual leaves(Figure 3.4), which may be possible to infer leaf inclination dynamics under varying environmental conditions, offering additional context for interpreting SIF yield variability. Furthermore, integration with radiative transfer models may allow retrieval of pigment contents (Féret et al., 2021), helping downscale SIF to photosystem level. facilitating the downscaling of SIF signals toward the photosystem level. Together, these features highlight the strong potential of HyScrren to reduce uncertainties in SIF interpretation by explicitly incorporating spatial and structural information.

The cold stress experiment demonstrates that the temporal profiles of SIF and VIs can be used to infer distinct stages of plant responses to cold stress, including NPQ development, changes in chlorophyll content, and alterations in leaf structure. Results from the four mutants indicate that photoinhibition is determined not only by the capacity for reversible NPQ but also by the plant's ability to scavenge reactive oxygen species (ROS) and maintain chlorophyll content. Comparison of young and mature leaves further suggests that, in addition to NPQ, other photoprotective mechanisms may contribute to protecting young leaves, as evidenced by their better maintenance of chlorophyll and higher zeaxanthin levels.

Regarding photosystem engineering, studies in Arabidopsis and other plant species have shown that maximum NPQ capacity can be paradoxically associated with lower biomass when NPQ relaxation is slow, underscoring the importance of NPQ dynamics rather than NPQ magnitude alone. Previous studies have demonstrated that biomass in tobacco and seed yield in soybean can be improved by accelerating NPQ relaxation through overexpression of VDE, PsbS, and ZEP. These findings suggest that future efforts in plant breeding should focus on reducing the contribution of slow NPQ components, particularly sustained NPQ, to enhance photosynthetic efficiency and productivity (Croce et al., 2024).

Similarly, the strategy of reducing antenna size to improve photosynthetic efficiency is not universally beneficial. Although lowering chlorophyll content can reduce light competition within dense canopies, its impact on photosynthetic performance and yield is species dependent. For example, tobacco plants with reduced antenna size and rice cultivars with paler leaves have shown improved performance, whereas chlorophyll-deficient soybean exhibited reduced photosynthetic efficiency, lower NPQ capacity, slower NPQ relaxation, and decreased leaf mass and grain yield (Acebron et al., 2022; Croce et al., 2024). These contrasting responses emphasize that optimal photoprotection strategies depend on species-specific balances between light harvesting and energy dissipation.

Importantly, our results demonstrate that the dynamics of SIF, PRI, and NDVIre following stress onset can be used to quantify qE, qZ, and chlorophyll content. This finding opens opportunities to use these parameters as a non-invasive tool for screening stress-tolerant genotypes under outdoor conditions. A particularly promising approach is the integration of SIF sensors with drone-based platforms for high-throughput field phenotyping (Bendig et al., 2023; Kneer et al., 2023). Such measurements would not only enable large-scale screening of

photoprotective traits but also provide valuable validation data for the ESA Earth Explorer mission.

5. References

Ač, A., Malenovský, Z., Olejníčková, J., Gallé, A., Rascher, U., Mohammed, G., 2015. Meta-analysis assessing potential of steady-state chlorophyll fluorescence for remote sensing detection of plant water, temperature and nitrogen stress. Remote Sensing of Environment 168, 420–436. https://doi.org/10.1016/j.rse.2015.07.022

Acebron, K., Matsubara, S., Jedmowski, C., Emin, D., Muller, O., Rascher, U., 2021. Diurnal dynamics of nonphotochemical quenching in Arabidopsis *npq* mutants assessed by solar-induced fluorescence and reflectance measurements in the field. New Phytol 229, 2104–2119. https://doi.org/10.1111/nph.16984

Acebron, K., Salvatori, N., Alberti, G., Muller, O., Peressotti, A., Rascher, U., Matsubara, S., 2022. Elucidating the photosynthetic responses in chlorophyll-deficient soybean (Glycine max, L.) Cultivar. Journal of Photochemistry and Photobiology 100152. https://doi.org/10.1016/j.jpap.2022.100152

Albert, L., Cushman, K.C., Allen, D.W., Zong, Y., Alonso, L., Kellner, J.R., 2019. Stray light characterization in a high-resolution imaging spectrometer designed for solar-induced fluorescence, in: Messinger, D.W., Velez-Reyes, M. (Eds.), Algorithms, Technologies, and Applications for Multispectral and Hyperspectral Imagery XXV. Presented at the Algorithms, Technologies, and Applications for Multispectral and Hyperspectral Imagery XXV, SPIE, Baltimore, United States, p. 15. https://doi.org/10.1117/12.2519395

Albert, L.P., Cushman, K.C., Zong, Y., Allen, D.W., Alonso, L., Kellner, J.R., 2023. Sensitivity of solar-induced fluorescence to spectral stray light in high resolution imaging spectroscopy. Remote Sensing of Environment 285, 113313. https://doi.org/10.1016/j.rse.2022.113313

Alonso, L., Gomez-Chova, L., Vila-Frances, J., Amoros-Lopez, J., Guanter, L., Calpe, J., Moreno, J., 2008. Improved Fraunhofer Line Discrimination Method for Vegetation Fluorescence Quantification. IEEE Geosci. Remote Sensing Lett. 5, 620–624. https://doi.org/10.1109/LGRS.2008.2001180

Arroyo-Mora, J.P., Kalacska, M., Løke, T., Schläpfer, D., Coops, N.C., Lucanus, O., Leblanc, G., 2021. Assessing the impact of illumination on UAV pushbroom hyperspectral imagery collected under various cloud cover conditions. Remote Sensing of Environment 258, 112396. https://doi.org/10.1016/j.rse.2021.112396

Arthur, A.M., Robinson, I., Rossini, M., Davis, N., MacDonald, K., 2014. A dual-field-of-view spectrometer system for reflectance and fluorescence measurements (Piccolo Doppio) and correction of etaloning. Proceedings of the Fifth International Workshop on Remote Sensing of Vegetation Fluorescence 9. http://www.congrexprojects.com/2014-events/14c04/proceedings

Asrar, G., Fuchs, M., Kanemasu, E.T., Hatfield, J.L., 1984. Estimating Absorbed Photosynthetic Radiation and Leaf Area Index from Spectral Reflectance in Wheat. Agronomy Journal 76, 300–306. https://doi.org/10.2134/agronj1984.00021962007600020029x

Baker, N.R., Rosenqvist, E., 2004. Applications of chlorophyll fluorescence can improve crop production strategies: an examination of future possibilities. J Exp Bot 55, 1607–1621. https://doi.org/10.1093/jxb/erh196

Ballaré, C.L., Pierik, R., 2017. The shade-avoidance syndrome: multiple signals and ecological consequences. Plant, Cell & Environment 40, 2530–2543. https://doi.org/10.1111/pce.12914

Bendig, J., Malenovsky, Z., Gautam, D., Lucieer, A., 2020. Solar-Induced Chlorophyll Fluorescence Measured From an Unmanned Aircraft System: Sensor Etaloning and Platform Motion Correction. IEEE Trans. Geosci. Remote Sensing 58, 3437–3444. https://doi.org/10.1109/TGRS.2019.2956194

Bendig, J., Siegmann, B., Kneer, C., Chakhvashvili, E., Kraemer, J., Choza-Farias, S., Rascher, U., 2023. Imaging Spatial Heterogeneity of Solar-Induced Chlorophyll Fluorescence (SIF) with Very High Spatial Resolution Drone Imagery, in: IGARSS 2023 - 2023 IEEE International Geoscience and Remote Sensing Symposium. Presented at the IGARSS 2023 - 2023 IEEE International Geoscience and Remote Sensing Symposium, pp. 4654–4657. https://doi.org/10.1109/IGARSS52108.2023.10283066

Bielczynski, L.W., Łącki, M.K., Hoefnagels, I., Gambin, A., Croce, R., 2017. Leaf and Plant Age Affects Photosynthetic Performance and Photoprotective Capacity. Plant Physiol 175, 1634–1648. https://doi.org/10.1104/pp.17.00904

Cendrero-Mateo, M.P., Bennertz, S., Burkart, A., Julitta, T., Cogliati, S., Scharr, H., Rademske, P., Alonso, L., Pinto, F., Rascher, U., 2018. Sun Induced Fluorescence Calibration and Validation for Field Phenotyping, in: IGARSS 2018 - 2018 IEEE International Geoscience and Remote Sensing Symposium. Presented at the IGARSS 2018 - 2018 IEEE International Geoscience and Remote Sensing Symposium, pp. 8248–8251. https://doi.org/10.1109/IGARSS.2018.8519174

Cendrero-Mateo, Wieneke, Damm, Alonso, Pinto, Moreno, Guanter, Celesti, Rossini, Sabater, Cogliati, Julitta, Rascher, Goulas, Aasen, Pacheco-Labrador, Arthur, 2019. Sun-Induced Chlorophyll Fluorescence III: Benchmarking Retrieval Methods and Sensor Characteristics for Proximal Sensing. Remote Sensing 11, 962. https://doi.org/10.3390/rs11080962

Chang, C.Y., Zhou, R., Kira, O., Marri, S., Skovira, J., Gu, L., Sun, Y., 2020. An Unmanned Aerial System (UAS) for concurrent measurements of solar-induced chlorophyll fluorescence and hyperspectral reflectance toward improving crop monitoring. Agricultural and Forest Meteorology 294, 108145. https://doi.org/10.1016/j.agrformet.2020.108145

Croce, R., Carmo-Silva, E., Cho, Y.B., Ermakova, M., Harbinson, J., Lawson, T., McCormick, A.J., Niyogi, K.K., Ort, D.R., Patel-Tupper, D., Pesaresi, P., Raines, C., Weber, A.P.M., Zhu, X.-G., 2024. Perspectives on improving photosynthesis to increase crop yield. Plant Cell 36, 3944–3973. https://doi.org/10.1093/plcell/koae132

Croce, R., van Amerongen, H., 2020. Light harvesting in oxygenic photosynthesis: Structural biology meets spectroscopy. Science 369, eaay2058. https://doi.org/10.1126/science.aay2058

Dall'Osto, L., Cazzaniga, S., Wada, M., Bassi, R., 2014. On the origin of a slowly reversible fluorescence decay component in the Arabidopsis npq4 mutant. Philosophical transactions of the Royal Society of London. Series B, Biological sciences 369, 20130221. https://doi.org/10.1098/rstb.2013.0221

D'Amico-Damião, V., Carvalho, R.F., 2018. Cryptochrome-Related Abiotic Stress Responses in Plants. Front. Plant Sci. 9. https://doi.org/10.3389/fpls.2018.01897

Damm, A., Erler, A., Hillen, W., Meroni, M., Schaepman, M.E., Verhoef, W., Rascher, U., 2011. Modeling the impact of spectral sensor configurations on the FLD retrieval accuracy of sun-induced chlorophyll fluorescence. Remote Sensing of Environment 115, 1882–1892. https://doi.org/10.1016/j.rse.2011.03.011

Damm, A., Guanter, L., Verhoef, W., Schläpfer, D., Garbari, S., Schaepman, M.E., 2015. Impact of varying irradiance on vegetation indices and chlorophyll fluorescence

derived from spectroscopy data. Remote Sensing of Environment 156, 202–215. https://doi.org/10.1016/j.rse.2014.09.031

Ehlert, B., Hincha, D.K., 2008. Chlorophyll fluorescence imaging accurately quantifies freezing damage and cold acclimation responses in Arabidopsis leaves. Plant Methods 4, 12. https://doi.org/10.1186/1746-4811-4-12

Ensminger, I., Sveshnikov, D., Campbell, D.A., Funk, C., Jansson, S., Lloyd, J., Shibistova, O., Öquist, G., 2004. Intermittent low temperatures constrain spring recovery of photosynthesis in boreal Scots pine forests. Global Change Biology 10, 995–1008. https://doi.org/10.1111/j.1365-2486.2004.00781.x

Féret, J.-B., Berger, K., de Boissieu, F., Malenovský, Z., 2021. PROSPECT-PRO for estimating content of nitrogen-containing leaf proteins and other carbon-based constituents. Remote Sensing of Environment 252, 112173. https://doi.org/10.1016/j.rse.2020.112173

Fletcher, K., 2015. Report for mission selection, ESA SP. ESA communications production, Noordwijk.

Fu, P., Meacham-Hensold, K., Siebers, M.H., Bernacchi, C.J., 2021. The inverse relationship between solar-induced fluorescence yield and photosynthetic capacity: benefits for field phenotyping. Journal of Experimental Botany 72, 1295–1306. https://doi.org/10.1093/jxb/eraa537

Gamon, J.A., Huemmrich, K.F., Wong, C.Y.S., Ensminger, I., Garrity, S., Hollinger, D.Y., Noormets, A., Peñuelas, J., 2016. A remotely sensed pigment index reveals photosynthetic phenology in evergreen conifers. Proceedings of the National Academy of Sciences 113, 13087–13092. https://doi.org/10.1073/pnas.1606162113

Gamon, J.A., Peñuelas, J., Field, C.B., 1992. A narrow-waveband spectral index that tracks diurnal changes in photosynthetic efficiency. Remote Sensing of Environment 41, 35–44. https://doi.org/10.1016/0034-4257(92)90059-S

Gehan, M.A., Fahlgren, N., Abbasi, A., Berry, J.C., Callen, S.T., Chavez, L., Doust, A.N., Feldman, M.J., Gilbert, K.B., Hodge, J.G., Hoyer, J.S., Lin, A., Liu, S., Lizárraga, C., Lorence, A., Miller, M., Platon, E., Tessman, M., Sax, T., 2017. PlantCV v2: Image analysis software for high-throughput plant phenotyping. PeerJ 5, e4088. https://doi.org/10.7717/peerj.4088

Gitelson, A., Merzlyak, M.N., 1994. Quantitative estimation of chlorophyll-*a* using reflectance spectra: Experiments with autumn chestnut and maple leaves. Journal of Photochemistry and Photobiology B: Biology 22, 247–252. https://doi.org/10.1016/1011-1344(93)06963-4

Gitelson, A.A., Gritz, Y., Merzlyak, M.N., 2003. Relationships between leaf chlorophyll content and spectral reflectance and algorithms for non-destructive chlorophyll assessment in higher plant leaves. Journal of Plant Physiology 160, 271–282. https://doi.org/10.1078/0176-1617-00887

Gitelson, A.A., Keydan, G.P., Merzlyak, M.N., 2006. Three-band model for noninvasive estimation of chlorophyll, carotenoids, and anthocyanin contents in higher plant leaves. Geophysical Research Letters 33. https://doi.org/10.1029/2006GL026457

Gray, G.R., Hope, B.J., Qin, X., Taylor, B.G., Whitehead, C.L., 2003. The characterization of photoinhibition and recovery during cold acclimation in Arabidopsis thaliana using chlorophyll fluorescence imaging. Physiologia Plantarum 119, 365–375. https://doi.org/10.1034/j.1399-3054.2003.00224.x

Grossmann, K., Frankenberg, C., Magney, T.S., Hurlock, S.C., Seibt, U., Stutz, J., 2018. PhotoSpec: A new instrument to measure spatially distributed red and far-red Solar-Induced Chlorophyll Fluorescence. Remote Sensing of Environment 216, 311–327. https://doi.org/10.1016/j.rse.2018.07.002

Guanter, L., Bacour, C., Schneider, A., Aben, I., van Kempen, T.A., Maignan, F., Retscher, C., Köhler, P., Frankenberg, C., Joiner, J., Zhang, Y., 2021. The TROPOSIF global sun-induced fluorescence dataset from the Sentinel-5P TROPOMI mission. Earth System Science Data 13, 5423–5440. https://doi.org/10.5194/essd-13-5423-2021

Guanter, L., Frankenberg, C., Dudhia, A., Lewis, P.E., Gómez-Dans, J., Kuze, A., Suto, H., Grainger, R.G., 2012. Retrieval and global assessment of terrestrial chlorophyll fluorescence from GOSAT space measurements. Remote Sensing of Environment 121, 236–251. https://doi.org/10.1016/j.rse.2012.02.006

Havaux, M., Bonfils, J.-P., Lütz, C., Niyogi, K.K., 2000. Photodamage of the Photosynthetic Apparatus and Its Dependence on the Leaf Developmental Stage in the npq1 Arabidopsis Mutant Deficient in the Xanthophyll Cycle Enzyme Violaxanthin De-epoxidase. Plant Physiol 124, 273–284. https://doi.org/10.1104/pp.124.1.273

Havaux, M., Kloppstech, K., 2001. The protective functions of carotenoid and flavonoid pigments against excess visible radiation at chilling temperature investigated in Arabidopsis npq and tt mutants. Planta 213, 953–966. https://doi.org/10.1007/s004250100572

Jacquemoud, S., Ustin, S., 2019. Leaf optical properties. Cambridge University Press, Cambridge. https://doi.org/10.1017/9781108686457

Jiang, Y., Snider, J.L., Li, C., Rains, G.C., Paterson, A.H., 2020. Ground Based Hyperspectral Imaging to Characterize Canopy-Level Photosynthetic Activities. Remote Sensing 12. https://doi.org/10.3390/rs12020315

Julitta, T., Corp, L., Rossini, M., Burkart, A., Cogliati, S., Davies, N., Hom, M., Mac Arthur, A., Middleton, E., Rascher, U., Schickling, A., Colombo, R., 2016. Comparison of Sun-Induced Chlorophyll Fluorescence Estimates Obtained from Four Portable Field Spectroradiometers. Remote Sensing 8, 122. https://doi.org/10.3390/rs8020122

Kagawa, T., Sakai, T., Suetsugu, N., Oikawa, K., Ishiguro, S., Kato, T., Tabata, S., Okada, K., Wada, M., 2001. Arabidopsis NPL1: a phototropin homolog controlling the chloroplast high-light avoidance response. Science 291, 2138–2141. https://doi.org/10.1126/science.291.5511.2138

Kallel, A., 2020. FluLCVRT: Reflectance and fluorescence of leaf and canopy modeling based on Monte Carlo vector radiative transfer simulation. Journal of Quantitative Spectroscopy and Radiative Transfer 253, 107183. https://doi.org/10.1016/j.jqsrt.2020.107183

Keller, B., Vass, I., Matsubara, S., Paul, K., Jedmowski, C., Pieruschka, R., Nedbal, L., Rascher, U., Muller, O., 2019. Maximum fluorescence and electron transport kinetics determined by light-induced fluorescence transients (LIFT) for photosynthesis phenotyping. Photosynth Res 140, 221–233. https://doi.org/10.1007/s11120-018-0594-9

Khanal, N., Bray, G.E., Grisnich, A., Moffatt, B.A., Gray, G.R., 2017. Differential Mechanisms of Photosynthetic Acclimation to Light and Low Temperature in Arabidopsis and the Extremophile Eutrema salsugineum. Plants 6, 32. https://doi.org/10.3390/plants6030032

Kleine, T., Kindgren, P., Benedict, C., Hendrickson, L., Strand, Å., 2007. Genome-Wide Gene Expression Analysis Reveals a Critical Role for CRYPTOCHROME1 in the Response of Arabidopsis to High Irradiance. Plant Physiol 144, 1391–1406. https://doi.org/10.1104/pp.107.098293

Kneer, C., Burkart, A., Bongartz, J., Siegmann, B., Bendig, J., Jenal, A., Rascher, U., 2023. A Snapshot Imaging System for the Measurement of Solar-Induced Chlorophyll Fluorescence— Addressing the Challenges of High-Performance Spectral Imaging. IEEE Sensors J. 23, 23255–23269. https://doi.org/10.1109/JSEN.2023.3297054

Kobayashi, M., Akutsu, S., Fujinuma, D., Furukawa, H., Komatsu, H., Hotota, Y., Kato, Y., Kuroiwa, Y., Watanabe, T., Ohnishi-Kameyama, M., Ono, H., Ohkubo, S., Miyashita, H., Kobayashi, M., Akutsu, S., Fujinuma, D., Furukawa, H., Komatsu, H., Hotota, Y., Kato, Y., Kuroiwa, Y., Watanabe, T., Ohnishi-Kameyama, M., Ono, H., Ohkubo, S., Miyashita, H., 2013. Physicochemical Properties of Chlorophylls in Oxygenic Photosynthesis — Succession of Co-Factors from Anoxygenic to Oxygenic Photosynthesis, in: Photosynthesis. IntechOpen. https://doi.org/10.5772/55460

Köhler, P., Guanter, L., Frankenberg, C., 2015. Simplified physically based retrieval of sun-induced chlorophyll fluorescence from GOSAT data. IEEE Geoscience and Remote Sensing Letters 12, 1446–1450. https://doi.org/10.1109/LGRS.2015.2407051

Kolber, Z., Klimov, D., Ananyev, G., Rascher, U., Berry, J., Osmond, B., 2005. Measuring photosynthetic parameters at a distance: laser induced fluorescence transient (LIFT) method for remote measurements of photosynthesis in terrestrial vegetation. Photosynth Res 84, 121–129. https://doi.org/10.1007/s11120-005-5092-1

Kolber, Z.S., Prášil, O., Falkowski, P.G., 1998. Measurements of variable chlorophyll fluorescence using fast repetition rate techniques: defining methodology and experimental protocols, Biochimica et Biophysica Acta (BBA) - Bioenergetics. https://doi.org/10.1016/S0005-2728(98)00135-2

Lakowicz, J.R., Masters, B.R., 2008. Principles of Fluorescence Spectroscopy, Third Edition. J. Biomed. Opt. 13, 029901. https://doi.org/10.1117/1.2904580

Leung, M.C.H., Chen, S., Jurgenson, C., 2022. Accurately Measuring Hyperspectral Imaging Distortion in Grating Spectrographs Using a Clustering Algorithm, in: Advances in Optical and Mechanical Technologies for Telescopes and Instrumentation V. p. 142. https://doi.org/10.1117/12.2630442

Luklová, M., Dubois, M., Kameniarová, M., Plačková, K., Novák, J., Kopecká, R., Karady, M., Pavlů, J., Skalák, J., Jindal, S., Tubić, L., Quddoos, Z., Novák, O., Inzé, D., Černý, M., 2025. Light Quantity Impacts Early Response to Cold and Cold Acclimation in Young Leaves of Arabidopsis. Plant, Cell & Environment 48, 5030–5052. https://doi.org/10.1111/pce.15481

Malnoë, A., 2018. Photoinhibition or photoprotection of photosynthesis? Update on the (newly termed) sustained quenching component qH. Environmental and Experimental Botany, An Integrative Approach to Photoinhibition and Photoprotection of Photosynthesis 154, 123–133. https://doi.org/10.1016/j.envexpbot.2018.05.005

Maxwell, K., Johnson, G.N., 2000. Chlorophyll fluorescence—a practical guide. Journal of Experimental Botany 51, 659–668. https://doi.org/10.1093/jexbot/51.345.659

Medina, Damm, Goulas, Wieneke, Hueni, Malenovský, Alonso, Pacheco-Labrador, Cendrero-Mateo, Tomelleri, Burkart, Cogliati, Rascher, Arthur, 2019. Sun-Induced Chlorophyll Fluorescence II: Review of Passive Measurement Setups, Protocols,

and Their Application at the Leaf to Canopy Level. Remote Sensing 11, 927. https://doi.org/10.3390/rs11080927

Meroni, M., Busetto, L., Colombo, R., Guanter, L., Moreno, J., Verhoef, W., 2010. Performance of Spectral Fitting Methods for vegetation fluorescence quantification. Remote Sensing of Environment 114, 363–374. https://doi.org/10.1016/j.rse.2009.09.010

Meroni, M., Rossini, M., Guanter, L., Alonso, L., Rascher, U., Colombo, R., Moreno, J., 2009. Remote sensing of solar-induced chlorophyll fluorescence: Review of methods and applications. Remote Sensing of Environment 113, 2037–2051. https://doi.org/10.1016/j.rse.2009.05.003

Mockler, T.C., Guo, H., Yang, H., Duong, H., Lin, C., 1999. Antagonistic actions of Arabidopsis cryptochromes and phytochrome B in the regulation of floral induction. Development 126, 2073–2082. https://doi.org/10.1242/dev.126.10.2073

Mohammed, G.H., Colombo, R., Middleton, E.M., Rascher, U., van der Tol, C., Nedbal, L., Goulas, Y., Pérez-Priego, O., Damm, A., Meroni, M., Joiner, J., Cogliati, S., Verhoef, W., Malenovský, Z., Gastellu-Etchegorry, J.-P., Miller, J.R., Guanter, L., Moreno, J., Moya, I., Berry, J.A., Frankenberg, C., Zarco-Tejada, P.J., 2019. Remote sensing of solar-induced chlorophyll fluorescence (SIF) in vegetation: 50 years of progress. Remote Sensing of Environment 231, 111177. https://doi.org/10.1016/j.rse.2019.04.030

Moncholi-Estornell, A., Van Wittenberghe, S., Pilar Cendrero-Mateo, M., Alonso, L., Jiménez, M., Urrego, P., Mac Arthur, A., Moreno, J., 2023. FluoCat: A cable-suspended multi-sensor system for the vegetation SIF Cal/Val monitoring and estimation of effective sunlit surface fluorescence. International Journal of Applied Earth Observation and Geoinformation 116, 103147. https://doi.org/10.1016/j.jag.2022.103147

Moore, R., 1998. Botany. WCB/McGraw-Hill, New York.

Murchie, E.H., Lawson, T., 2013. Chlorophyll fluorescence analysis: a guide to good practice and understanding some new applications. Journal of Experimental Botany 64, 3983–3998. https://doi.org/10.1093/jxb/ert208

Nehir, M., Frank, C., Aßmann, S., Achterberg, E.P., 2019. Improving Optical Measurements: Non-Linearity Compensation of Compact Charge-Coupled Device (CCD) Spectrometers. Sensors 19, 2833. https://doi.org/10.3390/s19122833

Nilkens, M., Kress, E., Lambrev, P., Miloslavina, Y., Müller, M., Holzwarth, A.R., Jahns, P., 2010. Identification of a slowly inducible zeaxanthin-dependent component of non-photochemical quenching of chlorophyll fluorescence generated under steady-state conditions in *Arabidopsis*. Biochimica et Biophysica Acta (BBA) - Bioenergetics 1797, 466–475. https://doi.org/10.1016/j.bbabio.2010.01.001

Pacheco-Labrador, J., Hueni, A., Mihai, L., Sakowska, K., Julitta, T., Kuusk, J., Sporea, D., Alonso, L., Burkart, A., Cendrero-Mateo, M.P., Aasen, H., Goulas, Y., Mac Arthur, A., 2019. Sun-Induced Chlorophyll Fluorescence I: Instrumental Considerations for Proximal Spectroradiometers. Remote Sensing 11, 960. https://doi.org/10.3390/rs11080960

Peng, H., Cendrero-Mateo, M.P., Bendig, J., Siegmann, B., Acebron, K., Kneer, C., Kataja, K., Muller, O., Rascher, U., 2022. HyScreen: A Ground-Based Imaging System for High-Resolution Red and Far-Red Solar-Induced Chlorophyll Fluorescence. Sensors 22, 9443. https://doi.org/10.3390/s22239443

Peñuelas, J., Gamon, J.A., Fredeen, A.L., Merino, J., Field, C.B., 1994. Reflectance indices associated with physiological changes in nitrogen- and water-limited sunflower leaves. Remote Sensing of Environment 48, 135–146. https://doi.org/10.1016/0034-4257(94)90136-8

Peterson, R., Havir, E., 2001. Photosynthetic properties of an Arabidopsis thaliana mutant possessing a defective PsbS gene. Planta 214, 142–152. https://doi.org/10.1007/s004250100601

Pinto, F., Damm, A., Schickling, A., Panigada, C., Cogliati, S., Müller-Linow, M., Balvora, A., Rascher, U., 2016. Sun-induced chlorophyll fluorescence from high-resolution imaging spectroscopy data to quantify spatio-temporal patterns of photosynthetic function in crop canopies: Sun-induced fluorescence in crop canopies. Plant, Cell & Environment 39, 1500–1512. https://doi.org/10.1111/pce.12710

Pinto, F., Müller-Linow, M., Schickling, A., Cendrero-Mateo, M., Ballvora, A., Rascher, U., 2017. Multiangular Observation of Canopy Sun-Induced Chlorophyll Fluorescence by Combining Imaging Spectroscopy and Stereoscopy. Remote Sensing 9, 415. https://doi.org/10.3390/rs9050415

Porcar-Castell, A., 2011. A high-resolution portrait of the annual dynamics of photochemical and non-photochemical quenching in needles of Pinus sylvestris. Physiologia Plantarum 143, 139–153. https://doi.org/10.1111/j.1399-3054.2011.01488.x

Porcar-Castell, A., Malenovský, Z., Magney, T., Van Wittenberghe, S., Fernández-Marín, B., Maignan, F., Zhang, Y., Maseyk, K., Atherton, J., Albert, L.P., Robson, T.M., Zhao, F., Garcia-Plazaola, J.-I., Ensminger, I., Rajewicz, P.A., Grebe, S., Tikkanen, M., Kellner, J.R., Ihalainen, J.A., Rascher, U., Logan, B., 2021. Chlorophyll a fluorescence illuminates a path connecting plant molecular biology to Earth-system science. Nat. Plants 7, 998–1009. https://doi.org/10.1038/s41477-021-00980-4

Porcar-Castell, A., Tyystjärvi, E., Atherton, J., van der Tol, C., Flexas, J., Pfündel, E.E., Moreno, J., Frankenberg, C., Berry, J.A., 2014. Linking chlorophyll a fluorescence to photosynthesis for remote sensing applications: mechanisms and challenges. Journal of Experimental Botany 65, 4065–4095. https://doi.org/10.1093/jxb/eru191

Puggioni, M.P., 2020. Dynamic regulation of oxygenic photosynthesis: study of long term acclimation to photo-oxidative stress induced by excess of light (Doctoral dissertation). Heinrich Heine University Düsseldorf, Düsseldorf.

R Core Team, 2024. R: A Language and Environment for Statistical Computing.

Rankenberg, T., Geldhof, B., van Veen, H., Holsteens, K., Van de Poel, B., Sasidharan, R., 2021. Age-Dependent Abiotic Stress Resilience in Plants. Trends in Plant Science 26, 692–705. https://doi.org/10.1016/j.tplants.2020.12.016

Rascher, U., Agati, G., Alonso, L., Cecchi, G., Champagne, S., Colombo, R., Damm, A., Daumard, F., De Miguel, E., Fernandez, G., Franch, B., Franke, J., Gerbig, C., Gioli, B., Gómez, J.A., Goulas, Y., Guanter, L., Gutiérrez-de-la-Cámara, Ó., Hamdi, K., Hostert, P., Jiménez, M., Kosvancova, M., Lognoli, D., Meroni, M., Miglietta, F., Moersch, A., Moreno, J., Moya, I., Neininger, B., Okujeni, A., Ounis, A., Palombi, L., Raimondi, V., Schickling, A., Sobrino, J.A., Stellmes, M., Toci, G., Toscano, P., Udelhoven, T., Van Der Linden, S., Zaldei, A., 2009. CEFLES2: the remote sensing component to quantify photosynthetic efficiency from the leaf to the region by measuring sun-induced fluorescence in the oxygen absorption bands. Biogeosciences 6, 1181–1198. https://doi.org/10.5194/bg-6-1181-2009

Rascher, U., Alonso, L., Burkart, A., Cilia, C., Cogliati, S., Colombo, R., Damm, A., Drusch, M., Guanter, L., Hanus, J., Hyvärinen, T., Julitta, T., Jussila, J., Kataja, K., Kokkalis, P., Kraft, S., Kraska, T., Matveeva, M., Moreno, J., Muller, O., Panigada, C., Pikl, M., Pinto, F., Prey, L., Pude, R., Rossini, M., Schickling, A., Schurr, U., Schüttemeyer, D., Verrelst, J., Zemek, F., 2015. Sun-induced fluorescence - a new probe of photosynthesis: First maps from the imaging spectrometer *HyPlant*. Glob Change Biol 21, 4673–4684. https://doi.org/10.1111/gcb.13017

Rossini, M., Meroni, M., Celesti, M., Cogliati, S., Julitta, T., Panigada, C., Rascher, U., van der Tol, C., Colombo, R., 2016. Analysis of Red and Far-Red Sun-Induced Chlorophyll Fluorescence and Their Ratio in Different Canopies Based on Observed and Modeled Data. Remote Sensing 8, 412. https://doi.org/10.3390/rs8050412

Rossini, M., Nedbal, L., Guanter, L., Ač, A., Alonso, L., Burkart, A., Cogliati, S., Colombo, R., Damm, A., Drusch, M., Hanus, J., Janoutova, R., Julitta, T., Kokkalis, P., Moreno, J., Novotny, J., Panigada, C., Pinto, F., Schickling, A., Schüttemeyer, D., Zemek, F., Rascher, U., 2015. Red and far red Sun-induced chlorophyll fluorescence as a measure of plant photosynthesis. Geophysical Research Letters 42, 1632–1639. https://doi.org/10.1002/2014GL062943

Rouse, J.W., Haas, R.H., Schell, J.A., Deering, D.W., 1973. Monitoring vegetation systems in the great plains with ERTS, in: Proceedings of 3rd Earth Resources Technology Satellite Symposium. Presented at the Third ERTS-1 Symposium NASA, Greenbelt, pp. 309–317.

Ruban, A., Foyer, C.H., Murchie, E.H., 2022. Photosynthesis in action: harvesting light, generating electrons, fixing carbon. Academic press, Elsevier, London [etc.].

Ruban, A.V., 2016. Nonphotochemical Chlorophyll Fluorescence Quenching: Mechanism and Effectiveness in Protecting Plants from Photodamage. Plant Physiol 170, 1903–1916. https://doi.org/10.1104/pp.15.01935

Ruban, A.V., Saccon, F., 2022. Chlorophyll a de-excitation pathways in the LHCII antenna. The Journal of Chemical Physics 156, 070902. https://doi.org/10.1063/5.0073825

Ruehr, S., Gerlein-Safdi, C., Falco, N., Seibert, P.O., Chou, C., Albert, L., Keenan, T.F., 2024. Quantifying Seasonal and Diurnal Cycles of Solar-Induced Fluorescence With a Novel Hyperspectral Imager. Geophysical Research Letters 51, e2023GL107429. https://doi.org/10.1029/2023GL107429

Sabater, N., Vicent, J., Alonso, L., Verrelst, J., Middleton, E.M., Porcar-Castell, A., Moreno, J., 2018. Compensation of Oxygen Transmittance Effects for Proximal Sensing Retrieval of Canopy–Leaving Sun–Induced Chlorophyll Fluorescence. Remote Sensing 10, 1551. https://doi.org/10.3390/rs10101551

Schaepman, M.E., Dangel, S., 2000. Solid laboratory calibration of a nonimaging spectroradiometer. Appl. Opt. 39, 3754. https://doi.org/10.1364/AO.39.003754

Scharr, H., Rademske, P., Alonso, L., Cogliati, S., Rascher, U., 2021. Spatio-spectral deconvolution for high resolution spectral imaging with an application to the estimation of sun-induced fluorescence. Remote Sensing of Environment 267, 112718. https://doi.org/10.1016/j.rse.2021.112718

Schindelin, J., Arganda-Carreras, I., Frise, E., Kaynig, V., Longair, M., Pietzsch, T., Preibisch, S., Rueden, C., Saalfeld, S., Schmid, B., Tinevez, J.-Y., White, D.J., Hartenstein, V., Eliceiri, K., Tomancak, P., Cardona, A., 2012. Fiji: an open-source platform for biological-image analysis. Nat Methods 9, 676–682. https://doi.org/10.1038/nmeth.2019

Schmalstig, J.G., Jainandan, K., 2021. Green light attenuates blue-light-induced chloroplast avoidance movement in Arabidopsis and Landoltia punctata. American Journal of Botany 108, 1525–1539. https://doi.org/10.1002/ajb2.1717

Schramma, N., Perugachi Israëls, C., Jalaal, M., 2023. Chloroplasts in plant cells show active glassy behavior under low-light conditions. Proceedings of the National Academy of Sciences 120, e2216497120. https://doi.org/10.1073/pnas.2216497120

Schreiber, U., Schliwa, U., Bilger, W., 1986. Continuous recording of photochemical and non-photochemical chlorophyll fluorescence quenching with a new type of modulation fluorometer. Photosynth Res 10, 51–62. https://doi.org/10.1007/BF00024185

Siegmann, B., Alonso, L., Celesti, M., Cogliati, S., Colombo, R., Damm, A., Douglas, S., Guanter, L., Hanuš, J., Kataja, K., Kraska, T., Matveeva, M., Moreno, J., Muller, O., Pikl, M., Pinto, F., Quirós Vargas, J., Rademske, P., Rodriguez-Morene, F., Sabater, N., Schickling, A., Schüttemeyer, D., Zemek, F., Rascher, U., 2019. The High-Performance Airborne Imaging Spectrometer HyPlant—From Raw Images to Top-of-Canopy Reflectance and Fluorescence Products: Introduction of an Automatized Processing Chain. Remote Sensing 11, 2760. https://doi.org/10.3390/rs11232760

Siegmann, B., Cendrero-Mateo, M.P., Cogliati, S., Damm, A., Gamon, J., Herrera, D., Jedmowski, C., Junker-Frohn, L.V., Kraska, T., Muller, O., Rademske, P., van der Tol, C., Quiros-Vargas, J., Yang, P., Rascher, U., 2021. Downscaling of far-red solar-induced chlorophyll fluorescence of different crops from canopy to leaf level using a diurnal data set acquired by the airborne imaging spectrometer HyPlant. Remote Sensing of Environment 264, 112609. https://doi.org/10.1016/j.rse.2021.112609

Smith, G.M., Milton, E.J., 1999. The use of the empirical line method to calibrate remotely sensed data to reflectance. International Journal of Remote Sensing 20, 2653–2662. https://doi.org/10.1080/014311699211994

Taiz, L., Zeiger, E., Møller, I.M., Murphy, A.S., 2015. Plant physiology and development, Sixth edition. ed. Sinauer Associates, Inc., Publishers, Sunderland, Massachusetts.

Takahashi, D., Soga, K., Kikuchi, T., Kutsuno, T., Hao, P., Sasaki, K., Nishiyama, Y., Kidokoro, S., Sampathkumar, A., Bacic, A., Johnson, K.L., Kotake, T., 2024. Structural changes in cell wall pectic polymers contribute to freezing tolerance induced by cold acclimation in plants. Current Biology 34, 958-968.e5. https://doi.org/10.1016/j.cub.2024.01.045

Taniguchi, M., Lindsey, J.S., 2021. Absorption and Fluorescence Spectral Database of Chlorophylls and Analogues. Photochemistry and Photobiology 97, 136–165. https://doi.org/10.1111/php.13319

Tsujimoto, K., Hikosaka, K., 2021. Estimating leaf photosynthesis of C3 plants grown under different environments from pigment index, photochemical reflectance index, and chlorophyll fluorescence. Photosynth Res 148, 33–46. https://doi.org/10.1007/s11120-021-00833-3

van Amerongen, H., Croce, R., 2025. Nonphotochemical quenching in plants: Mechanisms and mysteries. Plant Cell 37, koaf240. https://doi.org/10.1093/plcell/koaf240

Van Wittenberghe, S., Alonso, L., Verrelst, J., Moreno, J., Samson, R., 2015. Bidirectional sun-induced chlorophyll fluorescence emission is influenced by leaf structure and light scattering properties — A bottom-up approach. Remote Sensing of Environment 158, 169–179. https://doi.org/10.1016/j.rse.2014.11.012

Velitchkova, M., Popova, A.V., Faik, A., Gerganova, M., Ivanov, A.G., 2020. Low temperature and high light dependent dynamic photoprotective strategies in Arabidopsis thaliana. Physiologia Plantarum 170, 93–108. https://doi.org/10.1111/ppl.13111

Vella, N.G.F., Joss, T.V., Roberts, T.H., 2012. Chilling-induced ultrastructural changes to mesophyll cells of Arabidopsis grown under short days are almost completely reversible by plant re-warming. Protoplasma 249, 1137–1149. https://doi.org/10.1007/s00709-011-0363-5

Verhoeven, A., 2014. Sustained energy dissipation in winter evergreens. New Phytologist 201, 57–65. https://doi.org/10.1111/nph.12466

Wang, N., Suomalainen, J., Bartholomeus, H., Kooistra, L., Masiliunas, D., Clevers, J.G.P.W., 2021. Diurnal variation of sun-induced chlorophyll fluorescence of agricultural crops observed from a point-based spectrometer on a UAV. International Journal of Applied Earth Observation and Geoinformation 96. https://doi.org/10.1016/j.jag.2020.102276

Wang, T., Wu, S., Zheng, S., Feng, H., Wen, J., Lin, J., Yu, L., 2024. HSIS-SIF a high-performance hyperspectral imaging spectrometer for Solar-Induced Chlorophyll Fluorescence of vegetation. Optics and Lasers in Engineering 180, 108347. https://doi.org/10.1016/j.optlaseng.2024.108347

Wei, C., Huang, J., Wang, X., Blackburn, G.A., Zhang, Y., Wang, S., Mansaray, L.R., 2017. Hyperspectral characterization of freezing injury and its biochemical impacts in oilseed rape leaves. Remote Sensing of Environment 195, 56–66. https://doi.org/10.1016/j.rse.2017.03.042

Wientjes, E., van Amerongen, H., Croce, R., 2013. LHCII is an antenna of both photosystems after long-term acclimation. Biochimica et Biophysica Acta (BBA) - Bioenergetics 1827, 420–426. https://doi.org/10.1016/j.bbabio.2012.12.009

Yang, P., van der Tol, C., 2018. Linking canopy scattering of far-red sun-induced chlorophyll fluorescence with reflectance. Remote Sensing of Environment 209, 456–467. https://doi.org/10.1016/j.rse.2018.02.029

Yang, P., van der Tol, C., Campbell, P.K.E., Middleton, E.M., 2021. Unraveling the physical and physiological basis for the solar- induced chlorophyll fluorescence and photosynthesis relationship using continuous leaf and canopy measurements of a corn crop. Biogeosciences 18, 441–465. https://doi.org/10.5194/bg-18-441-2021

Yang, P., Van Der Tol, C., Campbell, P.K.E., Middleton, E.M., 2020. Fluorescence Correction Vegetation Index (FCVI): A physically based reflectance index to separate physiological and non-physiological information in far-red sun-induced chlorophyll fluorescence. Remote Sensing of Environment 240, 111676. https://doi.org/10.1016/j.rse.2020.111676

Yang, X., Shi, H., Stovall, A., Guan, K., Miao, G., Zhang, Yongguang, Zhang, Yao, Xiao, X., Ryu, Y., Lee, J.-E., 2018. FluoSpec 2—An Automated Field Spectroscopy System to Monitor Canopy Solar-Induced Fluorescence. Sensors 18, 2063. https://doi.org/10.3390/s18072063

Zeng, Y., Badgley, G., Dechant, B., Ryu, Y., Chen, M., Berry, J., 2019. A practical approach for estimating the escape ratio of near-infrared solar-induced chlorophyll fluorescence. REMOTE SENSING OF ENVIRONMENT 232. https://doi.org/10.1016/j.rse.2019.05.028

Zeng, Y., Chen, M., Hao, D., Damm, A., Badgley, G., Rascher, U., Johnson, J.E., Dechant, B., Siegmann, B., Ryu, Y., Qiu, H., Krieger, V., Panigada, C., Celesti, M., Miglietta, F., Yang,

X., Berry, J.A., 2022a. Combining near-infrared radiance of vegetation and fluorescence spectroscopy to detect effects of abiotic changes and stresses. Remote Sensing of Environment 270, 112856. https://doi.org/10.1016/j.rse.2021.112856

Zeng, Y., Chen, M., Hao, D., Damm, A., Badgley, G., Rascher, U., Johnson, J.E., Dechant, B., Siegmann, B., Ryu, Y., Qiu, H., Krieger, V., Panigada, C., Celesti, M., Miglietta, F., Yang, X., Berry, J.A., 2022b. Combining near-infrared radiance of vegetation and fluorescence spectroscopy to detect effects of abiotic changes and stresses. Remote Sensing of Environment 270, 112856. https://doi.org/10.1016/j.rse.2021.112856

Zong, Y., Brown, S.W., Johnson, B.C., Lykke, K.R., Ohno, Y., 2006. Simple spectral stray light correction method for array spectroradiometers. Appl. Opt. 45, 1111. https://doi.org/10.1364/AO.45.001111

6. Acknowledgements

First and foremost, I would like to express my deepest gratitude to my Doktorvater, Prof. Dr. Uwe Rascher. Thank you for giving me the opportunity to pursue my Ph.D. in your group. Your guidance, consistent feedback, and patience supported me throughout my studies. Your broad perspective, critical thinking, and enthusiasm for research have always inspired me.

I would also like to sincerely thank my day-to-day supervisors: Dr. Juliane Bendig, Dr. M. Pilar Cendrero-Mateo, and Dr. Kelvin Acebron. Juliane, I owe much of this thesis to you. When I lacked motivation or confidence, you never gave up on me and always encouraged me to move forward. Thank you for guiding me through the writings. You showed me what it means to be a scholar with strong beliefs and integrity. M^{a}Pi, you were the guide who led me into my research. You taught me how to work with HyScreen step by step, and the HyScreen data-processing chain you developed made it possible for me to continue my research. Your insightful comments guided my thesis, and your encouragement helped me believe that progress is made one step at a time. Kelvin, your advice opened the door for me to deeply explore energy partitioning in the light reactions of photosynthesis. You helped me identify complex and meaningful plant science questions and reaffirmed my love for plant biology. I will always remember your advice to be more mindful. Although it was difficult, it helped me let go of regret about the past and fear of the future, and to focus on the moment.

I am very grateful to the scientists and technicians who supported my research. Dr. Shizue Matsubara, I thank you for providing the Arabidopsis material and for guiding me in understanding and analyzing the different components of NPQ. You inspired my curiosity and motivation to explore complex yet fascinating biological questions. I wish I had been less shy and had discussed plant physiology with you more often. I would also like to thank Dr. Onno Muller, Dr. Bastian Siegmann, Patrick Rademske, Dr. Mark Müller-Linow, and Dr. Hanno Scharr for their valuable discussions and feedback on my research. I thank everyone who helped me with experiments: Michael, Nils, Angelina, Ilgaz, Beate, and Katharina. Special thanks go to Michael, who drove me to CKA, helped assemble the instruments, customized components in the workshop, and supported me in many practical ways. Without him, I could not have completed the experiments during the pandemic.

I also thank my peers in the Shoot Group: Juan, Vera, Oliver, Yuxi, Ana, Julie, David, Erekle, Jim, Saja, Sofia, Deepthi, Andrea, and Antony. I deeply miss our days at IBG-2, when we would gather downstairs, leave at 11:46 for lunch, and talk about research and life on the way to, and in, the Seecasino. Thank you to my Chinese friends at IBG—Fang, Xiaoran, Xinyu, Kunpeng, Yuxi, Shiyan, Congcong, Bo, Genghong, and Ruonan—for your help, companionship, and wonderful food. Thanks also to our friends in Germany, Boyuan, Anran, Xiang, and Yibin, for our conversations beyond daily life, and to my long-time friends Zhiyuan, Jiani, Yaoxin, Yanjun, Jie, and Ting. You all made my life richer and more joyful.

Finally, I thank my parents and my brother's family for their unconditional support of my education. I am deeply grateful to have such a family. Most of all, I thank my beloved husband, Runxuan. Thank you for being with me over the past six years and our discussions about broad topics. Thank you for teaching me atomic physics when I wanted to understand molecular energy levels. I love our motto: learning, thinking, and feeling.